Integrated Tunable LC Higher-Order Microwave Filters for Interference Mitigation

Farooq U. Amin

Dissertation submitted to the faculty of the Virginia Polytechnic Institute and State University in partial fulfillment of the requirements for the degree of

Doctor of Philosophy
In
Electrical Engineering

Kwang-Jin Koh, Chair
Sanjay Raman, Co-Chair
Ahmad Safaai-Jazi
Marius K. Orlowski
Vinh Nguyen

NOVEMBER 30th, 2017
Blacksburg, Virginia

Keywords: Tunable Filter, Active Filter, Q-enhanced Filter, 4th-order BPF, Wideband filter, RFIC

Integrated Tunable LC Higher-Order Microwave Filters for Interference Mitigation

Farooq U. Amin

ABSTRACT

Modern and future communication and radar systems require highly reconfigurable RF front-ends to realize the vision of Software-Defined Radio (SDR), where a single digitally-enabled radio is able to cover multiple bands and multiple operating standards. However, in the increasingly hostile RF environment, filtering becomes a bottleneck for SDRs as the traditional off-chip filters are fixed frequency and bulky. Therefore, tunable filtering is a critical building block for the reconfigurable RF front-ends and on-chip implementations are needed to meet size and weight constraints. On-chip passive components are lossy, especially inductors, and to fulfill the tunability requirements a number of active circuit techniques, e.g. N-path, Q-enhanced, discrete-time filters etc., have been developed. Most of these active filtering techniques, however, are limited to RF frequency range of few GHz and below. Additionally, these techniques lack or have very limited bandwidth tunability. On the other hand, Q-enhanced tunable LC filtering has the potential to be implemented at Microwave frequencies from 4~20 GHz and beyond.

In this dissertation, a number of Q-enhanced parallel synthesis techniques have been proposed and implemented to achieve high-order, frequency tunable, and wide bandwidth tunable filters. First, a tunable 4^{th}-order BPF was proposed and implemented in Silicon Germanium (SiGe) BiCMOS technology. Along with center frequency tuning, the filter achieves first ever reported 3-dB bandwidth tuning from 2% to 25%, representing 120 MHz to 1.5 GHz of bandwidth at 6 GHz. A new set of design equations were developed for the 4^{th}-order parallel synthesis of BPF. A practical switched varactor control scheme is proposed for large tuning ratio varactors to reduce the nonlinear contribution from the varactor substantially which improves the tunable LC BPF filter linearity. Second, parallel addition and subtraction techniques were proposed to realize

tunable dual-band filters. The subtraction technique is implemented in SiGe BiCMOS technology at X and Ku bands with more than 50 dB of out-of-band attenuation. Finally, a true wideband band-reject filter technique was proposed for microwave frequencies using parallel synthesis of two band-pass filters and an all-pass path. The proposed band-reject scheme is tunable and wide 20 dB attenuation bandwidths on the order of 10s of MHz to 100s of MHz can be achieved using this scheme.

The implementation of the proposed parallel synthesis techniques in silicon technology along with measured results demonstrate that Q-enhanced filtering is favorable at higher microwave frequencies. Therefore, such implementations are suitable for future wireless communication and radar systems particularly wide bandwidth systems on the order of 100s of MHz to GHz. Future research includes, high-order reconfigurable band-pass and band-reject filters, automatic tuning control, and exploring the parallel synthesis techniques in Gallium Nitride (GaN) technology for high RF power applications.

Integrated Tunable LC Higher-Order Microwave Filters for Interference Mitigation

Farooq U. Amin

GENERAL AUDIENCE ABSTRACT

The year is 2017 and the current state of the art smartphone can do amazing things using its wireless technologies including LTE, WiFi, Bluetooth, NFC, FM, GPS etc. Each of these wireless standards requires a hardware receiver and a transmitter, also called radio, so as to receive and transmit the signals over air using their designated frequencies. Often more than a single radio is needed to cover different frequency bands, e.g., LTE requires multiple radios to enable operation with different cellular providers and to be used in different countries in cases where the designated frequencies for LTE differs. In order to further reduce the size and cost of communication devices, including but not limited to smartphone, it is desired to implement a single software controlled hardware radio which can cover all of the aforementioned wireless standards. In doing so, the single radio has to distinguish between the desired signal and unwanted signals, also called interference, from other radios using filters that are needed to be reconfigurable to accommodate different wireless standards and bands. The same reconfigurable requirement is valid for radars as well. Therefore, there is a need for the research and development of cost effective and small size dynamic filters which can be controlled from software to adapt to different wireless standards.

In this dissertation, a number of filtering techniques are presented to make the radio tunable and agile in terms of operating frequency and bandwidth. The proposed techniques employs very large frequency and bandwidth tuning and are implemented in on-chip integrated circuit (IC) silicon technology. By doing so, the proposed on-chip integrated filters become tens to hundreds of times smaller than traditional off-chip filters which occupies majority of the space in small form factor devices. Therefore, the proposed tunable filters implementations are suitable for future wireless communication and radar systems particularly wide bandwidth systems to increase the data rate and radar detection accuracy.

Acknowledgments

I would like to express my deep gratitude to my research advisers Professor Kwang-Jin Koh and Professor Sanjay Raman for their tremendous guidance and support. Professor Koh, for his deep technical advice, comments, and dedication to RFIC research. Professor Raman has been a source of inspiration for me and I always found him very helpful and his comments very constructive. Without his invaluable guidance, moral and funding support, I could have never imagined finishing my doctoral work.

I am very grateful to my other committee members: Professor Ahmad Safaai-Jazi, Professor Marius Orlowski, and Professor Vinh Nguyen for serving on my doctoral committee. I would like to thank all my colleagues and professors at MICS for their support and collaboration. I am particularly grateful for the RFIC tools support provided by John Harris at ECE department. Much of this work would not have been possible by the kind support of BAE Systems and Northrop Grumman Mission Systems. I also gratefully acknowledge the graduate fellowship from the Virginia Space Grant Consortium. I would also have to thank all my friends at Blacksburg for making my stay memorable.

I would like to thank my parents, brothers and sisters, and my in-laws for their love and support. I have great appreciation for my father-in-law, Dr. Saifullah Afridi, who was at the forefront of encouraging me take on this challenge. Finally, I wish to thank and dedicate my achievements to my wife Razia and my two wonderful daughters, Zoya and Sofia, who have been the most important to me during this endeavor.

Table of Contents

List of Tables

List of Figures and Illustrations

List of Abbreviations and Nomenclature

Symbol	Definition
ADC	Analog to Digital Converter
AP	All-Pass
BAW	Bulk Acoustic Wave
BiCMOS	Bipolar Complementary Metal Oxide Semiconductor
BPF	Band Pass Filter
BRF	Band Reject Filter
BSF	Band Stop Filter
BW	Bandwidth
BPF	Band Pass Filter
C-band	Radar band name from 4-8 GHz
CDMA	Code Division Multiple Access
CMOS	Complementary Metal Oxide Semiconductor
DR	Dynamic Range
DT	Discrete Time
FDD	Frequency Division Duplexing
GaN	Gallium Nitride
GaAs	Gallium Arsenide
GD	Group Delay
Gm-C	Transconductance (Gm) and Capacitor (C)
GSSG	Ground-Signal-Signal-Ground
HD	Harmonic Distortion
IC	Integrated Circuit
IF	Intermediate Frequency
IMD	Intermodulation Distortion
IMD2	Second order Intermodulation Distortion
IMD3	Third order Intermodulation Distortion

IIP3	Third order Intercept Point
Ku-band	Radar band name from 12-18 GHz
LC-Tank	Inductor and Capacitor in parallel configuration
LNA	Low Noise Amplifier
LTE	Long Term Evolution
MOS	Metal Oxide Semiconductor
N-path	Filter type with N no. of switches driven by N clock phases.
OOB	Out of Band
OpAmp	Operational Amplifier
P_{-1dB}	1-dB Compression Point
PA	Power Amplifier
RF	Radio Frequency
RX	Receiver
SAW	Surface Acoustic Wave
SDR	Software Defined Radio
SiGe	Silicon Germanium
SIR	Substrate Integrated Waveguide
SNR	Signal-to-Noise Ratio
TDD	Time Division Duplexing
TX	Transmitter
VCO	Voltage Controlled Oscillator
X-band	Radar band name from 8-12 GHz

Chapter One: **Introduction**

1.1 Background

Modern and next generation wireless communication and radar systems require multi-band, multi-standard Radio Frequency (RF) operations, driving the need for multiple radios on the same platform. Figure 1-1 shows a generic modern wireless front-end where the antenna is shared between the transmitter (TX) and receiver (RX) using either a switch in time division duplexing (TDD) or a duplexer in frequency division duplexing (FDD). The receiver consists of a series of bandpass filters (BPFs) appropriately placed in the receiver chain to filter out unwanted signals and allow the desired signal. Due to the transmission loss, a low-noise amplifier is needed to amplify the signal with minimal noise added, while reducing the noise contribution of subsequent stages. The signal is down-converted using a mixer and then processed by the low frequency analog or digital circuits. The transmitter consists of data signal modulation and up-conversion to carrier frequency, followed by a set of two amplifiers, the driver and power amplifier (PA). The modulated high power signal is then filtered and transmitted by the antenna.

Figure 1-2 illustrates the problem of a modern cell phone containing multiple wireless standards each requiring a radio. Within each of these wireless standards, there is also a need to tune the radios at different bands thereby leading to increased number of selection components like filters and switches. Figure 1-3 shows the complexity of a modern 4G LTE RF front-end module

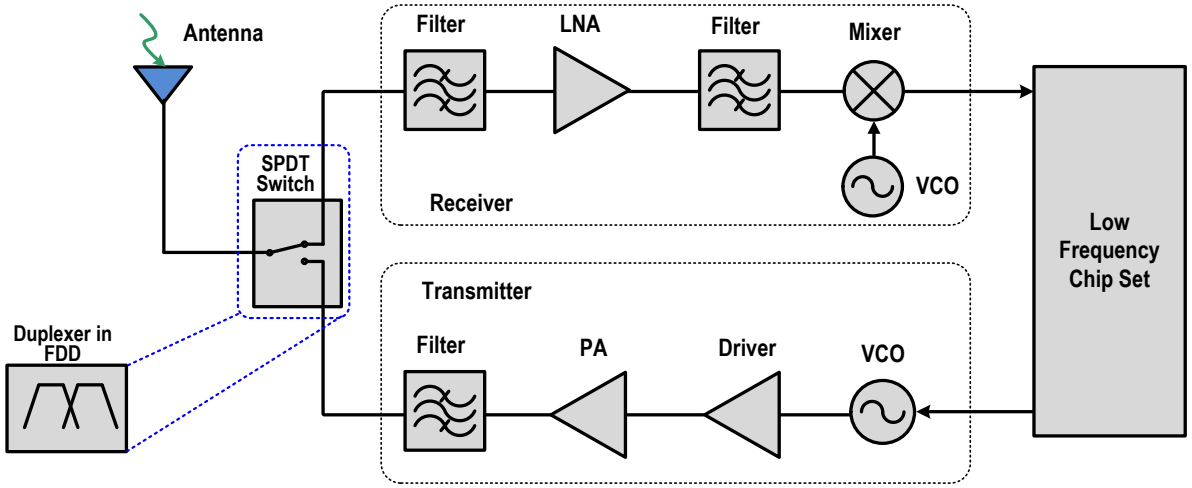

Figure 1-1: Generic RF Front-End with Transmitter and Receiver sharing a single antenna using Time-Division Duplexing.

covering the LTE low, mid and high bands. A number of filters are needed to select the RX and TX to these bands. This is accomplished by RF switches before and after the filters employing that these bandpass filters are fixed frequency. Traditionally, the front-end filters needed for band selection interference rejection are off-chip using technologies such as Bulk Acoustic Wave (BAW) and Surface Acoustic Wave (SAW). These filters are bulky and fixed frequency and a current research trend is to replace these with on-chip tunable filters.

1.2 Interference in Receivers

Any large power signal, other than the signal of interest, present at the input of receiver is considered an interferer (also called a blocker). Due to the non-linear behavior of the components in the receiver, high power interference can cause a number of non-linear distortions and can degrade reception of the signal of interest. The discussion of in-band interference verses out-of-band interference is subject to the particular operating frequencies, wireless standard, and communication system deployed. In general the frequency bandwidths and separations are smaller at lower RF frequencies like 1~2 GHz and increases when we move to higher microwave

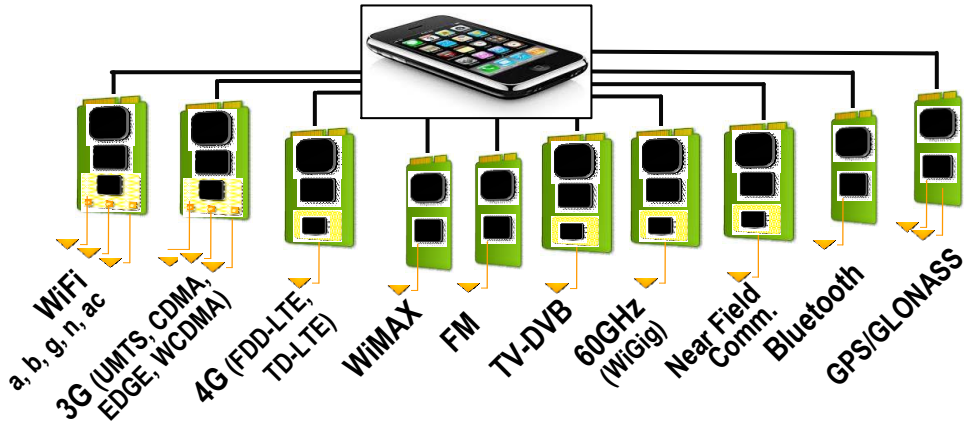

Figure 1-2: Conceptual illustration of multiple radios in a modern mobile phone.

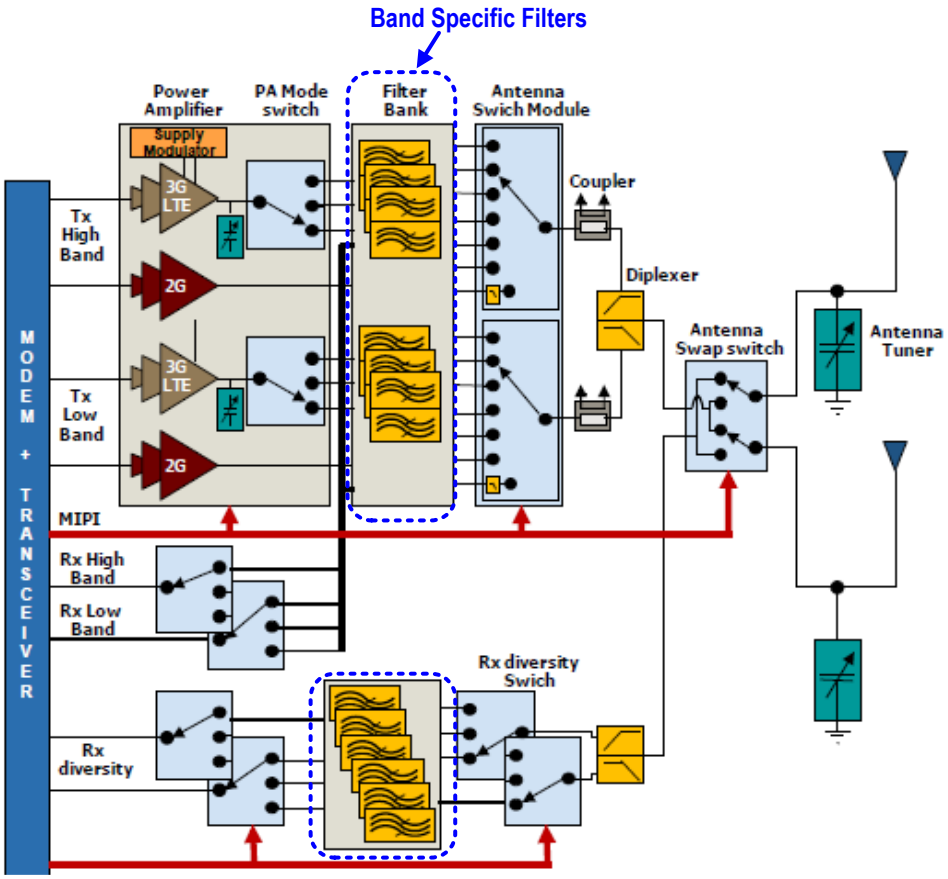

Figure 1-3: Example RF front-end complexity of a 4G LTE module (Source: Qorvo)

frequencies like 5~20 GHz. For example, the FDD-LTE bands (total of 31 spread over frequency range from 452 MHz to 3.6 GHz) bandwidth can be as small as 5MHz and as large as 90 MHz. TDD-LTE bands bandwidths ranges from 15 to 200 MHz. For the case of radar, there are many different types of radars with widely varying power and pulse bandwidth operating in the bands, S (2-4 GHz), C (4-8 GHz), X (8-12 GHz), and Ku (12-18 GHz) as shown in Table 1-1. For example, for Ku band synthetic aperture radar (SAR) or ground moving target radar (GMTI), the pulse bandwidth can vary from 10 MHz to more than 1 GHz compared to an X band marine radar of pulse bandwidth of 10 MHz. Filtering requirements are different for the consumer communication systems, where the front-end filter does the band selection to remove out-of-band interference whereas the channel selection to remove the in-band interference is either done in baseband analog or digital domain depending on the linearity requirements for the down conversion and digital conversion.

Table 1-1: Examples of Generic Radar Types and Implementations.

Radar Band	Generic Radar Role	RX Bandwidth
S	Air Traffic Management	1 MHz
X	Airborne Maritime Reconnaissance	10 MHz – 100 MHz
X	Fast Jet Radar	10 MHz
Ku	Small Airborne SAR/GMTI	10 MHz – >1 GHz
Radar Band	Specific Radar Implementation Examples	RX Bandwidth
S	Air Traffic Control ASR-11 Board[1]	100 MHz
C	FMCW Phased Array Receiver Board [2]	200 MHz
X	FMCW Radar Transceiver IC with Off-chip filter [3]	150 MHz

1.2.1 Interference and Self-interference

In a very crowded electromagnetic environment with many radios, a nearby transmitter power can appear at the input of the receiver as shown in Figure 1-4 (a). The transmit power is usually very large, to cover a large distance, compared to a received signal power. This transmit power can de-sensitize the receiver when it arrives together with the signal of interest at the input of receiver (RX). The de-sensitization occurs since the receiver components have limited dynamic range compared to the difference between RX signal and interferer which can be as large as, e.g., 80 to 120 dB in the case of CDMA/WCDMA where the TX signal maximum output power is 28 dBm. A first order effect of large interferer power is P_{-1dB} compression, also called blocker P_{-1dB} compression. Therefore, some form of filtering mechanism is typically needed to attenuate the interferer power.

Figure 1-4 (b) shows the scenario where a receiver is affected by leakage of the large transmit power of its own transmitter called self-interference or transmitter (TX) leakage. This can happen when the receiver and transmitter share the same antenna using a duplexer. The duplexer typically has limited out-of-band attenuation and therefore the transmit power can leak to the receiver. A large TX modulated signal, even after duplexer isolation, is still very strong compared to the received signal. Self-interference can also occur when multiple radios are put together in a very small form factor where the antennas are physically located very close to each other as shown in Figure 1-4 (b).

1.2.2 Distortion Effects of Interference in Receiver

A receiver is a non-linear device or system and can typically be modelled as a 3rd-order power series. The high power of the interferer(s) causes gain compression and harmonic distortion (HD), intermodulation distortion (IMD), and cross-modulation distortion (XMD) in the receiver due to the non-linear characteristic. Below is a brief discussion of these non-linear characteristics.

1.2.2.1 Gain Compression

The non-linear behavior of the receiver can be modelled as a third-order power series by

$$y(t) = \alpha_1 x(t) + \alpha_2 x^2(t) + \alpha_3 x^3(t). \quad (1)$$

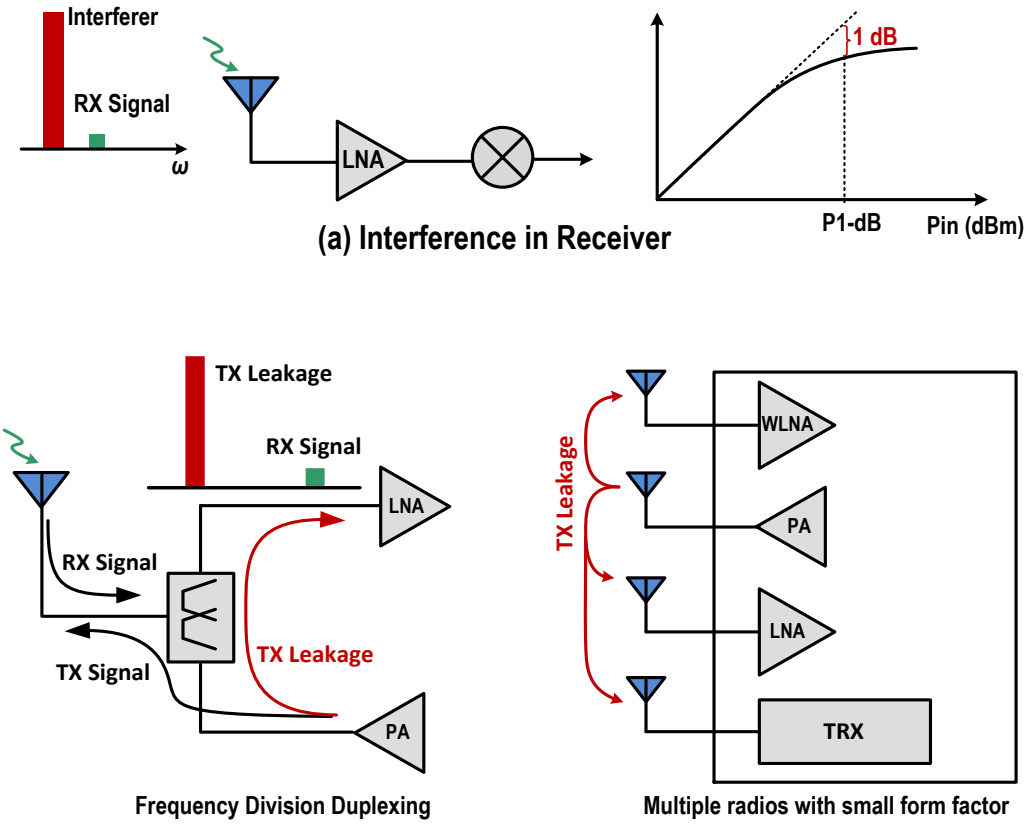

Figure 1-4: (a) Interference from nearby transmitter causing 1-dB compression and (b) Self interference (TX Leakage) from the transmitter.

Where α_1 can be considered a small signal gain if the other two terms are negligible for small output swings. When a sinusoidal signal $x(t) = A\cos\omega t$ is applied at the input of this non-linear system, the output consists of frequency components which are integer multiple of the fundamental ω. The output can be expressed as

$$y(t) = \alpha_1 A\cos\omega t + \alpha_2 A^2 \cos^2 \omega t + \alpha_3 A^3 \cos^3 \omega t. \tag{2}$$

$$= \alpha_1 A \cos \omega t + \frac{\alpha_2 A^2}{2}(1 + \cos 2\omega t) + \frac{\alpha_3 A^3}{4}(3\cos \omega t + \cos 3\omega t) \tag{3}$$

$$= \frac{\alpha_2 A^2}{2} + \left(\alpha_1 A + \frac{3\alpha_3 A^3}{4}\right)\cos \omega t + \frac{\alpha_2 A^2}{2}\cos 2\omega t + \frac{\alpha_3 A^3}{4}\cos 3\omega t. \tag{4}$$

The amplitudes of the second and third harmonics $\cos 2\omega t$ and $\cos 3\omega t$ are proportional to A_2 and A^3 respectively. For small signals, the amplitudes of the harmonics are negligible; however for large input amplitude A, the gain $(\alpha_1 + 3\alpha_3 A^2/4)$ at the fundamental $\cos \omega t$ varies substantially. For real nonlinear devices, α_1 and α_3 have opposite signs, resulting in a compressive behavior of the gain term $(\alpha_1 A + 3\alpha_3 A^3/4)$. In other words, as A increases, making the $\alpha_3 A^3$ more dominant, the gain of the nonlinear system decreases. This decrease in the gain is quantified by the 1-dB compression point as shown in Figure 1-5(a). In terms of power, the compression point is denoted as P_{-1dB} and is called Blocker P_{-1dB} when caused by a nearby large blocker or interferer. By setting the fundamental compressed gain to 1 dB less than the ideal gain:

$$20\log|\alpha_1| - 1\ dB = 20\log\left|\alpha_1 + \frac{3\alpha_3}{4}A_{-1dB}^2\right|. \tag{5}$$

$$\Longrightarrow \quad A_{-1dB} = \sqrt{0.145\left|\frac{\alpha_1}{\alpha_3}\right|}. \tag{6}$$

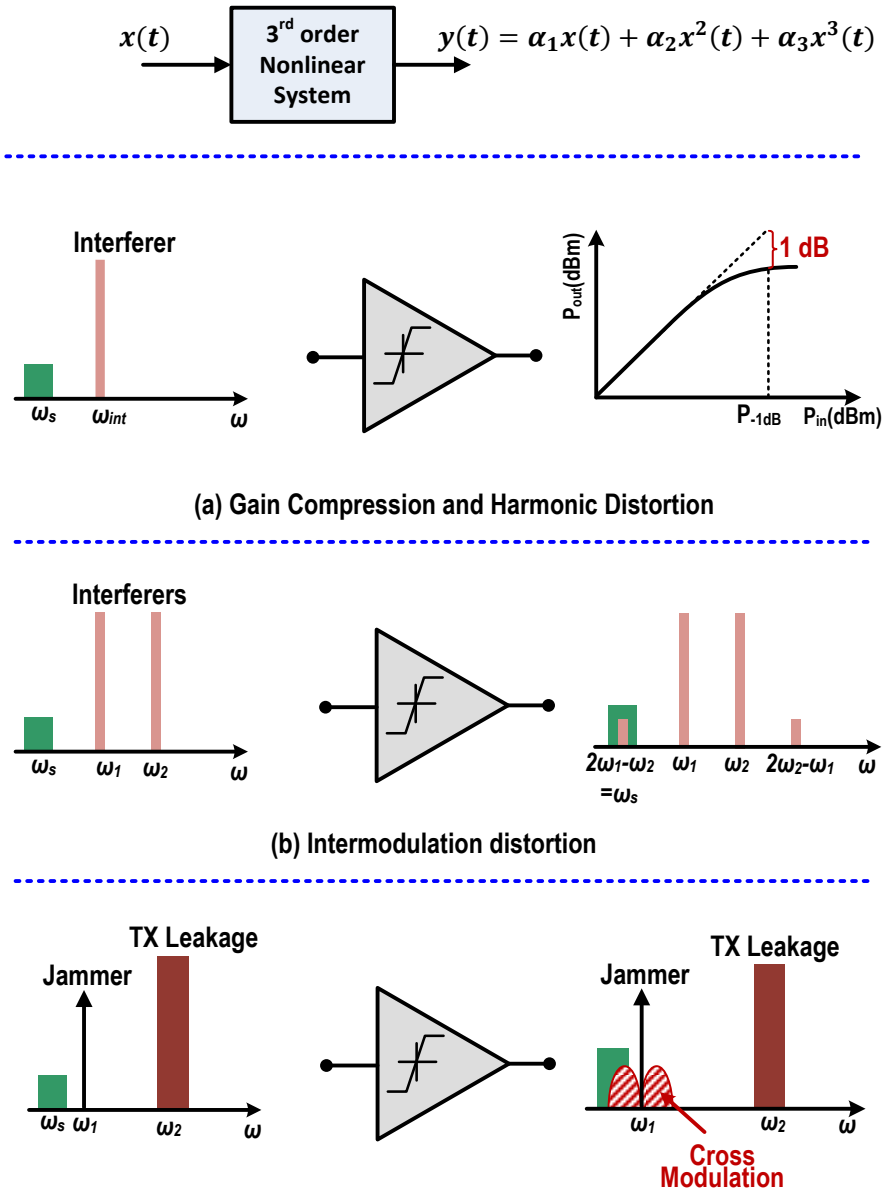

Figure 1-5: Effects of interference in a non-linear system, modelled as a power series, including (a) Gain compression, (b) Intermodulation distortions and (c) Cross-modulation distortion.

1.2.2.2 Intermodulation Distortions

Intermodulation distortion occurs when there are more than one tone present at the input of a nonlinear system. This type of distortion is commonly characterized using two tones. Figure 1-5(b) shows the intermodulation distortion resulting from two equally spaced interferers. Assuming two strong interferers $A_1 \cos \omega_1 t$ and $A_2 \cos \omega_2 t$ at the input of the nonlinear system then using (1)

$$y(t) = \alpha_1(A_1 \cos \omega_1 t + A_2 \cos \omega_2 t) + \alpha_2(A_1 \cos \omega_1 t + A_2 \cos \omega_2 t)^2$$

$$+\alpha_3(A_1 \cos \omega_1 t + A_2 \cos \omega_2 t)^3 \quad (7)$$

After trigonometric manipulation, the fundamental, second and third order intermodulation products can be writes as

$$\omega = \omega_1, \omega_2 : \left(\alpha_1 A_1 + \frac{3\alpha_3 A_1^3}{4} + \frac{3\alpha_3 A_1 A_2^2}{2}\right)\cos \omega_1 t + \left(\alpha_1 A_2 + \frac{3\alpha_3 A_2^3}{4} + \frac{3\alpha_3 A_2 A_1^2}{2}\right)\cos \omega_2 t)$$

$$\omega_1 \pm \omega_2 : \alpha_2 A_1 A_2 \cos(\omega_1 + \omega_2)t + \alpha_2 A_1 A_2 \cos(\omega_1 - \omega_2)t$$

$$2\omega_1 \pm \omega_2 : \left(\frac{3\alpha_3 A_1^2 A_2}{4}\right)\cos(2\omega_1 + \omega_2)t + \left(\frac{3\alpha_3 A_1^2 A_2}{4}\right)\cos(2\omega_1 - \omega_2)t$$

$$2\omega_2 \pm \omega_1 : \left(\frac{3\alpha_3 A_2^2 A_1}{4}\right)\cos(2\omega_2 + \omega_1)t + \left(\frac{3\alpha_3 A_2^2 A_1}{4}\right)\cos(2\omega_2 - \omega_1)t \quad (8)$$

IM₃–The two tones characterization is described in Figure 1-15(a) where the third-order intermodulation product A_{ID3} at frequency $2\omega_2 - \omega_1$ falls directly into band of interest and corrupts the signal of interest. For the two-tone test when the two sinusoids have equal amplitudes ($A_1 = A_2 = A$), the amplitude of the output third-order intermodulation product $A_{ID3}$is normalized to that of the fundamental A and is called relative IM_3 or just IM_3. From (8), IM_3 is given by

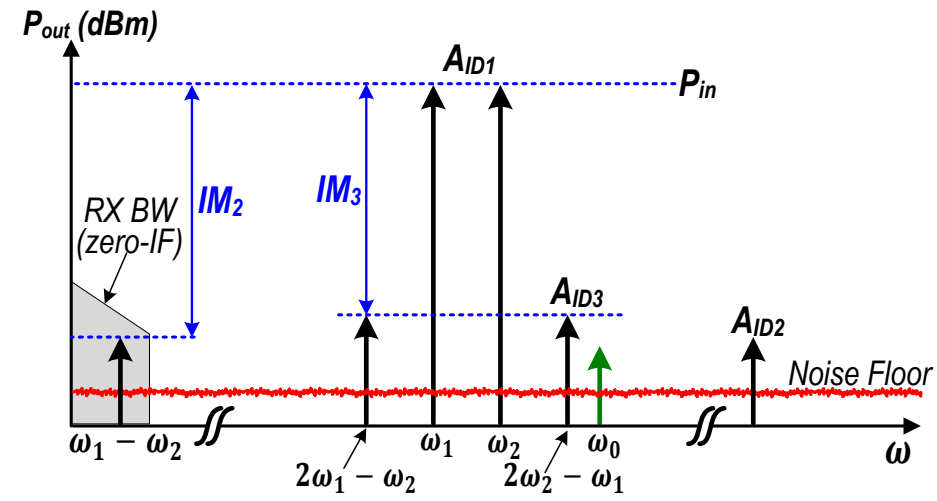

(a) Two-tones Intermodulation Products

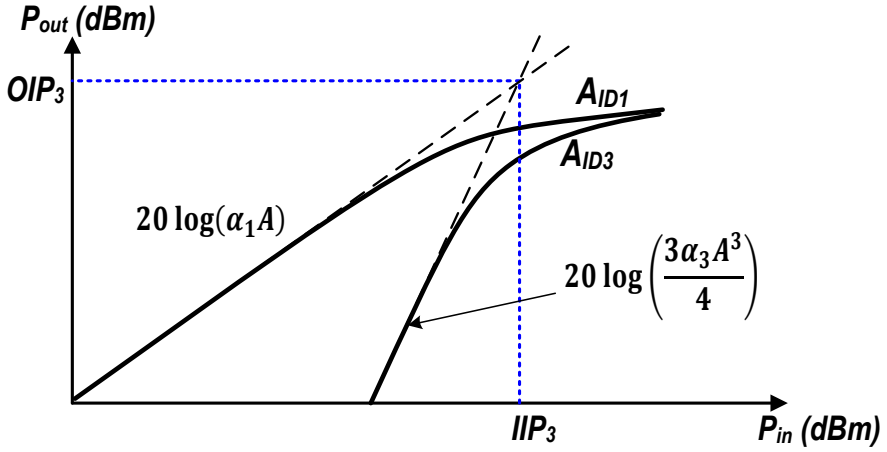

(b)Third Intercept Point (IP_3)

Figure 1-6: (a) Two-tone intermodulation products description and (b) Third intercept point-IIP_3

$$IM_3 = \frac{Amplitude\ of\ Third\ order\ Intermod.\ Product}{Amplitude\ of\ Fundamental} \tag{9}$$

$$\boldsymbol{IM_3} = \frac{A_{ID3}}{A_{ID1}} = \frac{3\alpha_3 A^3/4}{\alpha_1 A} = \frac{3\alpha_3 A^2}{4\alpha_1} \tag{10}$$

***IM₂*–**For the case of a zero-IF receiver architecture, where the RF signal is directly converted to baseband, second-order intermodulation products A_{ID2} fall directly into the down-converted signal band and thus can be harmful. IM_2 is characterized as

$$IM_2 = \frac{Amplitude\ of\ Second\ order\ Intermod.\ Product}{Amplitude\ of\ Fundamental} \tag{11}$$

$$\boldsymbol{IM_2} = \frac{A_{ID2}}{A_{ID1}} = \frac{\alpha_2 A^2}{\alpha_1 A} = \frac{\alpha_2 A}{\alpha_1} \tag{12}$$

Third Order Intercept Point – The relative IM_3 is meaningful only when the value of A is given. For a single measurement reference third-intercept point (IP_3) is used. From (8), we know that A_{ID3} increases in proportion to A^3, the $IP_3$is the intersection of extrapolated A_{ID1} and A_{ID3} when plotted in logarithmic scale as shown in Figure 1-15(b). Mathematically, A_{ID1} and A_{ID3} will have same magnitude for the input level A_{IP3}, also notated as A_{IIP3} to refer to the input-referred third-order intercept point.

$$A_{ID1} = A_{ID3} \tag{13}$$

$$|\alpha_1| A_{IIP3} = \frac{3}{4} |\alpha_3| A_{IIP3} \tag{14}$$

$$A_{IIP3} = \sqrt{\frac{3}{4}\left|\frac{\alpha_3}{\alpha_1}\right|} \tag{15}$$

1.2.2.3 Cross-Modulation Distortions

The modulation on the TX leakage or self-interference can also be transferred to jammer when these signals pass through a nonlinear system, thus corrupting the RX signal as shown in Figure 1-5(c). This type of distortion is called cross-modulation XMD. Mathematically, the input signal can be characterized as combination of jammer ($A_1 \cos \omega_1 t$) and TX leakage signal ($A_2 \cos \omega_2 t$).

$$x(t) = A_1 \cos \omega_1 t \; + \; A_2 \cos \omega_2 t \tag{16}$$

$$y(t) = \alpha_1(A_1 \cos \omega_1 t + A_2 \cos \omega_2 t) + \alpha_2(A_1 \cos \omega_1 t + \boldsymbol{A_2 \cos \omega_2 t})^2 + \alpha_3(A_1 \cos \omega_1 t + A_2 \cos \omega_2 t)^3 \tag{17}$$

Then the jammer frequency terms can be separated from (17)

$$y(t) = \left(\alpha_1 A_1 + \frac{3\alpha_3 A_1^2}{4} + \frac{3\alpha_3}{2}\boldsymbol{A_2^2}\right) A_1 \cos \omega_1 t + \cdots .. \tag{18}$$

If the leakage is a modulated signal i.e. $\boldsymbol{A_2(1 + mcos\omega_m t)}cos\omega_2 t$, then (18) becomes

$$y(t) = \left(\alpha_1 A_1 + \frac{3\alpha_3 A_1^2}{4} + \frac{3\alpha_3}{2}\boldsymbol{A_2^2(1 + mcos\omega_m t)^2}\right) A_1 \cos \omega_1 t + \cdots .. \tag{19}$$

$$y(t) = \left[\alpha_1 + \frac{3}{4}\alpha_3 A_1^2 + \frac{3}{2}\alpha_3 \boldsymbol{A_2^2}\left(\boldsymbol{1 + \frac{m^2}{2} + \frac{m^2}{2} cos2\omega_m t + 2mcos\omega_m t}\right)\right] A_1 \cos \omega_1 t + .. \tag{20}$$

From (20), it is evident that the modulation on the leakage signal is transferred to the jammer at ω_1. If the jammer is located very close to the desired signal, the TX modulation will corrupt the signal.

The effects of both intermodulation and cross modulation distortion IM_3 and IM_2 on the full-duplex transceiver are illustrated in Figure 1-7 where the distortions corrupt the received signal. Also shown in this figure is second-order intermodulation distortion IM_2 since the receiver consists of a zero-IF architecture.

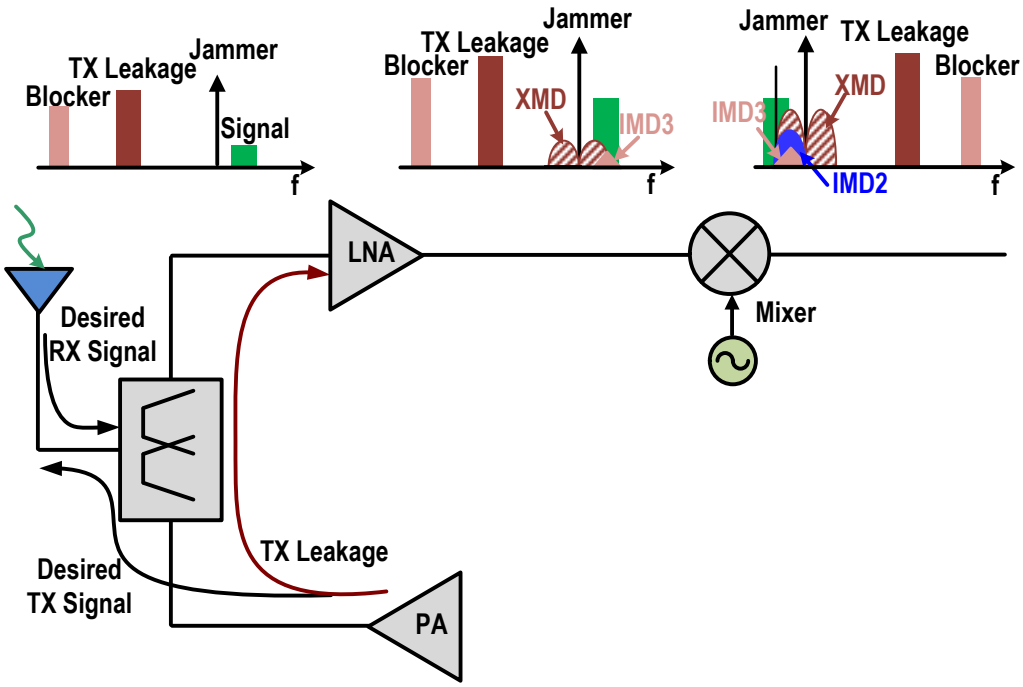

Figure 1-7: Effects of interference and self-interference on the receiver in a full-duplex architecture in terms of modulation distortions IM_2, IM_3 and XMD.

Filtering is needed to mitigate the effects of interference and self-interference. Depending on the system architecture and requirements, the filtering can be implemented at RF/microwave frequencies, intermediate frequencies (IF) or baseband frequencies, and in analog or digital domains. Implementing filtering at RF/microwave frequencies is advantageous, as it relaxes the requirements on subsequent components, but presents various challenges

1.3 Software Defined Radios and Applications

. The demand for the RF transceivers to cover wide range of frequencies and replace multiple radios has led to the emergence of the idea of Software Defined Radio (SDR). The original concept of SDR [4] is to down-convert a large RF spectrum using a wideband analog-to-digital converter (ADC) and perform the entire signal processing (generation, channelization, modulation, demodulation, error control etc.) in the digital domain using software, The term SDR was first introduced in [4] and related discussion, challenges and realization issues can be found in [5]-[8]. Figure 1-8 (a) shows the block diagram of an ideal SDR system. However, such SDR implementations historically have not been realistic, particularly in mobile platforms, due to interference requiring the ADC to have a very large dynamic range which comes at the expense of prohibitive power consumption in the current state of the art technologies. Furthermore, due to the continuous demands for increased data rates, communication systems are shifting to higher frequencies (microwave and millimetre-wave), making the requirements on the ADC even more challenging to meet. For the practical realization of an SDR system, system designers have converged towards a reconfigurable multi-standard approach, where a combination of antenna tuner, switched or tunable filters, and programmable frequency synthesizer are employed as shown in Figure 1-8 (b).

One of the main bottlenecks in the realization of SDR using a reconfigurable RF front-end is the filters which are unique per application using traditional off chip SAW and BAW technologies. A comparative study of BAW and SAW can be found in [9]. Though these technologies provide greater selectivity due to their high Q resonators, they are fixed frequency and occupy large area. Implementing SDR or multi-band reconfigurable radio operation under the presence of strong

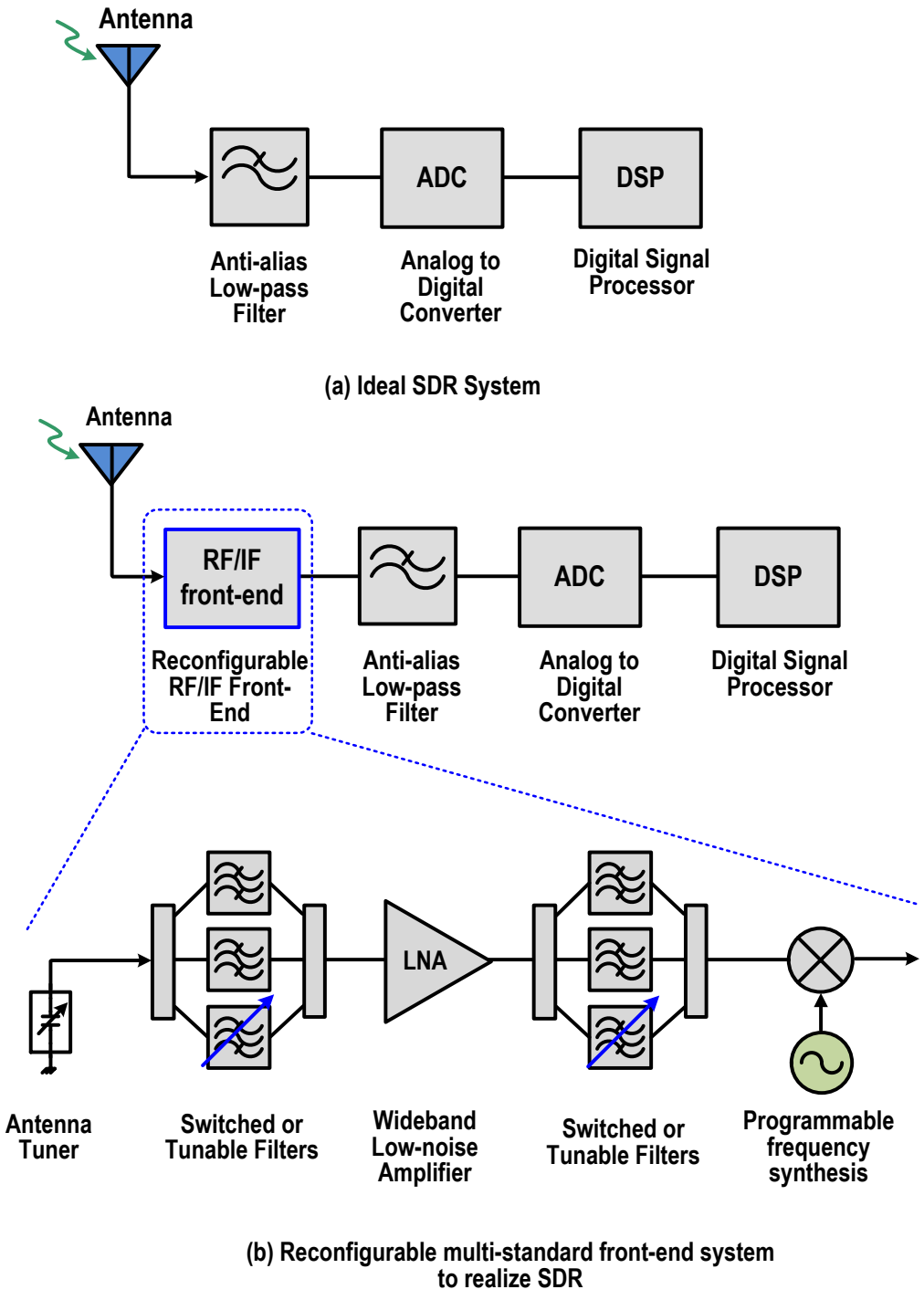

Figure 1-8: (a) An ideal SDR system and (b) reconfigurable multi-standard RF front-end system using a combination of antenna tuners, switched or tunable filters, and programmable frequency synthesizer to realize SDR.

interferers using theses off-chip technologies requires an array of fixed frequency filters along with a switching matrix to cover a large number of frequency bands. This will increase the cost and area of the whole system substantially and therefore is not a cost effective solution.

To realize the vision of a true SDR system with a single widely reconfigurable radio, tunable filters are a critical path moving forward. There are a number of off-chip solutions for tunable as well as dual-band band filters using RF MEMS, substrate integrated waveguide (SIW) cavities, and microstrip technologies. A survey of state of the art off-chip tunable and intrinsically switched filters using these technologies can be found in [10]. These solutions, however, are off-chip and thus suffer from similar cost effectiveness as switched BAW and SAW filters in terms of area, weight, and cost. The filters discussed by Chappell *et. al*. in [10] also face challenges in terms of tunability especially inter-resonator coupling control.

The tunability requirements of these filters creates challenges of its own for each of the implementation technologies mostly associated with frequency of operation. We define the tunability in terms of center-frequency tuning and 3-dB bandwidth tuning.

1.4 Overview of On-chip Filter Technologies

Integration of tunable filters in silicon IC technology can make it possible for a widely reconfigurable RF front-end system to be implemented on a single silicon die. This has resulted in tremendous interest in on-chip tunable filters, including N-path [11]-[27], discrete time [28]-[32] Q-enhanced LC [33]-[45], and Gm-C [31], [46]-[49] filters. Figure 1-9 shows basic form of on-chip 2nd-order bandpass filtering types. A simple passive LC filter with a voltage to current driver, which can be Q-enhanced using a –gm cell. The inductance in the LC tank can also be realized by a gyrator using Gm-C technique where the inductance is a function of the transconductance of the two cells $g_{m1}$and g_{m2} and the capacitor C_2. A 2nd-order BPF can also be implemented using a simple Op-Amp topology and using Sallen Key topology. Replacing the resistors by switched capacitor in the Op-Amp topology results in a switched capacitor BPF.

The majority of the N-path filters are narrowband/high Q and center-frequency tunable. The Q-enhanced filters in filters in [35]-[45] are either fixed frequency or tunable over a very small

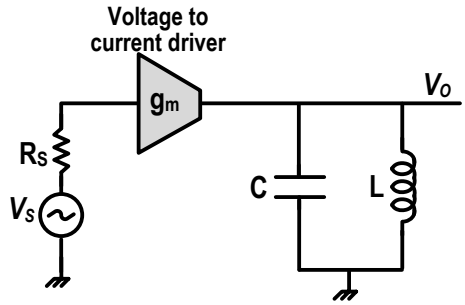

(a) 2nd-orrder BPF using inductor and capacitor with a driver

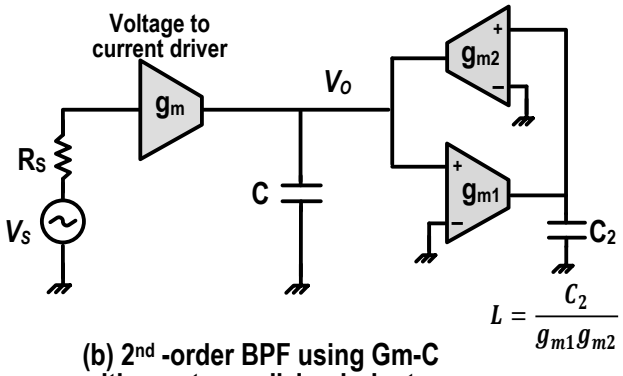

(b) 2nd -order BPF using Gm-C with gyrator realizing inductor

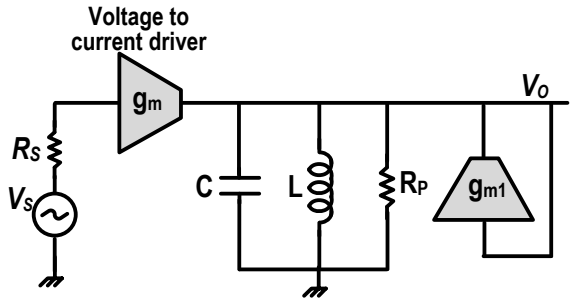

(c) 2nd-orrder LC BPF with Q-enhanced negative resistance -1/g_{m1}

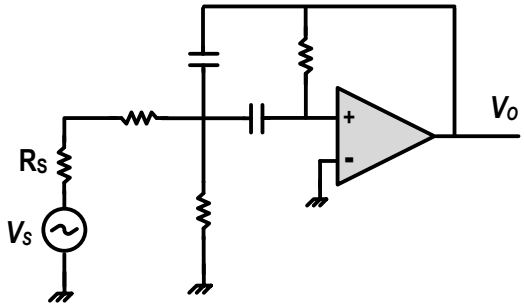

(d) 2nd -order BPF using Op-Amp and multiple feedbacks

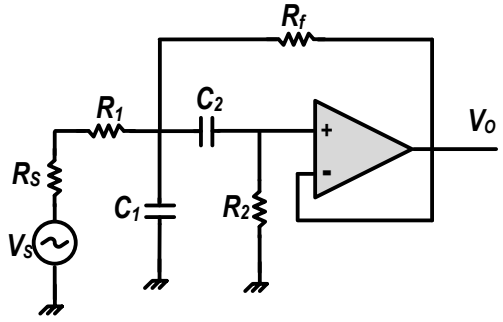

(e) 2nd -order BPF Sallen-Key unity Gain Topology

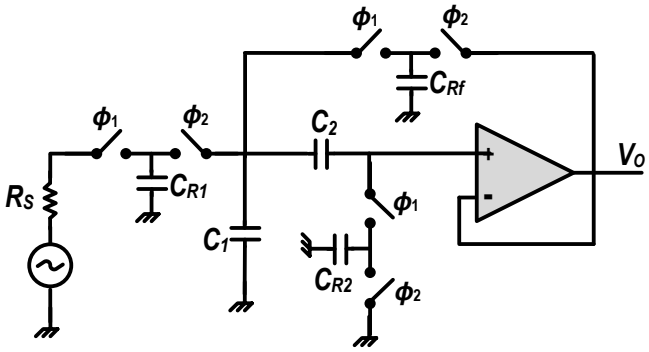

(f) 2nd -order Switched Capacitor Sallen-Key BPF

Figure 1-9: Types of on-chip bandpass filters (2nd-order) including LC, Gm-C, Q-enhanced LC, Op-Amp based, and switched capacitor.

range for the purpose of frequency trimming after manufacturing. Gm-C filters are implemented mostly at low RF frequency in the range of hundreds of MHz and at IF frequencies [46], [47]. This type of filter can also be used in conjunction with N-path where the baseband lowpass filter is based on the Gm-C topology [48]. Switched capacitors or discrete time filters are also used mainly for lower RF and baseband frequencies similar to Gm-C filters. The baseband of N-path filter can be a switched capacitor topology [28]-[32].

For high frequency GHz RF and microwave ranges, two filter topology stand out. The first is the N-path filter operating on clock driven switches and provide high Q filtering at RF frequencies. The second is Q-enhanced LC filter which may not be suited at lower RF frequencies below 2 GHz, due to large inductor size and associated low Q, but is very well suited at microwave frequencies above 2 to 20 GHz and beyond. We, therefore, discuss briefly about these two types of filters.

1.4.1 N-path filters

A basic N-path filtering block diagram consisting of 4-paths is shown in Figure 1-10(a) with 4 switches driven by 1/4 (25%) duty cycle non-overlapping clock phases. The baseband capacitor C_B makes a low pass filter in terms of voltage after down converting the RF current through switches. This baseband lowpass voltage signal is up-converted again using the same switches to realize a bandpass filtering characteristic at RF. The equivalent LC 2nd-order BPF is also shown in Figure 1-10(a). A generalized 4-path and M-path is also shown in Figure 1-10(b) and (c) where the driving impedance is shown in terms of a transconductance and its output impedance. The N-path out-of-band attenuation is a function of driving impedance and switch resistance. The ultimate out-of-band attenuation is better when driven by a current source with large output impedance. The baseband impedance is represented by $Z_{BB}(\omega)$ which can be any type of low pass filter and the RF impedance is represented by $Z_{in}(\omega)$. After complex signal processing involving Fourier transformation and convolution, the voltage at RF for an M-path can be approximated as

$$V_{in}(\omega) = I_{in}(\omega)(R_{SW} + M\left|a_{(2m+1)}\right|^2 I_{in}(\omega) \times [Z_{BB}(\omega - \omega_{LO}) + Z_{BB}(\omega + \omega_{LO})] \quad (1)$$

$$\Rightarrow \; Z_{in}(\omega) = 2R_{SW} + 2M\left|a_{1(2m+1)}\right|^2 \times [Z_{BB}(\omega - \omega_{LO}) + Z_{BB}(\omega + \omega_{LO})] \quad (2)$$

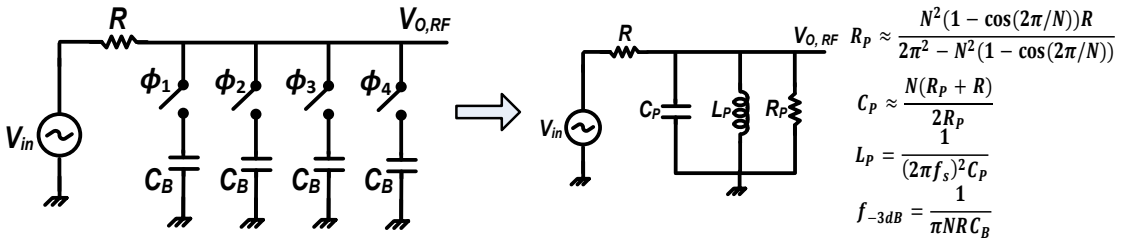

(a) 2nd-order 4-path passive BPF @ f_S with non-overlapping 25% duty cycle clocks and equivalent LC model

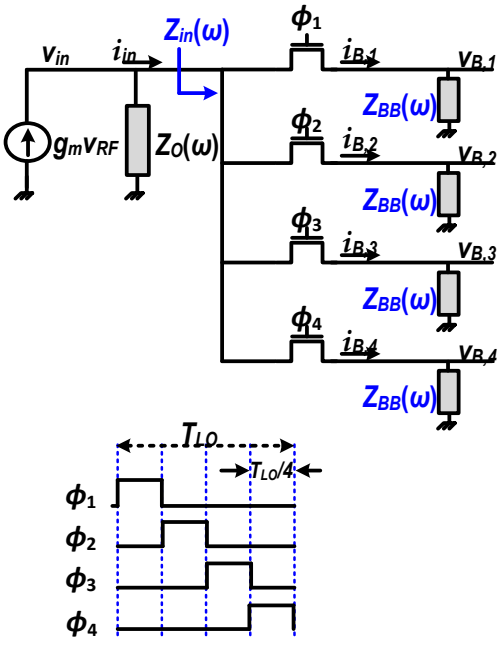

(b) 4-Path BPF with 4-phase clock

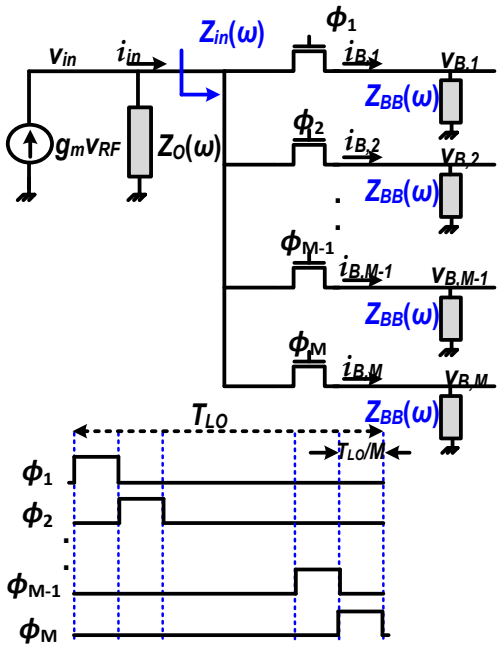

(c) M-Path Filter with M-phase clock

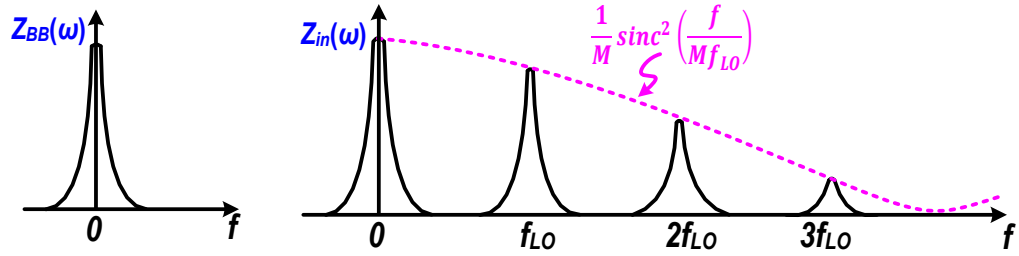

(d) M-path filtering at f_{L0} and its harmonics

Figure 1-10: (a) A 2nd-order 4-path passive filter, equivalent LC filter model, (b) a generalized 4-path filter model with 4-pahse clock, (c) a generalized M-path filter with M-phase clock, and (d) depiction of M-path filtering at RF with harmonics.

where

$$a_1 = \frac{\sin\left(\frac{\pi}{M}\right)}{\pi} e^{-j\frac{\pi}{M}} \Rightarrow |a_1|^2 = \frac{sin^2\left(\frac{\pi}{M}\right)}{\pi^2}$$

$$Z_{in}(\omega) = 2R_{SW} + \frac{2M}{\pi^2} sin^2(\frac{\pi}{M}) \times [Z_{BB}(\omega - \omega_{LO}) + Z_{BB}(\omega + \omega_{LO})]. \quad (3)$$

The harmonic filtering for an M-path is depicted in Figure 1-10(d) highlighting the sinc function. For a 4-path filter, the input impedance can be written as

$$a_1 = \frac{\sin\left(\frac{\pi}{4}\right)}{\pi} e^{-j\frac{\pi}{4}} \Rightarrow |a_1|^2 = \frac{sin^2\left(\frac{\pi}{4}\right)}{\pi^2}$$

$$Z_{in}(\omega) = 2R_{SW} + \frac{4}{\pi^2} \times [Z_{BB}(\omega - \omega_{LO}) + Z_{BB}(\omega + \omega_{LO})] \quad (4)$$

Figure 1-11 shows different architectures of N-path filters. For improved out-of-band attenuation, and to decouple the attenuation relationship to the driving impedance and switch resistance, a passive N-path containing twice the no. of switches can be implemented. In this case two different set of switches are used for down-conversion and up-conversion after baseband filtering. An active N-path is usually preceded by a low-noise transimpedance amplifier (LNTA). For a passive or an active N-path, the output at baseband node can be used, thus functioning as a mixer as well as shown in Figure 1-11. A mixer first receiver with 2nd-order 4-path passive BPF with basedband I/Q outputs as implemented in [14] is also shown.

The baseband low pass filter of an N-path filter can be passive/active continuous time or discrete time. The based band of an N-path filter can be a switched RC low pass filter or Gm-C filter. In [27] and [48], an N-path topology implemented where the baseband amplifier is a Gm-C filter. Similarly, [28] is an example of 4-path filter where the baseband is a high-order IIR filter with harmonic rejection.

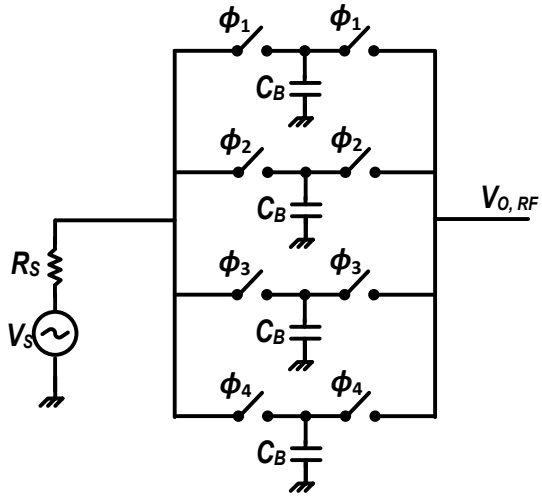

(a) 2nd-order 4-path passive BPF with improved out-of-band attenuation

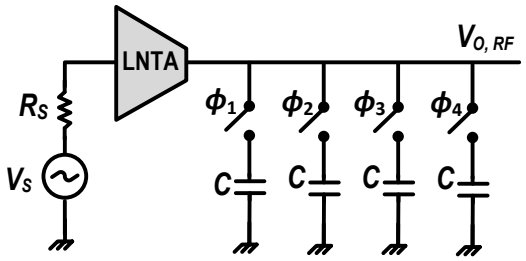

(b) 2nd-order 4-path Active BPF with Low-Noise Transimpedance Amplifier (LNTA)

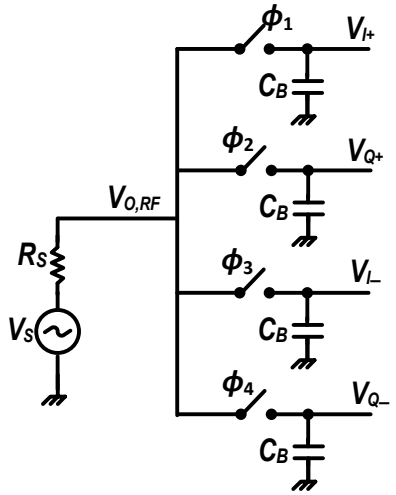

(c) 2nd-order 4-path passive BPF with baseband I/Q outputs also called mixer-first receiver

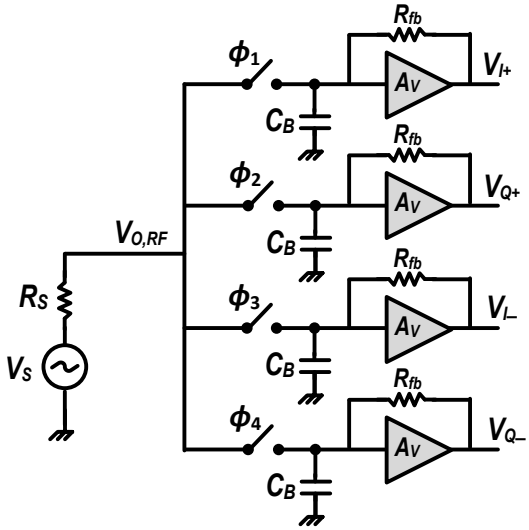

(d) Mixer-first receiver 4-path passive BPF with baseband I/Q outputs similar to [14]

Figure 1-11: Types of on-chip N-path bandpass filters (2nd-order) including 4-path path passive, 4-path active with LNTA, 4-path passive with baseband output, mixer first 4-path passive with baseband outputs.

1.4.2 Q-enhanced LC filters

1.4.2.1 2nd-order LC bandpass Filtering

Figure 1-9 (a) shows simple and straightforward implementation of a 2nd-order LC bandpass filter with a transconductance as driver. This uses one parallel resonator or tank, which provides two negative frequency poles. At low RF frequencies, in the range of 100s of MHz, the inductor size is very large as well as suffer from low Q. Figure 1-9 (b) shows implementation of inductor as gyrator using Gm-C architecture. Since on-chip spiral inductors typically have very low Q due to the sheet resistance of the inductor metal traces, substrate losses, and other effects. Consequently, on-chip inductors in LC filters require Q-enhancement. The Q of the tank is essentially equal to the quality factor of the inductor having a loss R_S at resonance frequency, i.e. $Q_0 = \omega_0 L/R_s$. Using series to parallel impedance transformation, the inductor with series loss can be represented as parallel inductor L_P with parallel loss R_P as shown in the Figure 1-9 (c). The Q_0 and R_P can be expressed as:

$$Q_0 = \frac{1}{R_S}\sqrt{\frac{L}{C}}, \qquad R_P = (1 + Q_o^2)R_S \approx \frac{\omega_0^2 L^2}{R_S} \tag{5}$$

and

$$L_P = \left(\frac{1 + Q_0^2}{Q_0^2}\right) L_S \tag{6}$$

A negative resistance, to cancel the equivalent parallel loss R_P, can be implemented using a transconductor with positive feedback as shown in the Figure 1-9 (c) . The equivalent parallel resistance R_{EQ} and the enhanced quality factor Q_{EN} are expressed in (7) and (8) respectively. The quality factor Q can be made very high when $gmR_P \to 1$. However the $-g_m$ needs to be precisely controlled to avoid oscillation which happens when the R_{EQ} becomes negative. i.e. $g_m R_P \geq 1$.

$$R_{EQ} = R_P \parallel \left(-\frac{1}{g_m}\right) = \frac{R_P}{1 - g_m R_P} \tag{7}$$

and

$$Q_{EN} = \frac{R_{EQ}}{\omega_o L_P} = \frac{Q_0}{1 - g_m R_P} \tag{8}$$

1.4.2.2 Higher-order LC bandpass Filtering

A 2nd-order LC BPF using parallel RLC circuit is simple to implement on-chip with lower complexity, easier frequency tuning and Q control, appropriate for very high Q or narrowband systems However, this approach is not optimal for wideband systems where large bandwidth (small Q) will have limited out-of-band attenuation. For a flat passband, bandwidth control and large out-of-band attenuation, higher order filtering is needed. Some common configurations for higher-order filters are π ladder structures, coupled resonators with capacitive or inductive coupling, as shown in Figure 1-12. These higher-order structures can give superior performance; however, their on-chip realization can be very complex in terms of number of components, frequency tuning, precise coupled component value and Q compensations for each inductor. Additionally, there can be a large difference in range between resonant and coupled component values limiting their on-chip realization. For example, C_1 and C_{12} in Figure 1-12 (b) are related as $C_{12} = k_{12}C_1/Q_{BPF}$ [34]. Coupling coefficient k_{12} is a small value e.g. 0.711 for Chebyshev 0.1 dB ripple filter. For a BPF Q of 30, the C_{12} is 42 times smaller than C_1. For magnetic coupling using transformer in Figure 1-12 (c), the bandwidth is determined by the coupling coefficient k, which is difficult to control.

1.4.3 Filter Tuning

1.4.3.1 Center-Frequency

For the configurable multi-band multi-standard RF front-ends, center frequency tuning of BPFs is the primary requirement. A large center-frequency tuning range on the order of octave or higher is advantageous to cover multiple bands. However, center frequency tuning complexity is a function of the filter-order. The traditional ladder filter theory for higher order filters is intended for fixed frequency filters, where there are number of resonators coupled together in series or parallel fashion. An nth-order filter will require an N number of resonators and therefore N tuning controls of either L or C is required. Therefore, for on-chip tunable filtering, the preference is to make to the filter simple or smaller-order filter. Most commonly used component to tune the frequency is on-chip varactor for LC or Q-enhanced LC filters, where the center frequency coverage is a square root function of the varactor capacitance range. A varactor is also used to tune

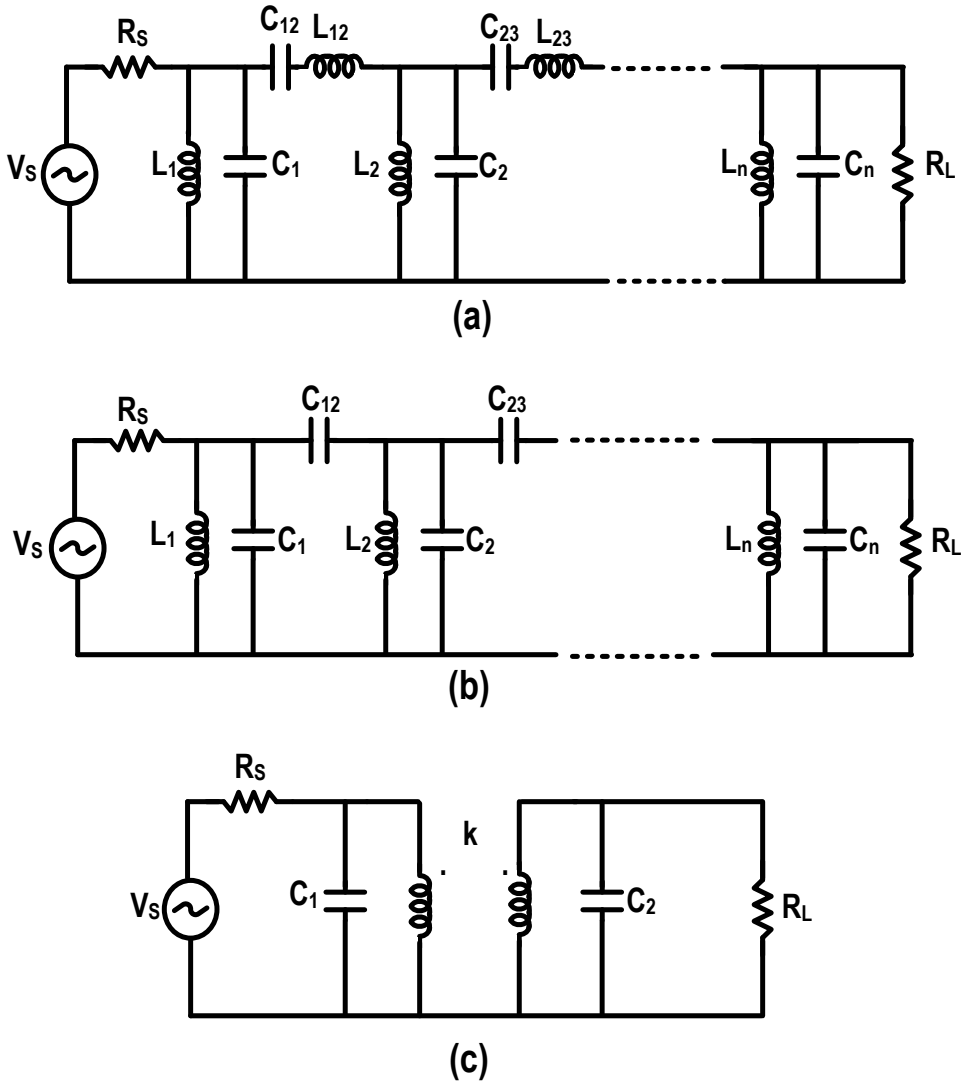

Figure 1-12: Common high-order band-pass filters configurations (a) an LC ladder structure, (b) a capacitive-coupled resonators and (c) Magnetic-coupled resonators.

the C in the Gm-C filters to change the center frequency directly or change the inductance indirectly to tune the center frequency. Changing the transconductance g_m by current or biasing can also be used to vary the inductance to change the center frequency. For N- path filters, frequency tuning is achieved by changing the clock frequency. N-path provides filter at RF frequency equivalent to the clock frequency and there for a large frequency tuning can be achieved by changing the clock frequency. Contrary to LC or Q-enhanced LC filtering, N-path filtering tuning for is a function of power for N number of paths. Foe example the power consumption becomes twice for an 8- path filter compared to 4-path simple because the clock phase generation and driver circuitry has to generate twice the number of phases as well as drive twice the number of MOSFET switches.

1.4.3.2 3-dB Bandwidth

Traditionally, filter theory is mostly focused on narrowband filtering. For on-chip filter frequency tuning, a simple BPF structure is preferred e.g. a 2nd-order parallel LC resonator. The complexity becomes worse for the bandwidth tuning of higher-order filter since all the resonators and coupling components will need tuning mechanism. For coupled LC filters which are cascaded, the 3-dB bandwidth is very limited since coupling in cascaded resonators affects each resonator. In the case of N-path filters, most of the reported filters are equivalent of 2nd-order BPF with a capacitor at the based serving as lowpass RC filter together with switches. N-path filters directly translate the baseband bandwidth to RF which is advantageous for narrowband high Q filtering but this makes realizing a wideband filter at baseband and transferring it to RF very challenging. On-chip large, tunable 3-dB bandwidth is therefore very challenging for both Q-enhanced as well as N-path filters.

1.4.4 Filter choice: N-path versus Q-enhanced LC

Although N-path filters have shown significant promise for on-chip realization of tunable filters with good performance, they have mostly been limited to operating frequencies of ~3 GHz and below. This frequency limitation is due to the challenge of creating accurate multiphase clocks at higher RF frequencies beyond 3 GHz. For low-IF or zero-IF receivers, the power consumption of N-path filter is a function of operating frequency since multiple phases of the clock equal to RF

signal frequency are needed. Such multiphase clocks also result in excessive dynamic power consumption. Moreover, for mixer-first architectures [14] where N-path filter provides filtering and down conversion at the same time, as well as when the N-path is used as a front-end filter before the LNA [12], the clock signal can leak at relatively high levels to the antenna. Such clock leakage may not be desirable in certain systems like tracking and detection.

Most recently, N-path filters at microwave frequencies of 6 GHz and 12 GHz have been reported [24], [25]. These filters have very large frequency tuning ranges accomplished by LO (clock) tuning; however, with increasing operating frequency, the out-of-band rejection decreases progressively to 20 dB or lower. This is due to the filtering dependency on the clock's duty cycle which gets distorted at higher frequency since the rise and fall times are significant fraction of the total clock pulse width. In the case of Q-enhanced LC filters, the filter shaping specifically is not dependant on the frequency and associated parasitics. Additionally, N-filtering at high frequencies comes at the expense of large power consumption compared to filtering below 2 GHz. The power consumption will also increase substantially to achieve higher out-of-band rejection using higher-order structures by cascading or other techniques,. For example, for a 4^{th}-order BPF realization through cascading two N-path filters or for using separate switches for down-conversion and up-conversion (Figure 1-11(a)), for improved out-of-band attenuation, the power consumption will be twice that of a 2^{nd}-order simply because the clock-phases generation circuit has to drive twice the number of switches. N-path filters with Discrete-Time (DT) baseband signal filtering approaches are reported in [28] – [32]. These filters also require multiphase clocks and hence the associated pros and cons similar to N-path filters. On the contrary Q-enhanced LC filtering does not suffer from the power consumption scaling with operating frequency and can actually have reduced power consumption as the frequency increases since the Q-enhanced negative resistance generation will use less power due to high Q inductors at higher frequencies.

Previous attempts to realize Q-enhanced LC-filters around 2 GHz and below have limitations including lack of frequency tuning, bandwidth (BW) or Q-tuning, and limited dynamic range (DR) [36]-[45]. Varactor-based tunable LC filters have the particular advantage of fast frequency tuning necessary for applications like tracking and detection. On-chip high frequency integrated band-pass filters are therefore very attractive in terms of integration resulting in small form factor. Meanwhile, higher-order filtering is always desirable for better frequency selectivity but when

cascading multiple resonators in conventional ladder or coupled resonator filters for better frequency selectivity, dynamic range degrades progressively due to increasing passive component losses.

In conclusion, Q-enhanced LC filters are a promising option at microwave and higher frequencies, particularly given that the required inductor size gets smaller and inductor Q increases as frequencies scales. Additionally, achieving larger 3-dB bandwidths and with tunability is also possible, to be discussed further in Chapter 2, and somewhat less complicated in terms of higher-order and Q tuning at the same time.

1.4.5 Applications of the Q-enhanced LC Filters

Figure 1-13 is a block diagram of a receiver with proposed tunable filter scope which includes a widely center frequency tunable 4^{th}-order band-pass filter (BPF) and a band-reject or band-stop filter (BSF). Apart from center frequency tenability is the large 3-dB bandwidth tuning from narrowband like 1~2% fractional bandwidth to wideband of 20~25% fractional bandwidth. The main application space of the proposed tunable/reconfigurable filters are emerging Software Defined Radio architectures as illustrated in Figure 1-8 as well as Radar receivers. For accommodating a higher input compression level, the existing radar receiver protection (RxP) module in Figure 1-14 (a) includes a high power limiter followed by a filter and a low power limiter before the GaAs-based receiver typically [50]. The pre-TR limiters are usually made with high power diodes housed in a bulky tube structure filled in with a retroactive gas to facilitate plasma discharge in the gas tube and thus to enhance breakdown process [50]. Figure 1-14 (b) shows an advanced concept RxP to reduce the form factor of the RxP module – by leveraging recent advances in high breakdown GaN process, the tunable (for gain, bandwidth, and operation frequency) GaN LNA can attenuate out-of-band signals with flexible dynamic range control. This allows the integration of the following receive module in a low-breakdown but cost- effective silicon process, reducing the size, weight and cost factors of the radar systems. The proposed silicon filter is to be used at the very front-end of the silicon receiver module following the external GaN LNA to provide further filtering-out of interferers and thus to relieve the dynamic range and associated power dissipation issues in the silicon receivers.

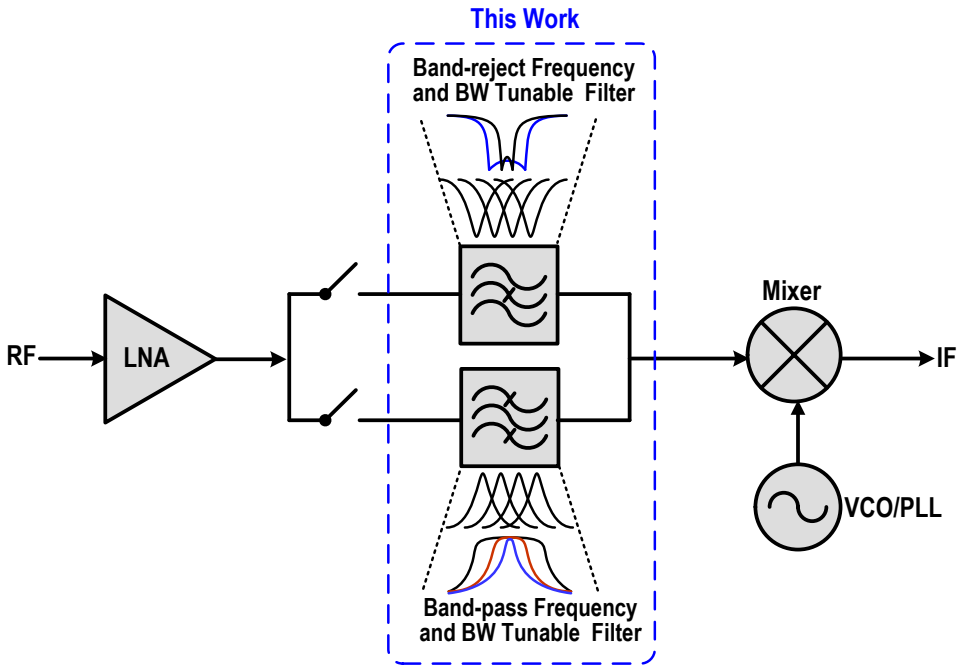

Figure 1-13: Block diagram of the receiver with proposed tunable filters for interference mitigation.

1.5 Integrated Filters Performance Characterization

Integrated tunable filters performance characterization is somewhat different from the traditional off-chip filters where the two main performance parameters are insertion loss and linearity. On-chip filters employ active components and therefor their noise contribution and linearity is characterized for the in-band. Additional they are also characterized for out-of-band linearity compared to off-chip passive filters where the out-of-band linearity is direct function of out-of-band attention. For example, at a certain offset frequency, the linearity in terms of P_{-1dB} is improved by the attenuation for off chip filters. This is not the case for integrated filters where the out-of-band linearity can be limited by the active components. These performance parameters are briefly explained in this section.

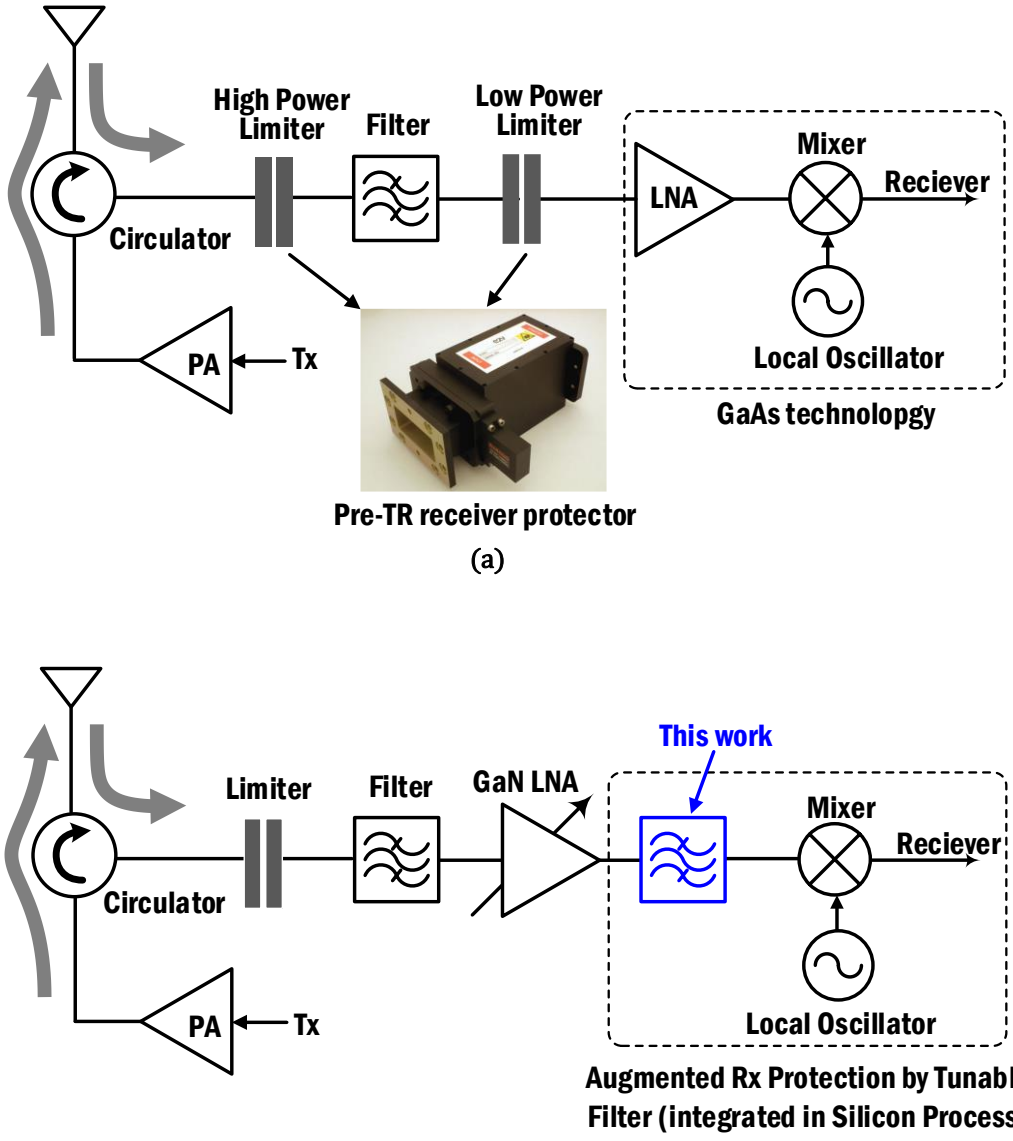

Figure 1-14: . Radar receiver protection (RxP) modules: (a) conventional RxP with bulky pre-TR power limiters and (b) advanced RxP by leveraging high breakdown GaN LNA for a low-volume RxP.

1.5.1 In-band Dynamic Range

Noise Figure and linearity in terms of P_{-1dB} are the key in-band performance parameters for active filters. NF and input P_{-1dB} limit the Dynamic Range (DR) of the filter. The normalized DR which is the ratio of in-band 1-dB input compression point to the input-referred noise-floor with 1-Hz BW [44] and can be expressed mathematically in dB as

$$DR = 174 + P_{-1dB} - NF \tag{8}$$

1.5.2 Out-of-band (OOB) Linearity

For active filters, the Out-of-band linearity characterization is very important to capture the interference effect on the filter and all other active components in the receiver. Figure 1-15 shows the characterization approach for the OOB IIP3 at an offset frequency of Δf where the interference is present. Two tones spaced by Δf when placed at an offset frequency of Δf from the center frequency create an in-band intermodulation tone. This gives the filter linearity characterization in terms of IIP3 when the two tones are swept outside of the filter 3-dB bandwidth. For sufficiently large offset the OOB IIP3 eventually saturates. Similarly, the OOB Blocker suppression or P_{-1dB} can be characterized when a blocker tone is located at offset frequency Δf. The power of the blocker tone is then swept causing the in-band response (signal tone) to compress as shown in Figure 1-16. The associated 1dB compression power level is the OOB Blocker P_{-1dB}.

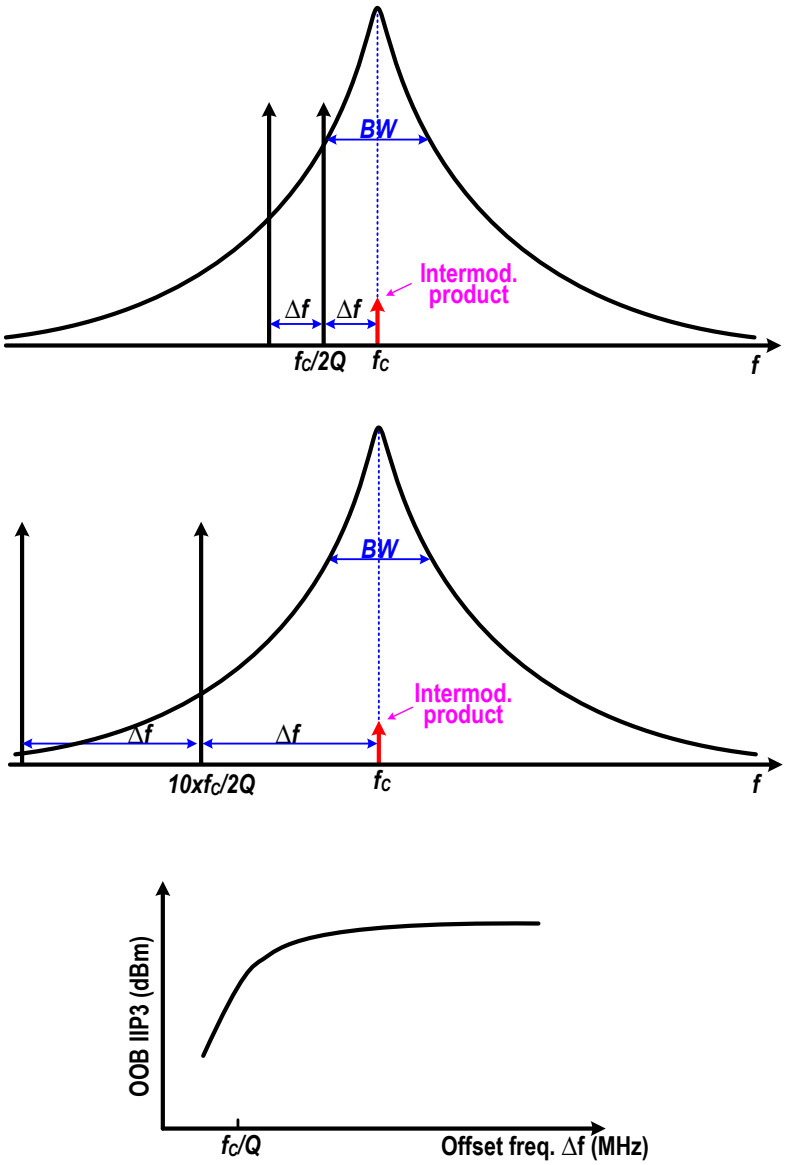

Expected OOB IIP3 response shape for varying the offset frequency of two tones

Figure 1-15: OOB IIP3 Characterization with two interference tones.

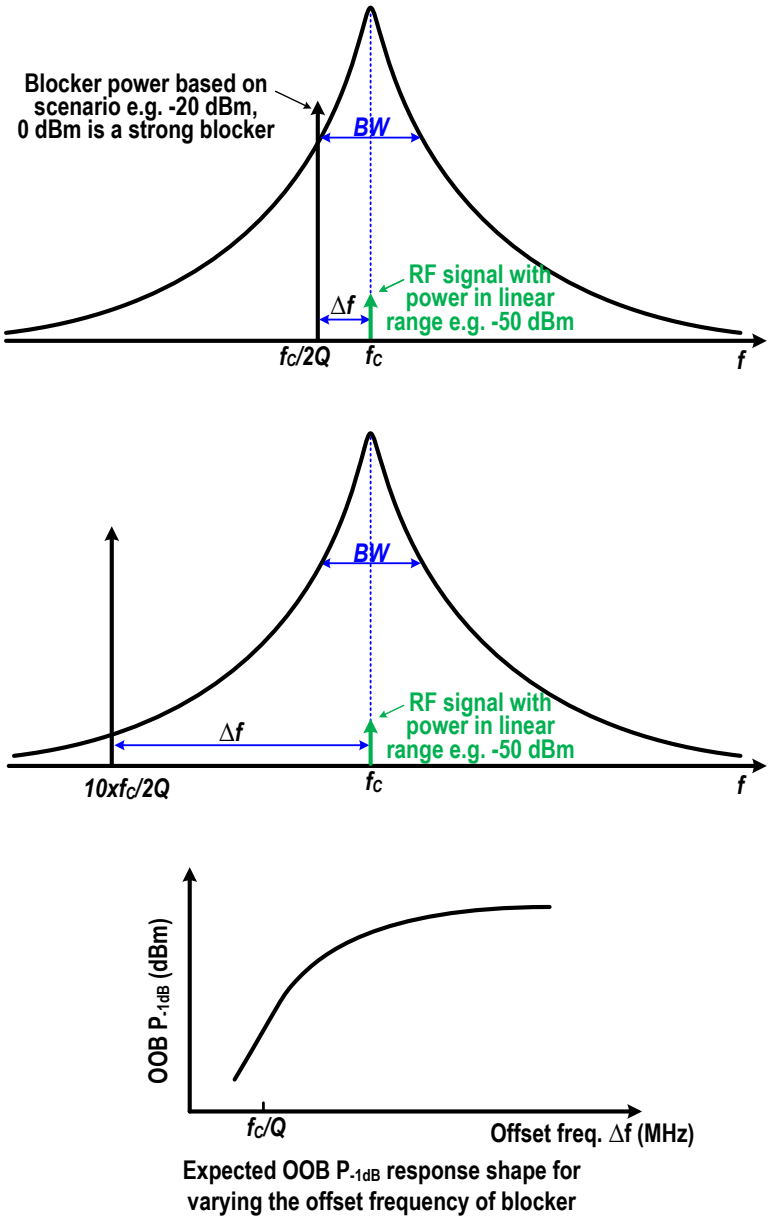

Figure 1-16: OOB Blocker P_{-1dB} Characterization with one interference tone and one small signal tome.

1.6 Summary and Dissertation Organization

SDR and reconfigurable radios require integrated tunable filters. Q-enhanced LC filters offer advantages at microwave frequencies and beyond. Apart from the small area, these filters can provide center frequency tuning as well as the bandwidth tuning.

This chapter has given detailed background on the tunable filtering requirement for reconfigurable RF front-ends and the motivation for designing Q-enhanced LC filtering at higher microwave frequencies range of 4~20 GHz. The remaining chapters of this dissertation have been organized as follows.

In Chapter 2, the 4^{th}-order BPF synthesis using two parallel 2^{nd}-order BPFs is introduced along with proposed design equations in terms of bandwidth, ripple magnitude, and spacing between the two BPFs. A system level linearity and noise analysis is presented highlighting the dynamic range benefits of the proposed filter. Finally, an introductory analysis of on-chip varactors for frequency tuning is presented.

In Chapter 3, the tunable 4^{th}-order BPF implementation detail is described with measured results. The circuit is designed in 130 nm SiGe BiCMOS technology with frequency tuning and Q tuning functionality resulting in large fractional bandwidth tuning. A circuit level noise analysis including model and verification is also presented. Detailed measurements of the fabricated chip are presented including S-parameters, noise figure, in-band linearity, and out-of-band linearity. The measurements demonstrate octave range frequency tuning as well as fractional bandwidth tuning from 2% to 25%, first ever on-chip wide bandwidth tuning.

In Chapter 4, a proposed improved switched varactor linearization scheme is described. Modeling and simulations are presented to verify the linearity improvement of the switched varactor control tuning technique. A 2^{nd}-order BPF with digital control bits for varactor tuning including decoding logic and designed level shifters to drive the varactors is fabricated and measured results are presented.

In Chapter 5, two techniques to achieve dual-band filtering using parallel synthesis techniques are proposed. The proposed technique is implemented at X and Ku bands in 130nm SiGe BiCMOS.

The fabricated chip is measured showing the dual-band filtering and the performance parameters.

In Chapter 6, a tunable true wideband high-order band-reject filtering technique is proposed for on-chip implementation. Simulation results are presented demonstrating the band-rejection and frequency tuning. The proposed technique is fabricated in 130 nm SiGe BiCMOS technology.

In Chapter 7, conclusion and contributions of this dissertation work are described. Finally, recommendations for the future direction of this research work are presented.

Chapter Two: **Tunable 4th-Order BPF Analysis**

2.1 Introduction

This chapter introduces the proposed tunable 4th-order BPF architecture at the block diagram level with a discussion on derived design equations, noise analysis and linearity analysis. The 4th-order BPF presented in this paper is based on a synthesis technique where subtraction of two identical 2nd-order LC-tank responses, with each resonator tuned at a slightly different center frequency, effectively shapes a 4th-order BPF response [27]. Thus, the filter can maintain the 2nd-order BPF DR while achieving the 4th-order filter selectivity [33]. The chapter also covers a basic analysis of the employed tuning varactors and their associated parameters such as tuning range and quality factor.

2.2 4th–order Filter Design Analysis

2.2.1 System Analysis

Figure 2-1 shows the 4th-order filter synthesis method intuitively, where two band-pass filters

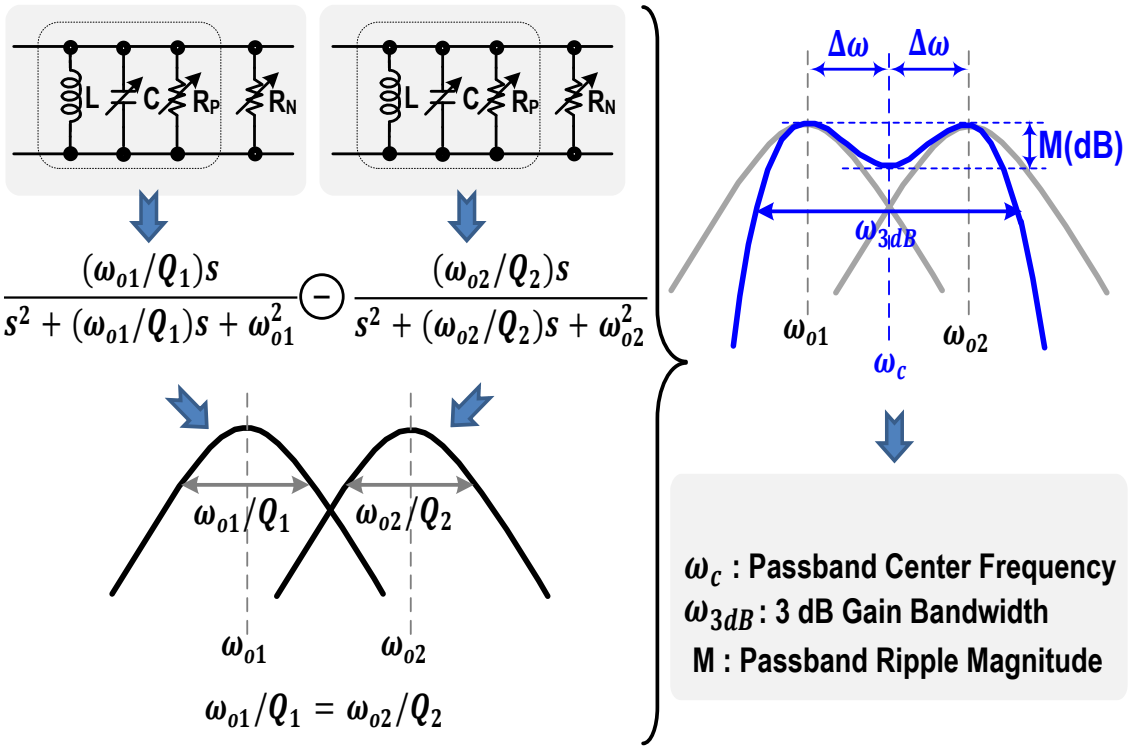

Figure 2-1: Synthesizing a 4th-order bandpass response by subtracting two identical 2nd-order resonators each tuned at slightly different resonance frequency.

or parallel resonators with close by center frequencies ω_{01} and ω_{02} are subtracted. For sufficiently high Q resonators, the frequency responses of the resonators undergo a sharp phase transition at their individual center frequencies ω_{01} and ω_{02}. For the regions below ω_{o1} and above ω_{o2}, the two characteristics will be subtracted. In-between the two resonance frequencies, the phases are opposite and therefore the characteristics will add to form a pass-band. Mathematically, the transfer function of the subtraction can be written as

$$H(s) = \frac{\left(\frac{\omega_{01}}{Q_1}\right)s}{s^2 + \frac{\omega_{01}}{Q_1}s + \omega_{01}^2} - \frac{\left(\frac{\omega_{02}}{Q_2}\right)s}{s^2 + \frac{\omega_{02}}{Q_2}s + \omega_{02}^2} \tag{1}$$

where ω_{01} and ω_{02} are the center frequencies of individual 2[nd]-order band-pass filters. If both band-pass filters have equal bandwidth i.e. $\omega_{01}/Q_1 = \omega_{02}/Q_2$, then (1) becomes

$$H(s) = \frac{\omega_{01}\omega_{02}\left(\frac{\omega_{02}}{Q_1} - \frac{\omega_{01}}{Q_2}\right)s}{\left(s^2 + \frac{\omega_{01}}{Q_1}s + \omega_{01}^2\right)\left(s^2 + \frac{\omega_{02}}{Q_2}s + \omega_{02}^2\right)} \ . \tag{2}$$

The relations between ripple magnitude, total bandwidth, bandwidth of each resonator and spacing between them are derived. This derivation is started by substituting $s = j(\omega_1 + \Delta\omega)$ and $s = j(\omega_2 + \Delta\omega)$ in (2), resulting in

$$H(s) = \frac{{j\omega_1}/{Q_1}\,(\omega_1 + \Delta\omega)}{{j\omega_1}/{Q_1}\,(\omega_1 + \Delta\omega) - 2\omega_1\Delta\omega - \Delta\omega^2} - \frac{{j\omega_2}/{Q_2}\,(\omega_2 - \Delta\omega)}{{j\omega_2}/{Q_2}\,(\omega_2 - \Delta\omega) + 2\omega_2\Delta\omega - \Delta\omega^2} \tag{3}$$

We are interested in calculating the ripple M_r in the passband, which can be expressed as follows, ignoring $\Delta\omega^2$ in the denominator, since $\Delta\omega$ is small compared to ω_{01} and ω_{02}

$$M_r(s) = \frac{1}{1 + j2Q_1\left(\frac{\Delta\omega}{\omega_1 + \Delta\omega}\right)} - \frac{1}{1 - j2Q_1\left(\frac{\Delta\omega}{\omega_2 - \Delta\omega}\right)} \tag{4}$$

Approximating

$$\left(\frac{\Delta\omega}{\omega_1 + \Delta\omega}\right) \approx \left(\frac{\Delta\omega}{\omega_1}\right), \qquad \left(\frac{\Delta\omega}{\omega_2 - \Delta\omega}\right) \approx \left(\frac{\Delta\omega}{\omega_2}\right)$$

(4) becomes

$$M_r(s) = \frac{1}{1 + j2Q_1\left(\frac{\Delta\omega}{\omega_1}\right)} - \frac{1}{1 - j2Q_2\left(\frac{\Delta\omega}{\omega_1}\right)} \tag{5}$$

(5) can then be re-written as

$$M_r(s) = \frac{1 - j2Q_1\left(\frac{\Delta\omega}{\omega_1}\right)}{1 + 4Q_1^2\left(\frac{\Delta\omega^2}{\omega_1^2}\right)} - \frac{1 + j2Q_2\left(\frac{\Delta\omega}{\omega_2}\right)}{1 + 4Q_1^2\left(\frac{\Delta\omega^2}{\omega_2^2}\right)} \tag{6}$$

.

Assuming the bandwidth of each resonator is equal i.e.

$$\left(\frac{\omega_1}{Q_1}\right) = \left(\frac{\omega_2}{Q_2}\right) = \omega_{RB}$$

$$\Longrightarrow \quad M_r(s) = \frac{-4j\frac{\Delta\omega}{\omega_{RB}}}{1+4\left(\frac{\Delta\omega^2}{\omega_{RB}^2}\right)} \tag{7}$$

So

$$|M_r(s)| = \frac{4\frac{\Delta\omega}{\omega_{RB}}}{1+4\left(\frac{\Delta\omega^2}{\omega_{RB}^2}\right)} \tag{8}$$

$$\Longrightarrow \quad \frac{1}{M} = \frac{1}{4}\left(\frac{\omega_{RB}}{\Delta\omega}\right) + \left(\frac{\Delta\omega}{\omega_{RB}}\right) \tag{9}$$

.

Solving the above quadratic equation for

$\left(\frac{\Delta\omega}{\omega_{RB}}\right)$

$$\frac{\Delta\omega}{\omega_{RB}} = \frac{\frac{1}{M_r} + \sqrt{\frac{1}{M_r^2} - 1}}{2} \tag{10}$$

When ripple magnitude M_r is in dB, (10) can be expressed as

$$\Delta\omega = \frac{\omega_{RB}}{2}\left(10^{M_r/20} + \sqrt{10^{M_r/10} - 1}\right) \tag{11}$$

The 3dB bandwidth of 4th-order BPF can be written as

$$\omega_{3dB} = 2\Delta\omega + 2\left(\frac{\omega_{RB}}{2}\sqrt{\sqrt{2}-1}\right)$$

$$= 2\frac{\omega_{RB}}{2}\left(10^{M_r/20} + \sqrt{10^{M_r/10}-1}\right) + 2\left(\frac{\omega_{RB}}{2}\sqrt{\sqrt{2}-1}\right) \quad (12)$$

From (11) and (12), the bandwidths ω_{01}/Q_1 and ω_{02}/Q_2 , resonance frequencies $\omega_{o1}$and ω_{o2}, and the spacing from center frequency can expressed in term of the desired 3-dB bandwidth (ω_{3dB}), and passband ripple magnitude (M_r in dB-scale) as

$$\frac{\omega_{o1}}{Q_1} = \frac{\omega_{o2}}{Q_2} \cong \frac{\omega_{3dB}}{10^{M_r/20} + \sqrt{10^{M_r/10}-1} + \sqrt{\sqrt{2}-1}} \quad (13)$$

$$\Delta\omega \cong \frac{1}{2}\left(\frac{\omega_{o1}}{Q_1}\right)\cdot\left(10^{M_r/20} + \sqrt{10^{M_r/10}-1}\right) \quad (14)$$

$\rightarrow \omega_{o1} = \omega_c - \Delta\omega$ & $\omega_{o2} = \omega_c + \Delta\omega$.

In Figure 2-1, R_P represents a finite frequency-dependent LC- tank loss and $-R_N$ is a negative resistance for Q tuning. As in general filter synthesis, the resonance frequency and Q of each LC-tank needs to be set by the design specification of the passband response. Assuming a standard 2nd-order bandpass response with same BW ($\omega_{o1}/Q_1 = \omega_{o2}/Q_2$ in Figure 2-1) in each LC-tank, once passband center frequency (ω_c), 3-dB bandwidth (ω_{3dB}), and passband ripple magnitude (M_r in dB-scale) are specified, the resonance frequency and Q of the individual resonators can be set by (13) and (14).

For instance, for f_C =6 GHz, f_{3dB} = 300 MHz (5%), and M_r = 0.5 dB, the required frequency offset from f_C is $\Delta f \approx 210$ MHz, resulting in the LC-tank design parameters given as $f_{o1} \approx$ 5.79 GHz, $f_{o2} \approx$ 6.21 GHz, $Q_1 \approx 57$, and $Q_2 \approx 61$ by (3) and (4), which are well matched with circuit simulation. Figure 2-2(a) is the plot of frequency spacing between the two resonators and BW of each resonator when the total BPF filter bandwidth ω_{3dB} = 300 MHz is set in (3). For a given resonator bandwidth e.g. 200 MHz, the maximum achievable 4th-order bandwidth

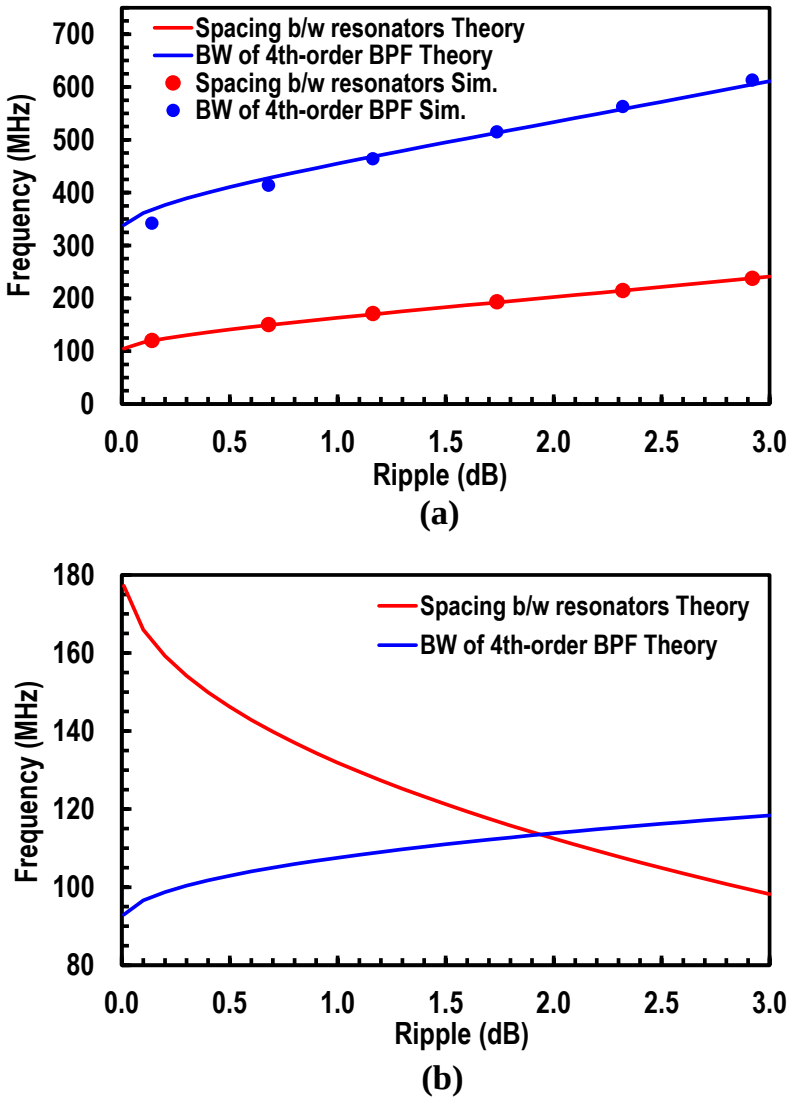

Figure 2-2: (a) Plot of spacing between resonators and total BPF bandwidth versus in-band ripple magnitude for a resonator bandwidth of 200 MHz and (b) Plot of frequency spacing between resonators and bandwidth of each resonator versus in-band ripple magnitude for a total bandwidth of 300 MHz.

and the frequency spacing between the two resonators are plotted in Figure 2-2(b) against passband ripple. For a 3-dB ripple, the maximum 4th-order bandwidth is 613 MHz, which is 3.1 times the bandwidth of the individual resonators. By lowering the Q (increasing the BW) of each resonator to around 4~5, a very large bandwidth can be achieved.

2.2.2 Noise Analysis

A system-level noise analysis is performed for the 4th-order BPF. The block diagram of a synthetic 4th-order filter consists of two 2nd-order filters Ⓐ and Ⓑ is shown in Figure 2-3. The noises of the LC tank, negative resistance and Q-tuning element are assumed to be dominant. The 2nd-order BPF has noise sources from $R_{C1,2}$, used for Q control, tank losses $R_{P1,2}$ and the loss compensation negative resistance $R_{N1,2} = -1/G_{m1,2}$ where $G_{m1,2}$ is cross-coupled transconductance in typical Q-enhanced LC filters. As can be seen in Section III-C, the noise contribution from the unity gain buffers in Figure 2-4 will be negligible since their output resistance will be far smaller than $R_{C1,2}$ in actual transistor level circuit implementation. The noise currents from $R_{C1,2}$, $R_{P1,2}$ and $R_{N1,2}$ are sampled by the total tank load $Z_{Tank1,2}$ and the equivalent total noise power of each 2nd – order BFP is given by

$$\overline{V_{n,T1,2}^2} = 4kT\left(\frac{1}{R_{C1,2}} + \frac{1}{R_{P1,2}} + \gamma_{Eq}G_{m1,2}\right)\left|Z_{Tank1,2}\right|^2 \tag{15}$$

where

$$Z_{Tank1,2} = R_{C1,2} \parallel R_{N1,2} \parallel \left(R_{P1,2}\frac{\frac{\omega_{01,2}}{Q_{1,2}}s}{s^2 + \frac{\omega_{01,2}}{Q_{1,2}}s + \omega_{01,2}^2}\right). \tag{16}$$

and γ_{Eq} is the constant factor associated with the negative transconductance cell noise sources. In the vicinity of resonance frequency, the tank impedance can be approximated to

$$Z_{Tank1,2}\,@\omega = \omega_{01,2} \pm \Delta\omega_{1,2} \cong \frac{R_{C1,2}}{1 + \square 2Q_{1,2}\frac{R_{C1,2}}{R_{P1,2}}\frac{\Delta\omega_{1,2}}{\omega_{01,2}}} \tag{17}$$

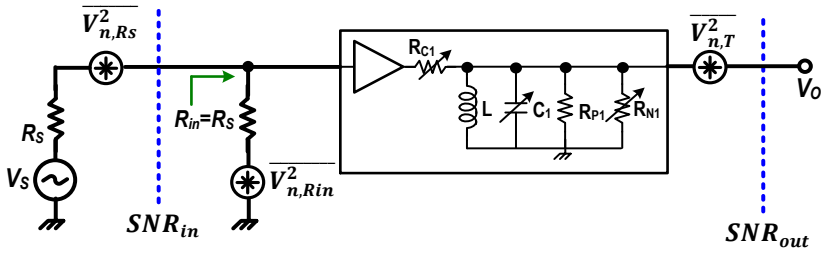

Figure 2-3: Noise source in a 2nd-order BPF.

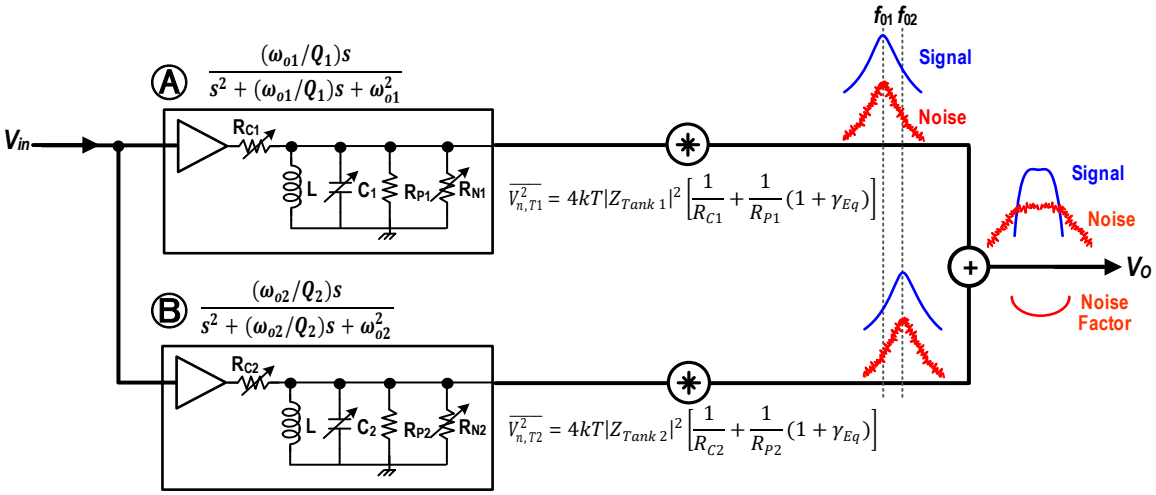

Figure 2-4: Noise shaping of the 4th-order BPF.

where $\Delta\omega_{1,2}$ expresses a small offset frequency around $\omega_{01,2}$ satisfying $\Delta\omega_{1,2} << \{\omega_{o1}, \omega_{o2}\}$. For simplification, let's assume that $R_{C1} = R_{C2}$, $R_{P1} = R_{P2}$, and $G_{m1} = G_{m2}$. If the tank loss is completely compensated by the negative resistance, e.g. $G_{m1,2} = -1/R_{P1,2}$, then the effective total noise power at ω_{01} will be given as

$$\overline{V_{n,T}^2}\big|_{\omega=\omega_{01}} = \overline{V_{n,T1}^2}\big|_{\omega=\omega_{01}} + \overline{V_{n,T2}^2}\big|_{\omega=\omega_{01}=\omega_{02}-2\Delta\omega} = 4kTR_{C1}\left\{1+\frac{R_{C1}}{R_{P1}}(1+\gamma_{Eq})\right\}$$

$$\times\left[1+\left\{1+\left(2Q_2\frac{R_{C2}}{R_{P2}}\frac{2\Delta\omega}{\omega_{02}}\right)^2\right\}^{-1}\right] = \underbrace{4kTR_{C1}\left\{1+\frac{R_{C1}}{R_{P1}}(1+\gamma_{Eq})\right\}}_{noise\ power\ of\ standalone\ 2nd-order\ BPF}$$

$$\times\underbrace{\left[1+\left\{1+\left(2\frac{R_{C2}}{R_{P2}}\mathrm{K}\right)^2\right\}^{-1}\right]}_{added\ nosie\ power\ factor\ ①}. \quad (18)$$

In (18), $2\Delta\omega/\omega_{02} = \mathrm{K}/Q_2$ is applied where $\mathrm{K} = 10^{M_r/20} + \sqrt{10^{M_r/10}-1}$ in (14) (see Fig. 2-3). Likewise, the effective total noise power at ω_{02} is found to be as

$$\overline{V_{n,T}^2}\big|_{\omega=\omega_{02}} = \overline{V_{n,T1}^2}\big|_{\omega=\omega_{02}=\omega_{01}+2\Delta\omega} + \overline{V_{n,T2}^2}\big|_{\omega=\omega_{02}}$$

$$= \underbrace{4kTR_{C2}\left\{1+\frac{R_{C2}}{R_{P2}}(1+\gamma_{Eq})\right\}}_{noise\ power\ of\ standalone\ 2nd-order\ BPF} \times\underbrace{\left[1+\left\{1+\left(2\frac{R_{C1}}{R_{P1}}\mathrm{K}\right)^2\right\}^{-1}\right]}_{added\ nosie\ power\ factor\ ②}. \quad (19)$$

Similarly, the noise power will be given as (20) at the center of the passband (ω_c).

$$\overline{V_{n,T}^2}\big|_{\omega=\omega_c} = \overline{V_{n,T1}^2}\big|_{\omega=\omega_{01}+\Delta\omega} + \overline{V_{n,T2}^2}\big|_{\omega=\omega_{01}=\omega_{02}-\Delta\omega}$$

$$= \underbrace{4kTR_{C1}\left\{1+\frac{R_{C1}}{R_{P1}}(1+\gamma_{Eq})\right\}}_{noise\ power\ of\ standalone\ 2nd-order\ BPF} \times\underbrace{\left[\left\{1+\left(\frac{R_{C1}}{R_{P1}}\mathrm{K}\right)^2\right\}^{-1}+\left\{1+\left(\frac{R_{C2}}{R_{P2}}\mathrm{K}\right)^2\right\}^{-1}\right]}_{added\ nosie\ power\ factor\ ③}. \quad (20)$$

From (18) – (20), the added noise power factors, the noise penalty paid for the 4th – order BPF

synthesis, is the function of $R_{C1,2}/R_{P1,2}$ and K. The parameter K ranges from 1.4 ~ 1.6 when 0.5 to 1 dB of passband ripple is allowed. In typical moderate-to-high Q control greater than the intrinsic LC tank Q, $R_{C1,2}$ will be greater than the intrinsic LC tank resistance $R_{P1,2}$. This makes the added noise power factors ① and ② in (18) and (19) less than 1.1 if K=1.5 is assumed, namely less than 10% noise power increase at the edges of the passband compared with the standalone 2nd-order BPF. The added noise power factor ③ in (20) will be less than 1 when $K \cdot R_{C1,2} > R_{P1,2}$, resulting in slight better noise performance than standalone 2nd-order BPF at ω_c. The reason for this better noise performance is obvious since the two added noises from individual filters are perfectly uncorrelated, whereas signals are correlated at ω_c. Note that as increasing the ratio of $R_{C1,2}/R_{P1,2}$ to obtain higher filter Q, the net noise power from the individual 2nd-order BPFs also increases, degrading overall noise performance and exhibiting typical noise-selectivity tradeoff in the Q-enhanced LC filters.

In a low Q control smaller than the intrinsic LC tank Q, $R_{C1,2}$ will be smaller than $R_{P1,2}$ and the added noise power factors ①, ② and ③ in (18)–(20) will increase incrementally. Apparently, in extremely low Q case where $K \cdot R_{C1,2} \ll R_{P1,2}$ the two 2nd – order BPFs could degenerate to an all-pass filter at the frequency band of interest. Then, the two BPF noise powers, $\overline{V_{n,T1}^2}$ and $\overline{V_{n,T2}^2}$, will be added together with negligible noise shaping effect by the resonators. This is well expected in (18)–(19) where if $K \cdot R_{C1,2} \ll R_{P1,2}$ the added noise power factors ①, ② and ③ approach to 2, manifesting non-coherent addition of the two BPF noises at the synthetic 4th-order BPF output. It should be noticed that as decreasing $R_{C1,2}$ for lowering Q, the net noise power from individual 2nd-order BPFs also becomes smaller. Thus, even if the added noise power factors increase the overall noise power will decrease, resulting in better noise performance compared with the high Q case.

Intuitively each resonator attenuates noise power with a 2nd-order bandpass response in Figure 2-4. Since the resonance frequencies of resonators are staggered, the attenuated noise from filter Ⓐ is either added directly to filter Ⓑ at ω_{02} or further attenuated by the bandpass response of filter Ⓑ before being added. Thanks to this attenuated bandpass noise shaping, the degradation of noise performance by the uncorrelated noise addition in the 4th-order bandpass filter is negligible. The net effect of the added noise at the edges of 4th-order BPF passband on the overall system noise

figure will be particularly trivial when the BPF is preceded by a high gain amplifier stage such as LNA or transconductor in typical RF front-end applications.

From equation (18) - (20), tank load, tunable resistance, losses and loss compensation are the main noise contributing sources. Therefore, the noise factor of 4th-order BPF in the passband will be same as that of 2nd-order BPF as the noise is shaped by the individual BPFs Ⓐ and Ⓑ, shown in Figure 2-4. At the first center frequency f_{01}, the dominant noise is that of the filter Ⓐ shaped by the 2nd-order BPF response. This results in same noise factor at the output after subtraction. Similarly, at the second center frequency f_{02}, the dominant noise is that of the filter Ⓑ and appears at the output after subtraction.

2.3 MOS Varactor Analysis

2.3.1 Varactor Device Capacitance

Figure 2-5 shows the device cross section of a MOS varactor structure in a p-substrate n-well where source and drain are tied together to form one of the two terminals. The other terminal is the gate of the device. The voltage across the two terminals is varied from negative to positive to form a variable capacitance. For a positive voltage V_{GS}, an accumulation of electrons are formed beneath the gate oxide resulting in maximum varactor capacitance which in this case is the oxide capacitance, i.e. $C_{max} = C_{0x}$ as shown in Figure 2-5. When voltage V_{GS} across varactor starts decreasing the capacitance C_{ox} decreases and a positive space charge/depletion region starts forming when V_{GS} becomes negative. The oxide capacitance C_{ox} and depletion capacitance C_D are in series now as shown in Figure 2-6. The minimum capacitance $C_{min} = C_{ox} \parallel C_D$ is achieved when the V_{GS} level is within the recommended device operating range which in this is from 1 V to -0.5 V. I. The capacitance in depletion mode is given by

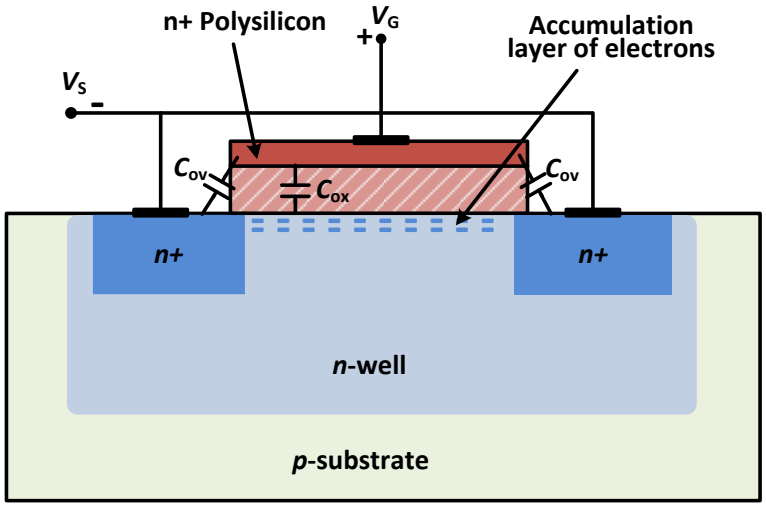

MOS Cap in Accumulation mode

Figure 2-5: MOS Capacitance in accumulation mode with a positive voltage across the V_{GS} forming the maximum capacitance C_{max} consisting of C_{ox}.

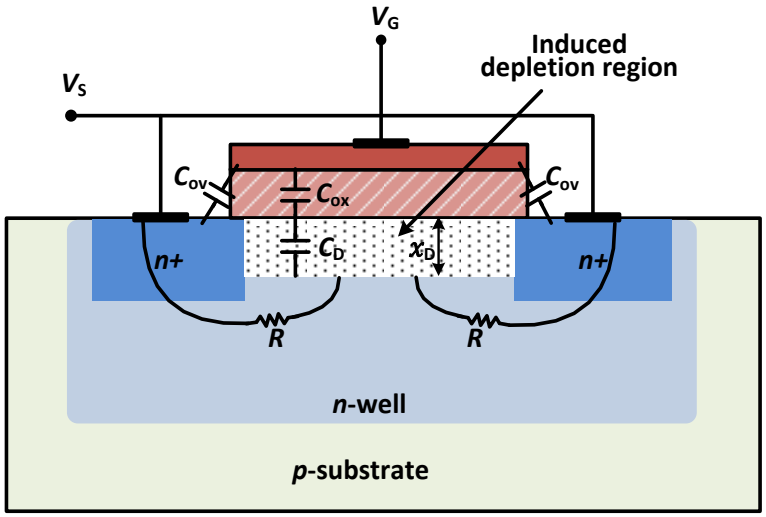

Figure 2-6: MOS Capacitance in an induced depletion mode with a negative voltage across the V_{GS} forming the minimum capacitance C_{min} consisting of C_{ox} in series with C_D.

$$C_{var}(dep) = \frac{C_{ox}C_D}{C_{ox}+C_D} = \frac{C_{ox}}{1+\frac{C_{ox}}{C_D}} = \frac{\varepsilon_{ox}\varepsilon_0}{t_{ox}+\left(\frac{\varepsilon_{ox}}{\varepsilon_s}\right)x_D} = \frac{C_{ox}}{1+\left(\frac{\varepsilon_{ox}}{\varepsilon_s}\right)\frac{x_D}{t_{ox}}} \quad (21)$$

where x_D is the depletion width. As x_D increases, C_{var} decreases. For $x_{D,max}$, $C_{var} = C_{min}$. The tuning ratio can be expressed as C_{max}/C_{min}. For shorter L length of the nMOS, which is desired for high Q (discussed in next section), gate to source/drain overlap and fringe capacitance C_{ov}, shown in Figure 2-6., becomes significant. This reduces the tuning/ratio range to

$$Tuning\ Ratio = \frac{C_{max}+2C_{ov}}{C_{min}+2C_{ov}}\,. \quad (22)$$

2.3.2 Varactor Device Parasitic

The MOS varactor lumped model is shown in Figure 2-7 with tuning capacitance and parasitic resistance R_{var} in series along with distributed RC model. The Q of the varactor can be written as

$$Q = \frac{1}{\omega R_{var} C_{var}}\,. \quad (23)$$

It is evident from the model in Figure 2-7 that the varactor parasitic resistance is proportional to the length L of the nMOS, the shorter the length the higher the Q. In accumulation mode with capacitance C_{max}, the electron accumulated channel resistance along with resistivity of n-well and n+ region determines the Q. In this region the resistance R_{var} gives a certain Q. The n+ regions are shorted through an electron layer and the effective resistance can be approximated as channel resistance. Going towards depletion mode, towards C_{min} , the capacitance decreases and resistance increases. The resistance is now the n-well resistance. We expect the Q to be somewhat constant. However, the Q does not remain constant, and increases when we move towards C_{min} , implying that the rate of decrease of C_{var} is more than the rate of increase of R_{var}

$$\left|\frac{d\,(C_{var})}{dV_{GS}}\right| > \left|\frac{d\,(R_{var})}{dV_{GS}}\right| \tag{24}$$

2.3.3 IBM8HP SiGe BiCMOS Varactor

The technology used to implement this work is IBM8HP SiGe BiCMOS which provides a varactor device (ncap) with a capacitance range of 4.8 times but with poor Q. The varactor range has relation to the Q, a higher range results in a lower Q resulting from the device physics and layout. With a decent Q of more than 15, the resulting varactor range is around 4.3 times which after parasitic addition results in around 4 times. It is important to mention that the parasitic capacitance reduces the varactor tuning range for smaller varactors. Thus the varactor design involves consideration of varactor size and inductor for the required frequency tuning range. A 4 times varactor capacitance variation gives twice of the frequency tuning range as $= 1/\sqrt{LC}$.

In this work, the varactor size is $1.1 - 4.2\ pF$ which, in parallel with $L = 325$ pH, covers the frequency range from 4-8 GHz including all parasitic effects. For the BiCMOS 8HP nMOS varactor, both capacitance and quality factor Q are plotted against tuning voltage V_{GS} in Figure 2-8. The simulated minimum Q of the varactor is around 18 at 5 GHz.

2.4 Linearity Analysis

Figure 2-9 shows the nonlinear response of the 4th-order filter when excited by two tones intuitively. The major sources of non-linearity are the varactor and the active loss compensation negative resistance. Two cases are discussed for the two-tone location within the 4th-order filter band. Case ① is the worst case scenario when the two tones are at the edge of 4th-order passband or at the center of 2nd-order filter Ⓐ. For the nonlinear response of the individual 2nd-order filters, shown on top of each other, the filter Ⓐ will give standard 2nd -order filter response and its nonlinear waveform $\Psi_{Ⓐ}$ is expressed as (21). In (21), the magnitude $(1/\alpha)$ of the 3rd-order intermodulation distortion (IMD3) tones ($\Psi_{Ⓐ,IMD3}$) are normalized by the magnitude of the fundamental tones ($\Psi_{Ⓐ,fund}$). The 3rd – order input intercept point (IIP3) of filter Ⓐ is found to

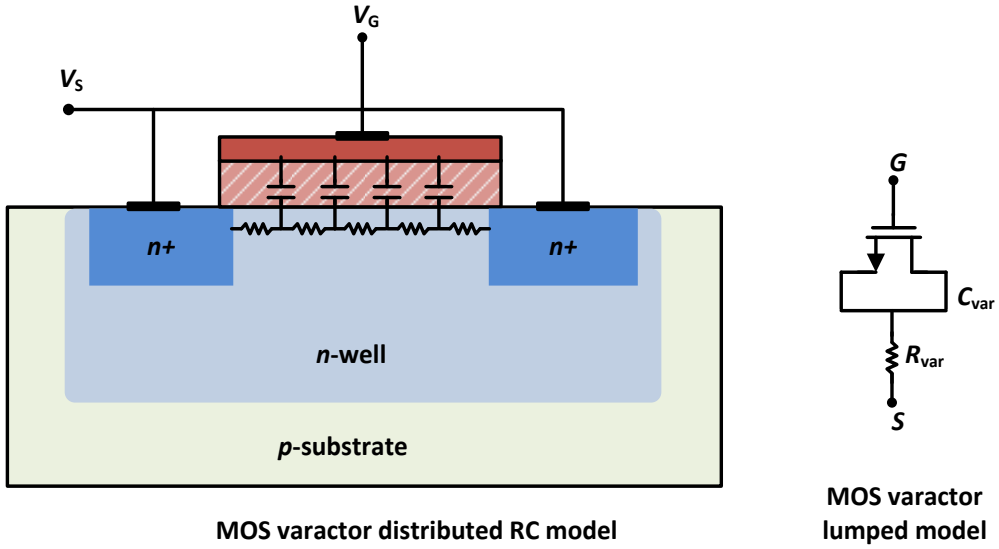

Figure 2-7: MOS Capacitance in accumulation mode with a positive voltage across the V_{GS} forming the maximum capacitance C_{max} consisting of C_{ox}.

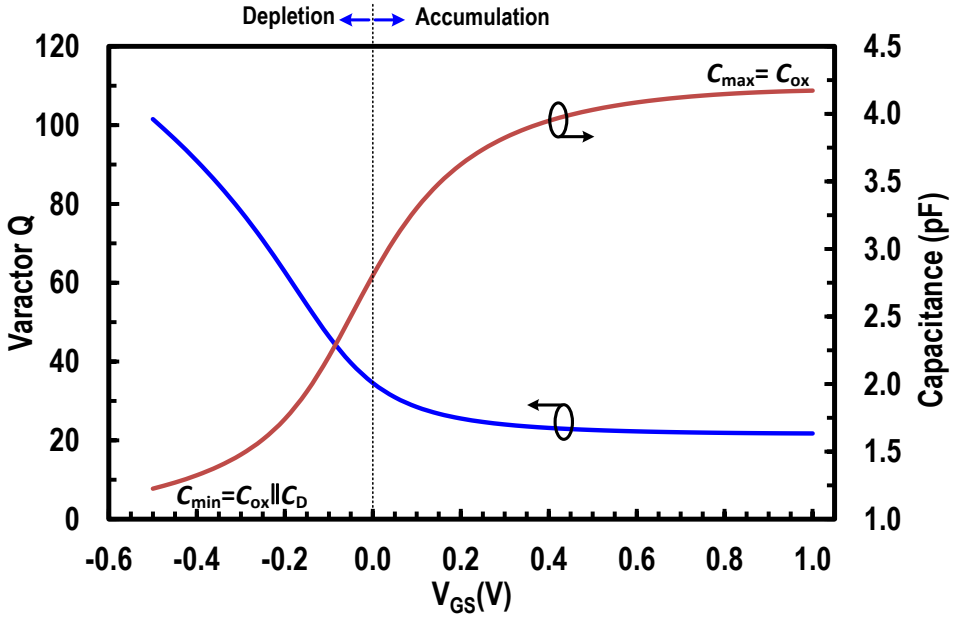

Figure 2-8: BiCMOS 8HP "ncap" varactor simulation of capacitance tuning and quality factor Q.

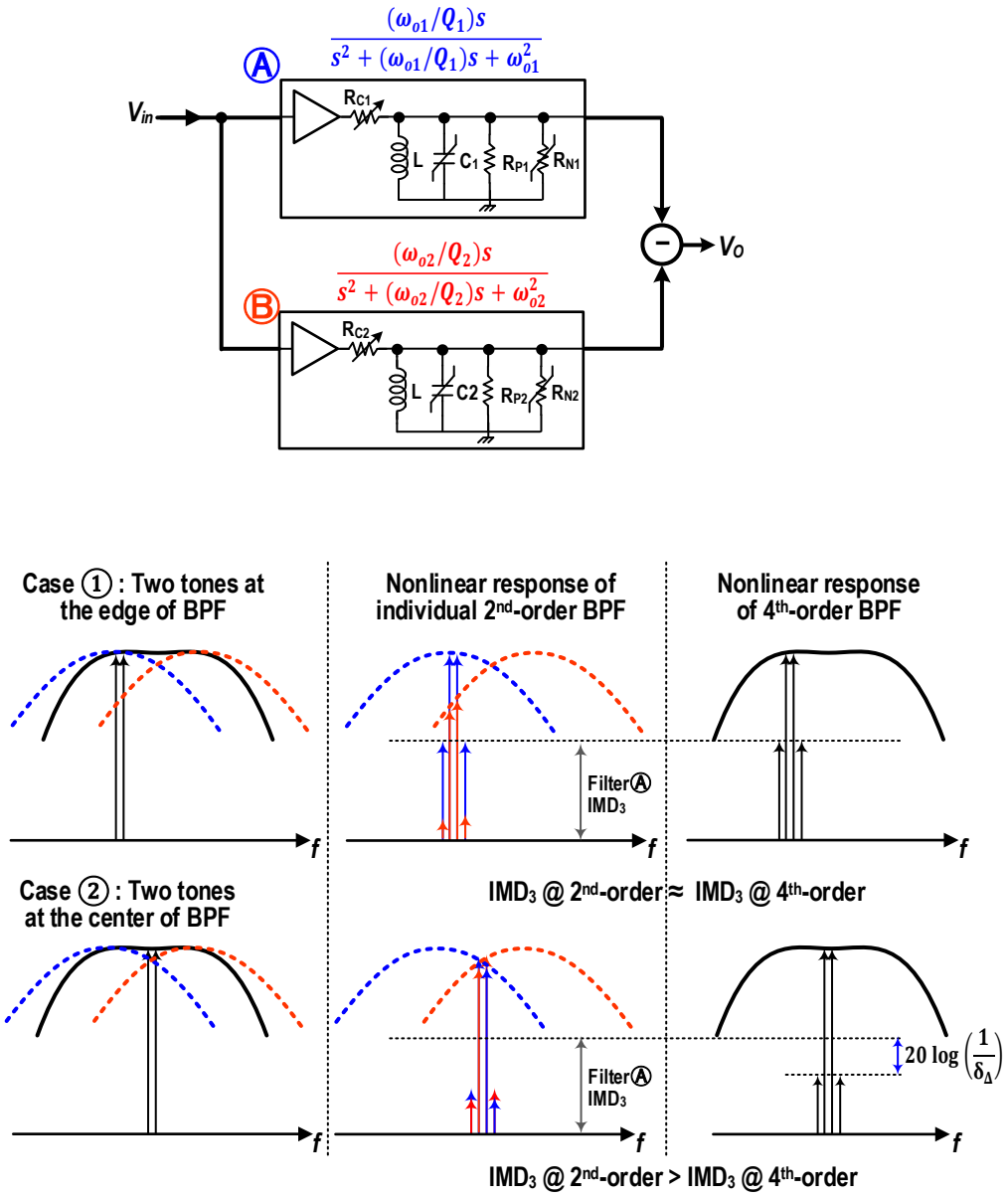

Figure 2-9 Conceptual description of nonlinear response of the synthetic 4th–order filter comprising two 2nd-order filters Ⓐ and Ⓑ with two-tone analysis for two cases : ① at the edge of 4th-order response and ② at the center of 4th-order response.

be 10log($\alpha \cdot P_{in}$) [dB] where P_{in} is the input power in linear scale. Assuming the two fundamental tones (ω_1 and ω_2) and IMD3 tones ($2\omega_1 - \omega_2$ and $2\omega_2 - \omega_1$) are close enough not to experience any meaningful phase delay difference amongst them, the two-tone response of filter Ⓑ can be given as (22).

$$\Psi_{Ⓐ} = \underbrace{e^{j\omega_1 t} + e^{j\omega_2 t}}_{\Psi_{Ⓐ,fund}} + \frac{1}{\alpha}\underbrace{\left\{e^{j(2\omega_1-\omega_2)t} + e^{j(2\omega_2-\omega_1)t}\right\}}_{\Psi_{Ⓐ,IMD3}}. \tag{25}$$

$$\Psi_{Ⓑ} = \begin{pmatrix} \delta \cdot \Psi_{Ⓐ,fund} \\ + \delta^3 \cdot \frac{1}{\alpha}\Psi_{Ⓐ,IMD3} \end{pmatrix} e^{-j\varphi}$$

$$where, \delta = \frac{|Z_{Tank2}|}{R_{C2}} \; and \; \varphi = tan^{-1}(Z_{Tank2}). \tag{26}$$

In (26), the output of filter Ⓑ is modulated by the normalized tank impedance ($\delta^{-j\varphi}$). δ and φ are dependent on the frequency offset from the resonance frequency of each filter. Note that the IMD3 tones are attenuated by a factor of δ^3 compared with the fundamental tone attenuation factor of δ. The composite two-tone response (Ψ_T) at the output of the 4th-order filter will be

$$\Psi_T = \Psi_{Ⓐ} + \Psi_{Ⓑ} = \left(1 + \delta \cdot e^{-j\varphi}\right)\Psi_{Ⓐ,fund} + \left(1 + \delta^3 \cdot e^{-j\varphi}\right)\frac{1}{\alpha}\Psi_{Ⓐ,IMD3}. \tag{27}$$

From (17), the attenuation factor δ at $2\Delta\omega$ offset from the center frequency of filter Ⓑ (see Figure 2-1) can be found as

$$\delta_{2\Delta} = \frac{1}{\sqrt{1 + \left(2Q_2 \frac{R_{C2}}{R_{P2}} \frac{2\Delta\omega}{\omega_{02}}\right)^2}} = \frac{1}{\sqrt{1 + \left(2\frac{R_{C2}}{R_{P2}}\mathrm{K}\right)^2}}. \tag{28}$$

Therefore, IIP_3 of the 4th-order filter at the edge of passband, $IIP_3|_{T,edge}$, is

$$IIP_3|_{T,edge} = 10log\left(\alpha \cdot P_{in}\sqrt{\frac{(1+\delta_{2\Delta}cos\varphi)^2+(\delta_{2\Delta}sin\varphi)^2}{\left(1+{\delta_{2\Delta}}^3cos\varphi\right)^2+\left({\delta_{2\Delta}}^3sin\varphi\right)^2}}\right)$$

$$= IIP_3|_{filter\text{Ⓐ}} + 10log\left(\sqrt{\frac{(1+\delta_{2\Delta}cos\varphi)^2+(\delta_{2\Delta}sin\varphi)^2}{\left(1+{\delta_{2\Delta}}^3cos\varphi\right)^2+\left({\delta_{2\Delta}}^3sin\varphi\right)^2}}\right). \quad (29)$$

In typical Q control where $\mathrm{K}\cdot R_{C2} > R_{P2}$, δ could be much smaller than 1. Therefore, the resultant IIP_3 is essentially the same as that of the 2nd-order filter or slight better. The same is valid for the higher frequency edge of the 4th-order filter.

The best case, ② in Figure 2-9, is when the two tones are at the center of the 4th-order filter passband. At the center of passband, the two filters outputs are added in phase and the overall wave function of (27) will be modified to

$$\Psi_{\mathrm{T}} = \Psi_{\text{Ⓐ}} + \Psi_{\text{Ⓑ}} = 2\delta\left(\Psi_{\text{Ⓐ},fund} + \frac{\delta^2}{\alpha}\Psi_{\text{Ⓐ},IMD3}\right)\mathrm{e}^{-j\varphi}. \quad (30)$$

The attenuation factor δ at $\Delta\omega$ offset from the center frequency of each filter (see Figure 2-1) is

$$\delta_\Delta = \frac{1}{\sqrt{1+\left(2Q_{1,2}\frac{R_{C1,2}}{R_{P1,2}}\frac{\Delta\omega}{\omega_{01,2}}\right)^2}} = \frac{1}{\sqrt{1+\left(\frac{R_{C1,2}}{R_{P1,2}}\mathrm{K}\right)^2}}. \quad (31)$$

Therefore, IIP_3 at the center of passband, $IIP_3|_{T,center}$, will be

$$IIP_3|_{T,center} = IIP_3|_{filter\text{Ⓐ}} + 20log\left(\frac{1}{\delta_\Delta}\right). \quad (32)$$

The net IIP_3 improvement is $20log(1/\delta_\Delta)$ at the mid passband.

Figure 2-10 illustrates a simplified simulation setup in Advanced Design System (ADS) to verify the linearity improvement in the 4th-order BPF and simulation results for the case ① and

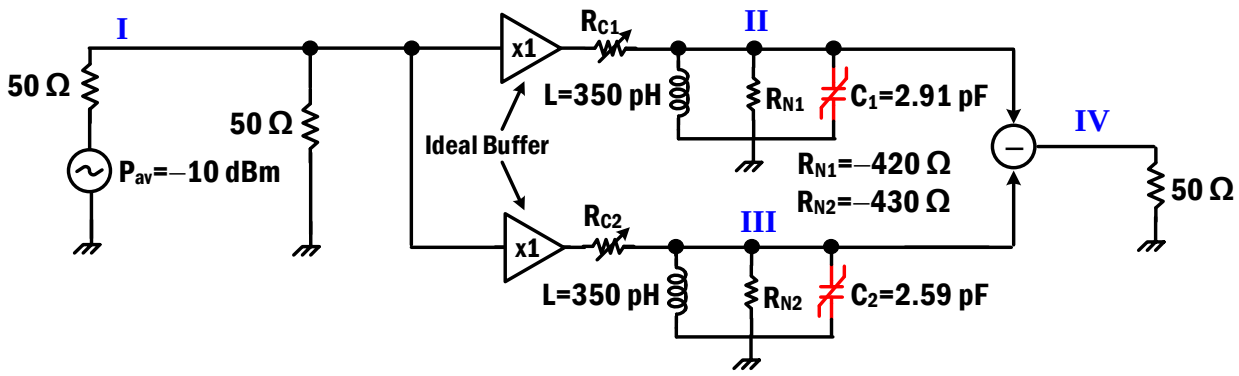

Figure 2-10 Simulation setup for the nonlinear response of the synthetic 4th–order filter comprising two 2nd-order filters Ⓐ and Ⓑ.

② in Figure 2-9. Figure 2-10, the ideal voltage buffer is a voltage controlled voltage source (VCVS) component and the varactor from GlobalFoundries (GF) 0.13 μm SiGe BiCMOS process (GF8HP) library model (model name: ncap) is used. The varactance ranges 1.1-to-4.2 pF and is set to 2.91 pF at filter Ⓐ and 2.59 pF at filter Ⓑ to resonate the inductor L=350 pH at around 5 GHz (f_{o1}) and 5.28 GHz (f_{o2}), respectively, resulting in f_c=5.14 GHz. In this case, the varactor Q is 38.3 and 37, resulting in the parasitic LC tank resistance of 420 Ω and 430 Ω in the filters Ⓐ and Ⓑ, respectively. These resistances are compensated respectively by the negative resistances of R_{N1} and R_{N2}. Then, R_{C1} and R_{C2} are set to 232 Ω and 262 Ω, respectively, to define the filter Q to around 21.24 and 22.55 in the filters Ⓐ and Ⓑ, respectively, a 5-6% error. With matched impedance, two tones with same −10 dBm input power are applied to characterize the filter nonlinearity, and the results are shown in Figure 2-11.

For case ①, with two-tone input of 5 GHz ±25 MHz, the IMD_3 tones at the output of filter Ⓐ are about -36 dBm [see node II output in Figure 2-11]. Whereas the IMD_3 tone powers are significantly decreased to around -70 dBm at the output of filter Ⓑ due to gain decrease [see node III output in Figure 2-11]. Consequently, the composite IMD_3 at the output of 4th-order response [node IV output in Figure 2-11] is essentially same as that of filter Ⓐ. However, at the center of

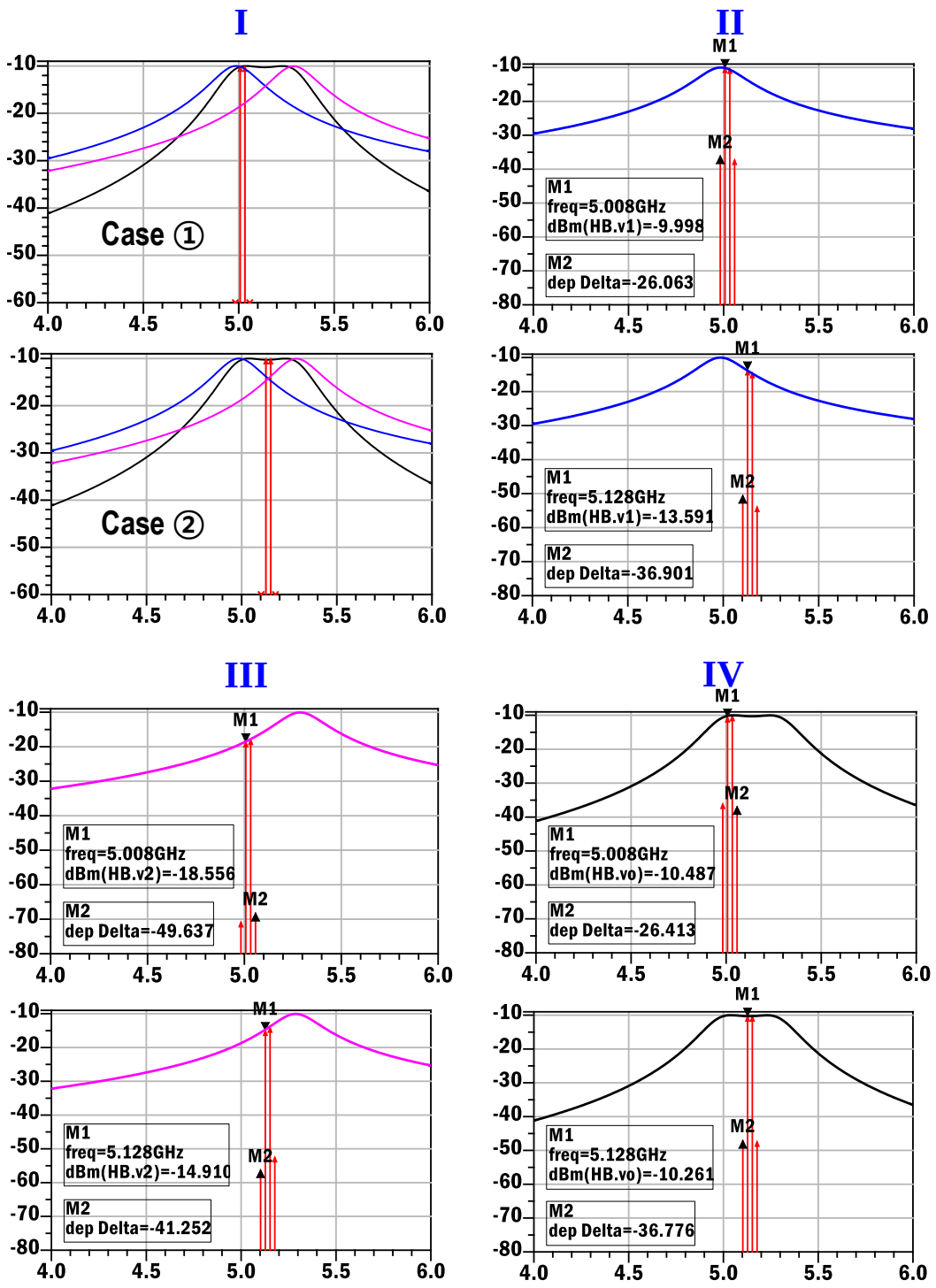

Figure 2-11 Simulated nonlinear response of the synthetic 4th–order filter comprising two 2nd-order filters Ⓐ and Ⓑ with two-tone analysis for two cases : ① at the edge of 4th-order response and ② at the center of 4th-order response.

the passband (case ②) each individual filter's IMD_3 tones decrease by the factor of three in dB-scale compared to the fundamental tones, decreasing to below the -36.9 dBm level. After combining the nonlinearities, the composite IMD_3 at the synthetic filter output node IV grows to around -47 dBm. This is ~11 dB smaller IMD_3 tone power, resulting in 5.5 dB better IIP_3 at the center of the 4^{th}-order BPF passband compared to the individual 2^{nd}-order filter's IIP_3.

The simulation verifies the linearity advantage of the 4^{th}-order BPF using subtraction of two 2^{nd}-order BPFs. When the ripple magnitude is kept below ~1.5 dB ($K < 1.7$), the theoretical IIP_3 improvement from (32) is around 3 dB. The discrepancy is because theory assumes identical quality factor and same nonlinearity from individual 2^{nd}-order filters. However, in actual simulation, the two filters experience slight different Q and nonlinearity because the varactors are biased slightly different bias points.

From the noise and linearity analysis it is evident that using the subtraction of two 2^{nd}-order filters, to achieve 4^{th}-order filtering, results in same noise figure as that of the individual 2^{nd}-order filters. Meanwhile, the nonlinear behavior of the 4^{th}-order is the same as 2^{nd}-order BPF at worst, and improves in the mid region of 4^{th}-order filter band. Therefore, the dynamic range of the 2^{nd}-order filter is preserved when using synthetic approach to implement a 4^{th}-order BPF. The detailed circuit level noise analysis is presented in chapter3 and for the linearity circuit level simulation results are included in Appendix A.

2.5 Summary

In this chapter, the 4^{th}-order BPF analysis is done in terms of signal synthesis and filter design equations. This is followed by the noise and linearity performance analysis. The signal and performance analysis concludes that the parallel synthesis 4^{th}-order filter has advantages over traditional cascading resonators in terms of functionality (achieving tunable wideband filtering) as well as dynamic range performance.

Chapter Three: **Tunable 4th-Order BPF Implementation**

3.1 Introduction

This chapter covers the 4th-order BPF implementation in SiGe BiCMOS technology in detail including block diagram, circuit design and analysis, and detailed measurement results. Applications of the proposed wideband 3-dB bandwidth tunable filter include cellular communication, radar systems, navigation, etc. One such application is a Radar Receiver Protector (RRP) as discussed in chapter 1. By integrating such radar systems in silicon with tunable filters and Gallium Nitride (GaN) or Silicon Germanium (SiGe) based LNAs, the size, weight and power can be reduced substantially.

3.2 4th–order Q-Enhanced LC BPF Circuit Design

Figure 3-1 shows a block diagram of the proposed differential 4th-order filter, along with integrated varactor linearization control scheme. This filter is implemented in 0.13 μm SiGe BiCMOS technology. The variable transconductor G_m cells drive the LC filter sections in current

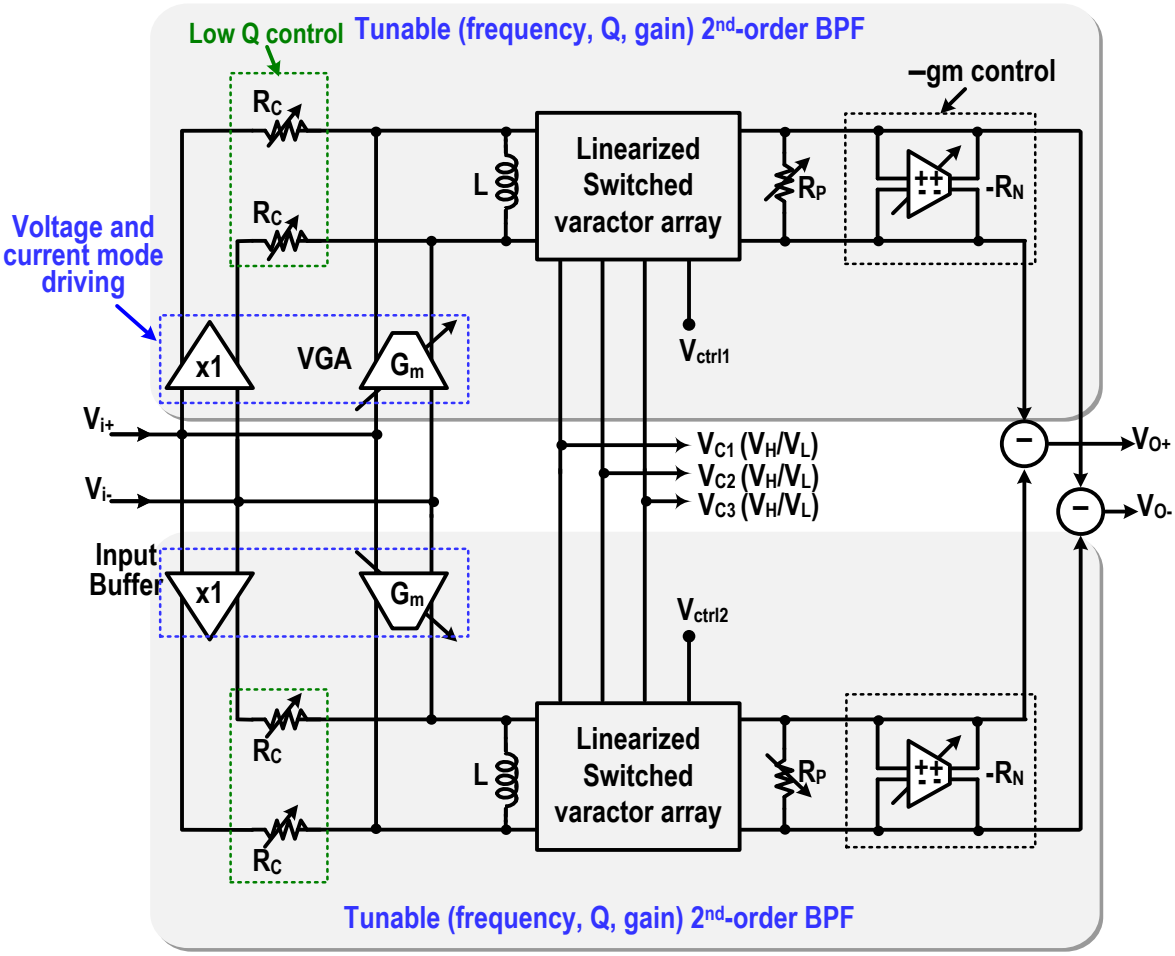

Figure 3-1: Differential synthetic 4th-order bandpass filter block diagram.

mode and provide gain control. The LC BPFs are also driven in voltage mode by the unity gain (x1) input buffers. This dual mode driving scheme allows for power-efficient gain control when the BPF Q varies widely and provides filter operation flexibility in the noise-linearity tradeoff space [35]. The LC-tank losses in each 2nd-order BPF are compensated by their respective negative gm cells ($-R_N$) which has a control to increase the Q of the tank. The outputs of the two tunable (frequency, Q, gain) 2nd-order BPFs are subtracted to realize 4th-order BPF shaping.

3.2.1 Frequency-Tuning and Varactor Linearization

The center frequency tuning of each 2nd-order BPF is done using a varactor as discussed in section 2.2. The varactor capacitance is a function of control voltage ΔV_{GS} across its terminals. The typical C-V relation of a widely tunable varactor is depicted in Figure 3-2. The varactor tuning capacitance range expressed as a ratio of maximum to minimum capacitance is around 4:1 in this case. For large frequency tuning range, e.g. octave, we need large varactor capacitance tuning ratio, e.g. four in this case meaning Cmax/Cmin~4. This large range makes the varactor very nonlinear in the middle region which is a disadvantage compared to Metal-Insulator-Metal (MIM) based switched fixed cap banks. However, the use the MIM cap banks seriously affect the frequency tuning and Q of the tank. First in order to switch to filter banks, the switches have to be very large so that the switch resistance does not affect the Q of the tank. In doing so, the off-state switch capacitance will add to varactor Cmax and Cmin thereby limiting the tuning range of frequency. Large switched capacitor banks also put a serious toll on the tank Q in terms of layout parasitics. Since the MIM caps occupies large area and thus connecting them together to form LC tank Q–sensitive nodes will add significant parasitics which will lower the Q and limit the frequency tuning. In the current implementation, due to the smaller size of varactors, the LC tank layout is done in an efficient manner and the Q degradation due to layout is found to be around 7% after post layout simulation. This helps with noise and linearity since less negative gm is needed to compensate for the Q of the LC-tank. Switched varactor control does not suffer from the limitation of switched fixed capacitor banks however the linearity needs to be improved.

The varactor capacitance is quasi-linear towards the minimum and maximum capacitance regions and strongly non-linear in the transition region. To minimize the nonlinearity, the single

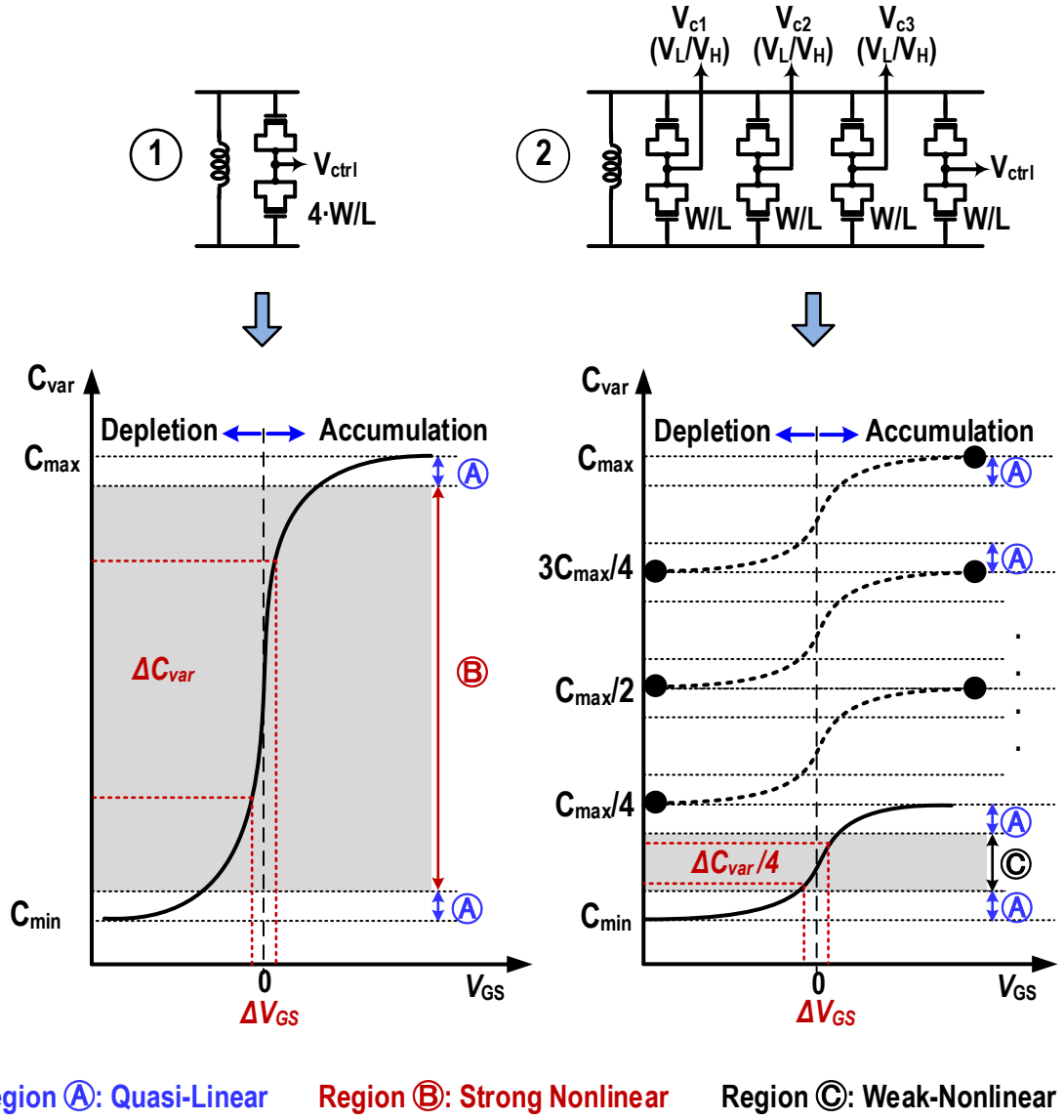

Figure 3-2: Varactor control schemes: ① typical single control varactor with large non-linear capacitance and ② four independent controls employing three switched and one continuous mode control to improve the linearity by reducing the non-linear capacitance.

large varactor is split into multiple equal-sized smaller varactors where N-1 of these are controlled discretely ON and OFF and the Nth varactor is varied continuously to cover the entire frequency range without any discontinuity. The switched varactor approach is going to be developed further in chapter 4. For the filter implementation in this chapter, a bank of four differential paired varactors $C_{v1} - C_{v4}$ together with inductor L form the tunable LC-Tanks. The two LC-tanks in Figure 3-1 are identical with common controls ($V_{C1} - V_{C3}$) for the three-varactors and one independent varactor control (V_{ctrl1}, and V_{ctrl2}) for each tank to tune to closely spaced frequencies. Total varactor capacitance varies from $1.1 - 4.2\ pF$ which, in parallel with $L = 325$ pH, covers the frequency range from 4-8 GHz including all parasitic effects. When using a single large varactor for frequency tuning, due to the nonlinear variable capacitance transition versus control voltage, nonlinearity from the varactor becomes significant as illustrated in Figure 3-2① in terms of P_{-1dB}.

The nonlinear capacitance in Region Ⓑ in Figure 3-2① can be expressed using power series as

$$C_{var}(V_{GS}) = C_0 + C_1 V_{GS} + C_2 V_{GS}^2 \tag{1}$$

where V_{GS} consists of the DC tuning point plus the AC output of the varactor, $V_{GS} = V_{GS,DC} + \Delta V_{GS}$. Capacitance C_0 is the fixed linear capacitance due to the DC tuning point. The nonlinear capacitance coefficients in (1) are

$$C_1 = \frac{dC_{var}}{dV_{GS,DC}}, \quad C_2 = \frac{1}{2}\frac{d^2 C_{var}}{dV_{GS,DC}^2} \tag{2}$$

The nonlinear current is then given by

$$\begin{aligned} i_{var}(V_{GS}) &= \frac{dQ_{var}}{dt} = C_{var}(V_{GS})\frac{dV_{GS}}{dt} \\ &= C_1 \frac{dV_{GS}}{dt} + \frac{1}{2} C_2 \frac{dV_{GS}^2}{dt^2} + \frac{1}{3} C_3 \frac{dV_{GS}^3}{d3}. \end{aligned} \tag{3}$$

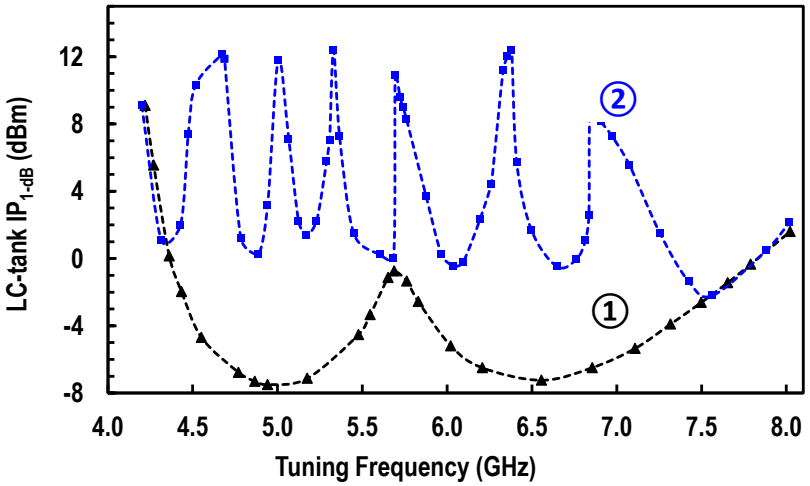

(a)

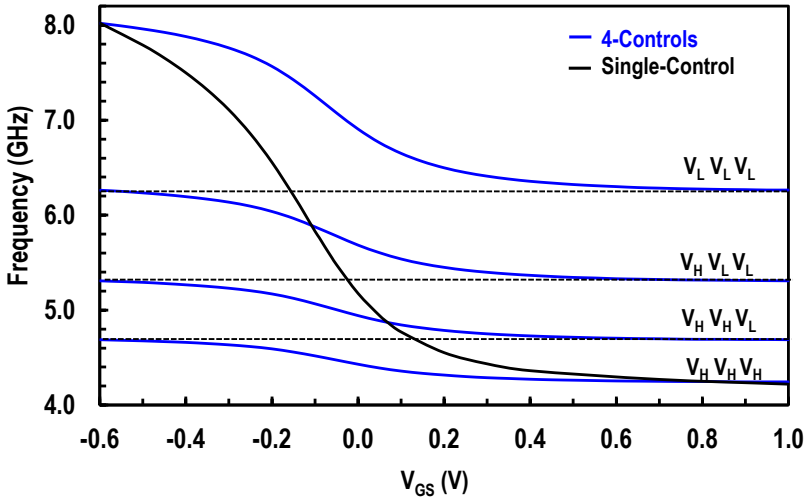

(b)

Figure 3-3: LC-tank linearity with ① continuous single varactor control and ② split varactor control: 3 switched-varactor control plus one continuous varactor control.

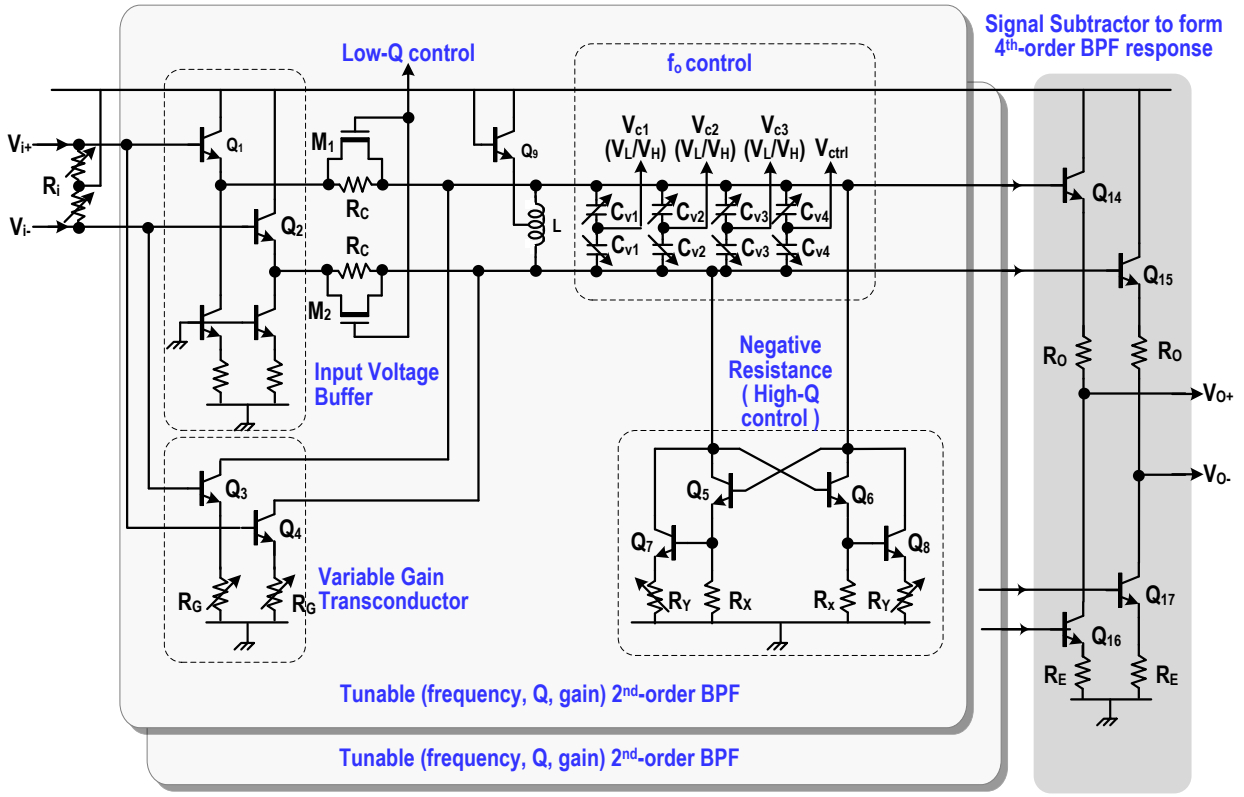

Figure 3-4: Circuit implementation of the Q-enhanced 4th-order differential BPF shown in Figure 3-1.

By dividing the single varactor into four smaller varactors (Figure 3-2②) where the three varactors can be switched in quasi-linear region Ⓐ, the nonlinear capacitance coefficients C_1 and C_2 in (3) of the fourth varactor can be reduced by more than four times for the same V_{GS} swing. This makes the overall nonlinear region behave effectively as four stacked weak-nonlinear regions Ⓒ. In this way, the LC-tank linearity can be increased substantially (Figure 3-3(a)-②). The switched varactor array approach with a larger number of small varactors would improve the linearity further, and overall Q-enhanced LC-tank nonlinearity would then be limited by the negative resistance $-R_N$ nonlinearity. Further details of the switched varactor control scheme are discussed in Chapter 4.

3.2.2 Q-Tuning

The BPF filter Q can be reduced as low as ~4 by decreasing the variable resistor R_C in Figure 3-1, that is composed of a linear resistor R_C (350 Ω) and NMOS $M_{1,2}$ as shown in Figure 3-4. The parallel combination of M_1 and R_C, in series with the 20 Ω output impedance of $Q_{1,2}$, forms the load of the tank. This load varies from 27–370 Ω to control the intrinsic $Q = R_P/\sqrt{L/C}$ from 3–42 of each resonator at 4 GHz. The tanks are driven by emitter follower pair $Q_{1,2}$ in voltage mode, whereas the R_G degenerated pair $Q_{3,4}$ drive the tank in current-mode to provide variable gain transconductance. Note that $Q_{1,2}$ and Q_9 regulate supply voltage and set DC bias across R_C to an equal voltage (V_{CC}-$V_{BE,on}$), forcing $M_{1,2}$ into deep triode region so as to operate as a linear controlled resistor. The diodes Q_9 also provide biasing for the variable-gain transconductor and $-g_m$ cell. Resistance R_G varies from 10-to-670 Ω which can be set to minimum for better NF with large gain and to maximum when the linearity is more important.

The filter Q can be increased up to ~100 by increasing the negative resistance $-R_N$ formed using variable $-g_m$ cell, consisting of degenerated Darlington like pairs $Q_{5\text{-}8}$, R_X, and R_Y for improved linearity. Transistors $Q_{5,6}$ and $R_Y = 200\ \Omega$ give fixed linearized negative resistance, where R_Y also traps the transistor noise. Additional variable negative resistance is achieved from transconductance pair $Q_{7,8}$ and variable resistance R_X. The total $-R_N$ can be approximated as $-2(R_X||R_Y)$. The degenerated Darlington-pair also improves the linearity of $-R_N$ with minimal

center frequency drift when changing the filter Q.

The outputs of the two LC-tanks are subtracted, using an emitter follower pair $Q_{14,15}$ and a common emitter pair $Q_{16,17}$ in Figure 3-4, to form the fourth order BPF shape. The emitter- follower also serves as an output driving buffer with 4.3 mA bias current in each branch. Resistance R_0 is set to $26\ \Omega$ for $50\ \Omega$ output matching with the measurement instruments. Resistance R_E $(22\ \Omega)$ is optimized to match the gains from the outputs of two LC-tanks.

The component values for the 4-8 GHz 2nd-order BPF are provided in Table 3-1.

3.3 Circuit level Noise Analysis

Chapter 2, section 2 covered the system level noise analysis and it was concluded that the 4th-order filter shaping using two parallel 2nd-order BPFs shape the noise as well. Since the dominant noise of the 2nd –order filter are the tank losses, negative transconductance, and gain stage, the output noise follows the signal shaping as the two parallel BPFs noise is uncorrelated. A detailed circuit level analysis is performed and compared with the simulation results in this section.

The first of the two parallel 2nd-order Q-enhanced LC bandpass filter noise model is shown in Figure 3-5, which includes the current driver, voltage driver and the output subtraction circuit. We derive the noise contribution expression at the output of each of the BPFs tanks. The noise expressions for each tank include noise contribution from tank, variable gain amp, input voltage buffer, and output voltage buffer. For the first of the two parallel 2nd-order BPFs, below is the detailed noise expressions derivation.

Tank Noise: The tank noise includes noise contribution due to losses R_P, load resistance R_C, and noise from the negative G_m cell as shown in Figure 3-5 . The total tank impedance can be calculated as

$$R_{Tank} = R_P \parallel R_{-gm} \parallel R_C \tag{4}$$

Then the output noise will be the current noise from the individual resistance sampled by the total

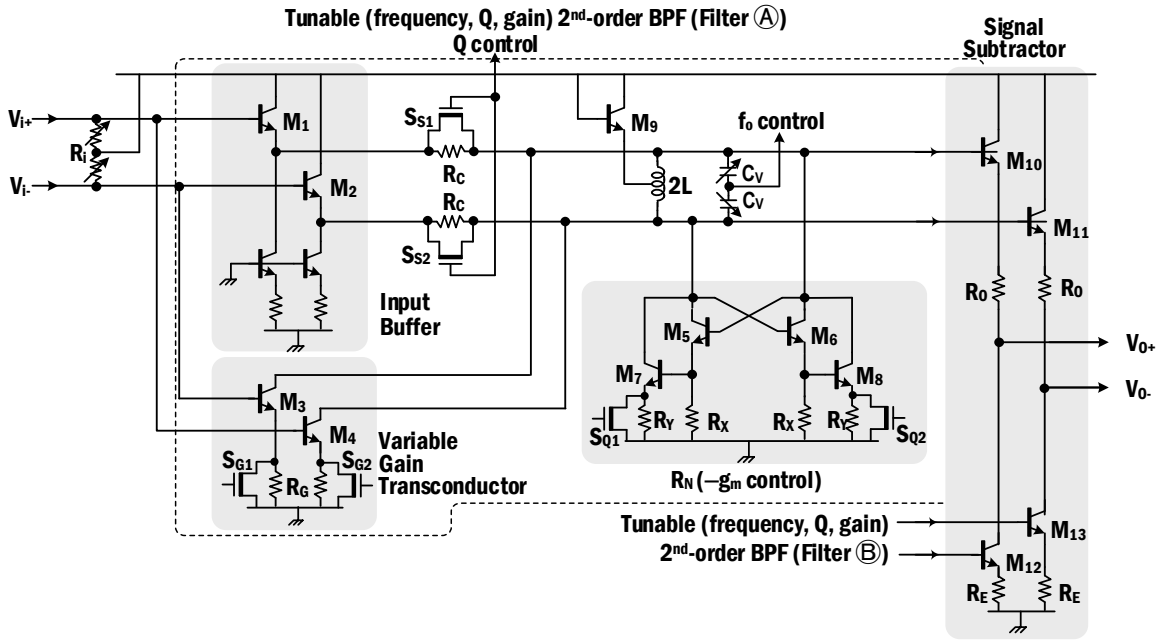

COMPONENT	PARAMETER	VALUE
$M_{1,2}$	$L_{Emitter}$	4 µm
$M_{C1,C2}$	$L_{Emitter}$	4 µm
$R_{s,buffer}$	Ω	455
$S_{S1,S2}$	W/L	30/0.18
R_C	Ω	350
$M_{3,4}$	$L_{Emitter}$	6 µm
$S_{G1,G2}$	W/L	20/0.18
R_G	Ω	677
M_9	$L_{Emitter}$	4 µm
Inductor	2L	650 pH
Varactor C_V	W/L	1008/0.37
$M_{5,6}$	$L_{Emitter}$	4 µm
R_X	Ω	201
$M_{7,8}$	$L_{Emitter}$	2.5 µm
R_Y	Ω	400
$S_{Q1,Q2}$	W/L	20/0.2
$M_{10,11}$	$L_{Emitter}$	4 µm
R_0	Ω	26
$M_{12,13}$	$L_{Emitter}$	4 µm
R_E	Ω	22

Table 3-1: Component values of 2nd-order BPF

tank resistance R_{Tank}

$$\overline{V_{n,T}^2} = \frac{4kT}{R_P}R_{Tank}^2 + \frac{4kT}{R_C}R_{Tank}^2 \quad + 4kT\left(\gamma_{Eq}G_m + \frac{1}{R_Y}\right)R_{Tank}^2 \tag{5}$$

$$\overline{V_{n,T}^2} = 4kT\left[\frac{1}{R_C} + \frac{1}{R_P} + \left(\gamma_{Eq}G_m + \frac{1}{R_Y}\right)\right]R_{Tank}^2, \tag{6}$$

where $\gamma_{EQ}G_m = \gamma(g_{mn} + g_{dsn})$ triode nMOS switch noise for the negative G_m. Then the total tank noise can be written as

$$\overline{V_{n,T}^2} = 4kT\left[\frac{1}{R_C} + \frac{1}{R_P} + \gamma(g_{mn} + g_{dsn}) + \frac{1}{R_Y}\right]R_{Tank}^2. \tag{7}$$

Variable Gain Amp Noise: The variable gain amplifier noise contribution includes the base resistance r_B and the G_{m2} of the whole gain stage including the variable resistance $1/R_G$ as modelled in Figure 3-5. The total noise can be written as

$$\overline{V_{n,G}^2} = 4kTr_b\left(\frac{g_{m2}}{1 + g_{m2}R_G}\right)^2 R_{Tank}^2 + 4kTG_{m2}R_{Tank}^2 \tag{8}$$

$$G_m = \frac{g_{m2}}{1 + g_{m2}R_G} \approx \frac{1}{R_G}$$

$$\overline{V_{n,G}^2} = 4kTr_b\left(\frac{1}{1/g_{m2} + R_G}\right)^2 R_{Tank}^2 + \frac{4kT}{R_G}R_{Tank}^2. \tag{9}$$

Input Voltage Driver Noise: The input voltage driver consists of an input matched resistor R_{in}, common collector stage Q_1 and the tank load resistance R_C. The dominant noise will be from of the input matched resistor R_{in}, and the tank load resistor R_C and can be written as

$$\overline{V_{n,Dı}^2} = 2qI_C\left(\frac{1}{g_m^2}\right)\left(\frac{1}{R_C^2}\right)R_{Tank}^2 = 2kTg_m\left(\frac{1}{g_m^2}\right)\left(\frac{1}{R_C^2}\right)R_{Tank}^2 \tag{10}$$

$$\overline{V_{n,Dı}^2} = 4kT\left(\frac{1}{2g_mR_C^2}\right)R_{Tank}^2\,. \tag{11}$$

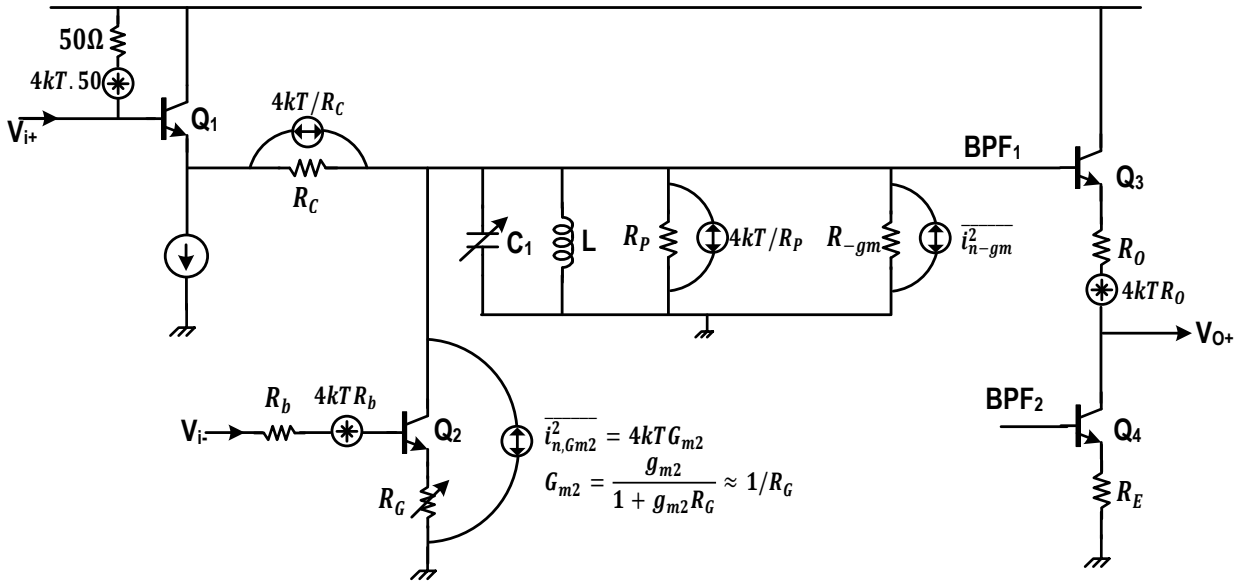

Figure 3-5: Circuit noise model of the first Q-enhanced 2nd-order BPF.

Output Voltage Driver Noise: The output subtraction part of the first 2nd-order BPF includes Q_3 buffer and an output matched resistorR_0. The noise can be expresses as

$$\overline{V_{n,\,Do}^2} = 2qI_C\left(\frac{1}{g_{m3}^2}\right) + \frac{1}{2}4kTR_0 \tag{12}$$

$$\overline{V_{n,\,Do}^2} = 4kT\left(\frac{1}{2g_{m3}}\right) + \frac{1}{2}4kTR_0 \tag{13}$$

Total Noise: The total noise at the tank output can be expresses as

$$\overline{V_{n,\,T}^2} = 4kTR_{Tank}^2\left[\frac{1}{R_P} + \frac{1}{R_C} + \gamma(g_{mn} + g_{dsn}) + \frac{1}{R_Y} + \frac{r_b}{(1/g_{m2} + R_G)^2} + \frac{1}{R_G} + \frac{1}{2g_mR_C^2}\right] + 4kT\left(\frac{1}{2}\right)\left(\frac{1}{g_{m3}} + R_0\right) \tag{14}$$

Gain: The gain of the filter is needed to calculate the noise figure. The filter gain has two paths, one is from input through voltage buffer and the other is through variable gain amplifier to the output of the tank. Then the gain can be expresses as below, note that the 1/2 term is due to resistive impedance matching.

$$A_v = \frac{1}{2}\left(R_{Tank}G_{m2} + \frac{R_P \parallel R_{-gm}}{R_P \parallel R_{-gm} + R_C}\right) \tag{15}$$

$$A_v = \frac{1}{2}\frac{R_P \parallel R_{-gm}}{R_P \parallel R_{-gm} + R_C}(R_CG_{m2} + 1) \tag{16}$$

In terms of Q, the gain can be expressed as

$$R_{Tank} = \frac{R_P \parallel R_{-gm}.R_C}{R_P \parallel R_{-gm} + R_C} \quad \Longrightarrow \quad \frac{R_{Tank}}{R_C} = \frac{R_P \parallel R_{-gm}}{R_P \parallel R_{-gm} + R_C}, \quad R_CG_{m2} + 1 \approx R_CG_{m2}$$

$$A_v \cong \frac{1}{2}\frac{R_{Tank}}{R_C}R_CG_{m2} \quad , \qquad R_CG_{m2} = \frac{2A_vR_C}{R_{Tank}} = \frac{2A_vR_C}{Q\sqrt{L/C}} \qquad Q = \frac{R_{Tank}}{\sqrt{L/C}}$$

$$A_v \cong \frac{1}{2} G_{m2} Q \sqrt{L/C} \tag{17}$$

Noise Factor: The noise factor of any system can be expresses as

$$F = \frac{SNR_{in}}{SNR_{out}} = \frac{P_{in}/\overline{V_{n,in}^2}}{P_{out}/\overline{V_{n,out}^2}} = \frac{\overline{V_{n,in}^2}}{A_v^2 \overline{V_{n,out}^2}} = \frac{A_v^2(\overline{V_{n,in}^2} + \overline{V_{n,DUT}^2})}{A_v^2 \overline{V_{n,in}^2}} \tag{18}$$

$$F = 1 + \frac{\overline{V_{n,DUT}^2}/A_v^2}{\overline{V_{n,in}^2}} \tag{19}$$

Due to input matching transistor R_{in}, the noise factor can be expresses as

$$F = 1 + \frac{\overline{V_{n,Rin}^2} + \overline{V_{n,T}^2}/A_v^2}{\overline{V_{n,in}^2}} = 1 + \left(\frac{4kTR_{in}}{4kTR_s}\right) + \frac{\overline{V_{n,T}^2}/A_v^2}{\overline{4kTR_s}} = 2 + \frac{\overline{V_{n,T}^2}/A_v^2}{4kTR_S} \tag{20}$$

Substituting the $\overline{V_{n,T}^2}$ and A_v^2 from (14) and (16) respectively in (20) results in

$$F = 2 + \frac{4kT}{4kTR_S}\left(\frac{R_{Tank}^2\left(\frac{1}{R_P} + \frac{1}{R_C} + \gamma(g_{mn} + g_{dsn}) + \frac{1}{R_Y} + \frac{r_b}{(1/g_{m2} + R_G)^2} + \frac{1}{R_G} + \frac{1}{2g_m R_C^2}\right)}{\frac{1}{4}\left(\frac{R_P \parallel R_{-gm}}{R_P \parallel R_{-gm} + R_C}\right)^2 (R_C G_{m2} + 1)^2}\right)$$

$$+ \frac{4kT}{4kTR_S}\left(\frac{\left(\frac{1}{2}\right)\left(\frac{1}{g_{m3}} + R_0\right)}{\frac{1}{4}\left(\frac{R_P \parallel R_{-gm}}{R_P \parallel R_{-gm} + R_C}\right)^2 (R_C G_{m2} + 1)^2}\right) \tag{21}$$

$$= 2 + \left[\frac{\left(\frac{R_P \parallel R_{-gm}}{R_P \parallel R_{-gm} + R_C}\right)^2 R_C^2\left(\frac{1}{R_P} + \frac{1}{R_C} + \gamma(g_{mn} + g_{dsn}) + \frac{1}{R_Y} + \frac{r_b}{\left(\frac{1}{g_{m2}} + R_G\right)^2} + \frac{1}{R_G} + \frac{1}{2g_m R_C^2}\right)}{R_S \frac{1}{4}\left(\frac{R_P \parallel R_{-gm}}{R_P \parallel R_{-gm} + R_C}\right)^2 (R_C G_{m2} + 1)^2}\right.$$

$$+\frac{\left(\frac{1}{2}\right)\left(\frac{1}{g_{m3}}+R_0\right)}{R_S\frac{1}{4}\left(\frac{R_P \parallel R_{-gm}}{R_P \parallel R_{-gm}+R_C}\right)^2 (R_C G_{m2}+1)^2}\Bigg] \tag{22}$$

$$= 2+\frac{4}{R_S}\frac{R_c^2\left(\frac{1}{R_P}+\frac{1}{R_C}+\gamma(g_{mn}+g_{dsn})+\frac{1}{R_Y}+\frac{r_b}{(1/g_{m2}+R_G)^2}+\frac{1}{R_G}+\frac{1}{2g_m R_C^2}\right)}{(R_C G_{m2}+1)^2}$$

$$+\frac{4}{R_S}\frac{\left(\frac{1}{2}\right)\left(\frac{1}{g_{m3}}+R_0\right)}{(R_C G_{m2}+1)^2} \tag{23}$$

Where $R_C = 350 \implies 1/R_C$, $1/2g_m R_C$ can be ignored. $R_C G_{m2}+1 \approx R_C G_{m2}$ and $1/R_P/(R_C G_{m2}+1)^2$ are negligible. Then (23) can be expressed as

$$F = 2+4\,\frac{R_c^2\left(\gamma(g_{mn}+g_{dsn})+\frac{1}{R_Y}+\frac{r_b}{(1/g_{m2}+R_G)^2}+\frac{1}{R_G}\right)}{R_S R_C^2 G_{m2}^2}$$

$$+4\,\frac{\left(\frac{1}{2}\right)\left(\frac{1}{g_{m3}}+R_0\right)}{R_S R_C^2 G_{m2}^2} \tag{24}$$

$$= 2+4\,\frac{\left(\gamma(g_{mn}+g_{dsn})+\frac{1}{R_Y}+\frac{r_b}{(1/g_{m2}+R_G)^2}+\frac{1}{R_G}\right)}{R_S G_{m2}^2}+4\frac{\left(\frac{1}{2}\right)\left(\frac{1}{g_{m3}}+R_0\right)}{R_S R_C^2 G_{m2}^2} \tag{25}$$

In terms of Q, the noise factor using (17) can be expressed as

$$F = 2+4\left(\frac{\gamma(g_{mn}+g_{dsn})+\frac{1}{R_Y}}{R_S G_{m2}^2}+\frac{r_b}{R_S G_{m2}^2}\left(\frac{g_{m2}}{1+g_{m2}R_G}\right)^2+\frac{1}{R_S R_G}\frac{1}{G_{m2}^2}\right)$$

$$+4\frac{\left(\frac{1}{2}\right)\left(\frac{1}{g_{m3}}+R_0\right)}{R_S R_C^2 G_{m2}^2} \tag{26}$$

$$= 2 + 4\left(\frac{1}{R_S G_{m2}} + \frac{\gamma(g_{mn} + g_{dsn}) + \frac{1}{R_Y}}{R_S G_{m2}^2} + r_b\right) + 4\frac{\left(\frac{1}{2}\right)\left(\frac{1}{g_{m3}} + R_0\right)}{R_S R_C^2 G_{m2}^2} \quad (27)$$

$$= 2 + 4\left(\frac{Q_1\sqrt{L/C_1}}{2R_S A_v} + \frac{r_b}{R_S} + \frac{\left(\gamma(g_{mn} + g_{dsn}) + \frac{1}{R_Y}\right)}{4R_S A_v^2} Q_1^2 {}^{L}/_{C_1} + \frac{\left(\frac{1}{2}\right)\left(\frac{1}{g_{m3}} + R_0\right)}{R_S R_C^2 G_{m2}^2}\right) \quad (28)$$

$$F = 2 + 4\left(\frac{Q_1}{2A_V}\frac{\sqrt{{}^{L}/_{C_1}}}{R_S} + \frac{r_b}{R_S} + Q_1^2\frac{\left(\gamma(g_{mn} + g_{dsn}) + \frac{1}{R_Y}\right){}^{L}/_{C_1}}{4A_v^2 R_S} + Q_1^2\frac{\left(\frac{1}{g_{m3}} + R_0\right){}^{L}/_{C_1}}{8A_v^2 R_S R_C^2}\right) \quad (29)$$

For low Q (<15), when the 4th-order BPF fractional bandwidth is >15%, the noise contribution from the negative gm is negligible

$$F = 2 + 4\left(\frac{Q_1}{2A_V}\frac{\sqrt{{}^{L}/_{C_1}}}{R_S} + \frac{r_b}{R_S} + \frac{Q_1^2}{8A_v^2}\frac{\left(\frac{1}{g_{m3}} + R_0\right){}^{L}/_{C_1}}{R_S R_C^2}\right) \quad (30)$$

Second BPF Output Current Driver Noise: For the second of the two parallel 2nd-order BPF, all the noise analysis will be same as that of the first BPF except the output subtraction circuit where the driver in this case is a degenerated transconductance stage. The noise modelling is shown in Figure 3-6. The output noise for the current driver can be expressed as

$$\overline{V_{n,G}^2} = 4kT\frac{g_{m4}}{1 + g_{m4}R_E}\left(\frac{R_L}{2}\right)^2 \quad (31)$$

$$1 + g_m R_E \gg 1 \text{ for } R_E = 22\Omega \text{ and } g_m = 50\ mS$$

Noise at the Tank output will be

$$\overline{V_{n,Go}^2} = 4kT\frac{(R_L/2)^2}{R_E}/\left(\frac{R_L/2}{R_E}\right)^2 \quad (32)$$

$$\overline{V_{n,Go}^2} = 4kTR_E$$

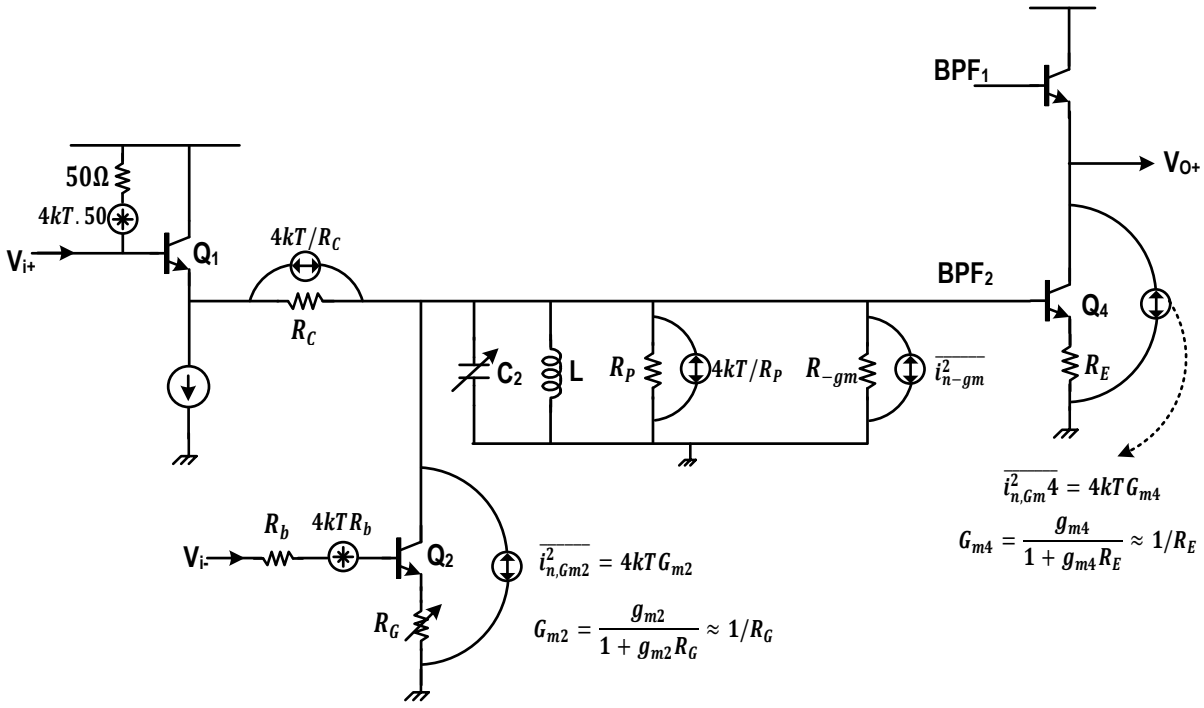

Figure 3-6: Circuit noise model of the second Q-enhanced 2nd -order BPF.

$$F = 2 + 4\,\frac{\left(\gamma(g_{mn} + g_{dsn}) + \dfrac{r_b}{(1/g_{m2} + R_G)^2} + \dfrac{1}{R_G}\right)}{R_S G_{m2}^2} + 4\,\frac{R_E}{R_S R_C^2 G_{m2}^2} \tag{33}$$

In terms of Q, the noise factor can be expressed as

$$F = 2 + 4\left(\frac{Q_2}{2A_V}\frac{\sqrt{L/C_2}}{R_S} + \frac{r_b}{R_S} + \frac{Q_1^2}{4A_v^2}\frac{\left(\gamma(g_{mn} + g_{dsn}) + \dfrac{1}{R_Y}\right)L/C_1}{R_S} + \frac{Q_2^2}{4A_v^2}\frac{R_E\,L/C_2}{R_S R_C^2}\right) \tag{34}$$

For low Q (<15), when the 4th-order BPF fractional bandwidth is >15%, the noise contribution from the negative gm is negligible

$$F = 2 + 4\left(\frac{Q_2}{2A_V}\frac{\sqrt{L/C_2}}{R_S} + \frac{r_b}{R_S} + \frac{Q_2^2}{4A_v^2}\frac{R_E\,L/C_2}{R_S R_C^2}\right) \tag{35}$$

Figure 3-7(a) shows the plots of noise figure equations and simulations versus 4th-order fractional bandwidth of 2% to 25% for the filter gain of 10 dB. The first 2nd-order BPF noise figure theory, Eq. (29), and simulation are plotted at the center-tuned frequency f_1 whereas the theory, Eq. (34), and simulation for the second BPF are plotted at center-frequency f_2. Also the 4th-order noise figure simulation is plotted at center frequency f_c. The plot shows a good match between theory and simulation for the 2nd-order BPFs at f_1 and f_2. The noise figure of the 4th-order BPF is similar to that of 2nd-order BPF. The noise figure of the 4th-order for smaller factional bandwidth is slightly lower than the 2nd-order due to noise shaping resulting from two high Q parallel BPFs and ripple magnitude. At lower fractional bandwidth when the BPF tank contribution is not dominant due to very low Q on the order of 5~10, the noise figure of 4th-order at f_c is slightly higher than the 2nd-order due to reduced noise shaping.

Figure 3-7 (b) shows the % noise contribution from dominant components in 4th-order BPF circuit shown in Figure 3-4. The noise contribution is plotted at block level from different gain stage, negative gm, input buffer, source, input matching, and the subtraction circuit. The noise contribution from the gain stage is dominant. The second dominant contribution is from negative

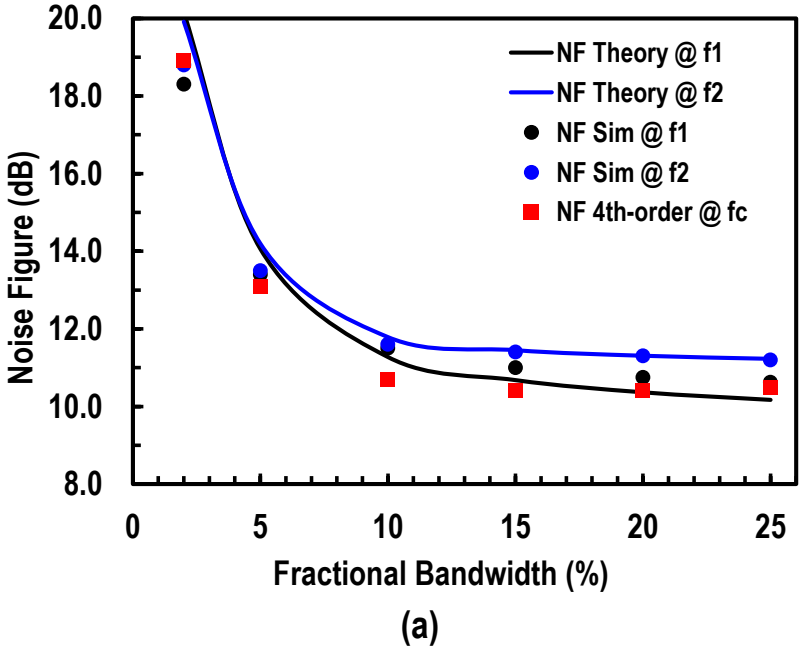

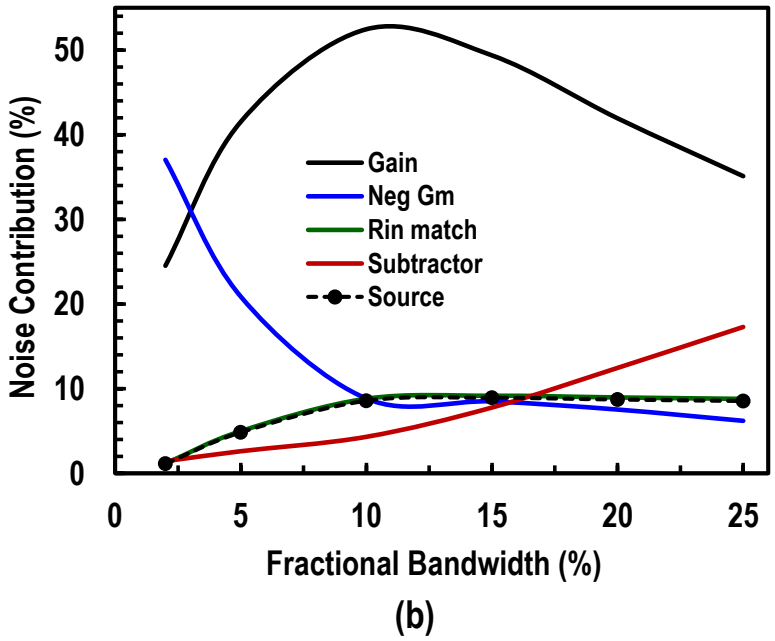

Figure 3-7: (a) Noise Figure simulations and theory for the two 2nd-order parallel BPFs and 4th order resultant filter for fractional bandwidth of 2% to 25% and (b) % noise contribution from the dominant blocks.

Table 3-2: % Noise contribution from all the components of circuit in **Figure 3-4**

%BW	$M_{G1,2}$	$Q_{3,4}$	$M_{N1,2}$	Rx	Q_{5-8}	R_S (50Ω)	R_{in} (50Ω)	Ry	Rc	Ind Loss R_P	$Q_{14,15}$	$Q_{16,17}$
2	21.66	2.86	11.93	5.84	17.42	1.14	1.17	1.84	2.6	3.16	0.66	0.78
5	23.78	17.74	4.26	4.42	9.96	4.85	4.99	2.24	1.26	3.74	1.1	1.52
10	21.95	30.5	0.2	3.04	4.4	8.58	8.82	1.2	1.98	3.96	1.84	2.48
15	19.12	30.24	0.2	2.42	4.64	8.92	9.17	1.24	2.86	5.92	3.33	4.45
20	16.7	25.23	0.1	2.34	3.98	8.72	8.97	1.12	4.75	1.88	5.32	7.14
25	14.22	20.88	0.1	2.02	3.51	8.55	8.8	0.58	4.64	1.42	7.43	9.86

gm at smaller % bandwidth requiring high Q BPFs and reduces at higher %bandwidth or low Q bandpass filter. At fractional bandwidth of 10~15% and above the Q enhancement is not needed and each BPF Q needs to be lowered than the LC-tank Q using variable resistor R_C as explained in (section 3.2.3) Q tuning.

3.4 Measurement Results

The filter is fabricated in 0.13 μm SiGe BiCMOS process, and the core circuit excluding pads occupies 0.53 × 0.7 mm^2 (Figure 3-8). The input resistance R_i in Figure 3-4 is made variable from 50-to-1 kΩ for the measurement of both matched and actual large load conditions.

3.4.1 Bandwidth Tuning:

Figure 3-9 shows the measured filter response at f_c=6 GHz when gain is set to 0 dB and R_i=50 Ω. When the passband ripple magnitude (Mr) is constrained to less than 0.5 dB, the filter achieves 2-to-25% fractional bandwidth tuning range (Figure 3-9(a)). Within the 3-dB passband, the worst case measured group delay is less than 410 ps as shown in Figure 3-9(b). NF measurements were done for both input matched and high impedance cases. In Figure 3-10(a), for the R_i=1 kΩ case, the measured NF is 7.6 dB at 25% fractional BW and degrades to 18 dB when the filter BW decreases to 2% due to the increase of noise power in the negative resistance cell as the filter Q increases, manifesting the sensitivity-selectivity tradeoff in typical Q-enhanced LC filters. When R_i=50 Ω, the NF is degraded by 4~5 dB because the input signal power halved due to the resistive matching. The NF can be lowered substantially by increasing gain from the variable gain transconductor at the expense of linearity degradation. The measured in-band P_{-1dB} ranges –1~4 dBm when the input is matched to 50 Ω, resulting in 151~166 dB of normalized dynamic range (DR) as the fractional bandwidth varies from 2% to 25% in Figure 3-10(a). The normalized DR =174+ P_{-1dB}-NF, is the ratio of in-band 1-dB input compression point to the input-referred noise-floor with 1-Hz BW [44].

The group delay variation and phase variation within 3-dB bandwidth is plotted in Figure 3-10(b) versus fractional bandwidth. The phase variation within the 3-dB bandwidth is

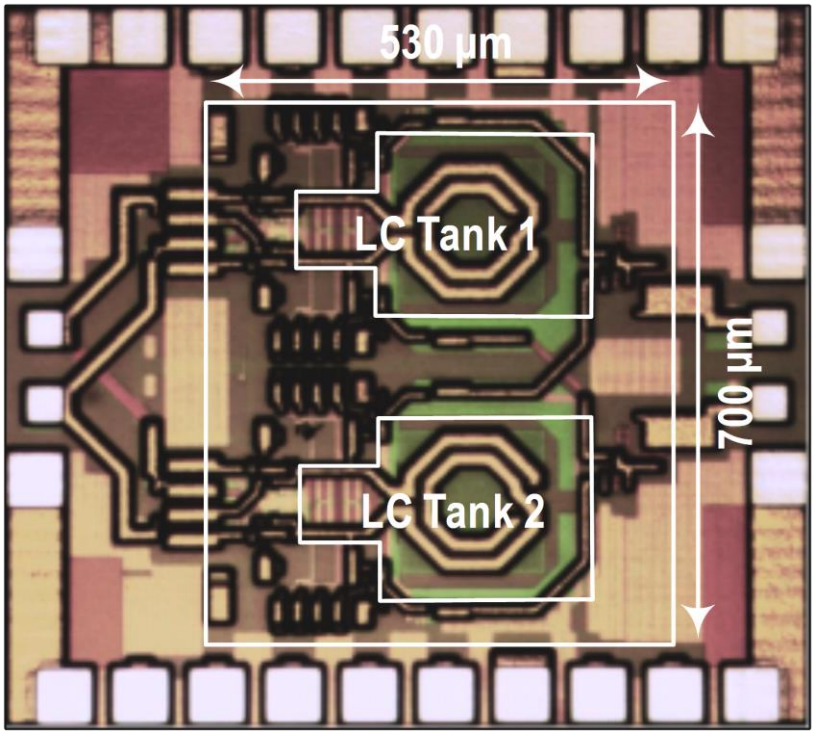

Figure 3-8: Chip photograph (1.05×0.95 mm^2 including pads).

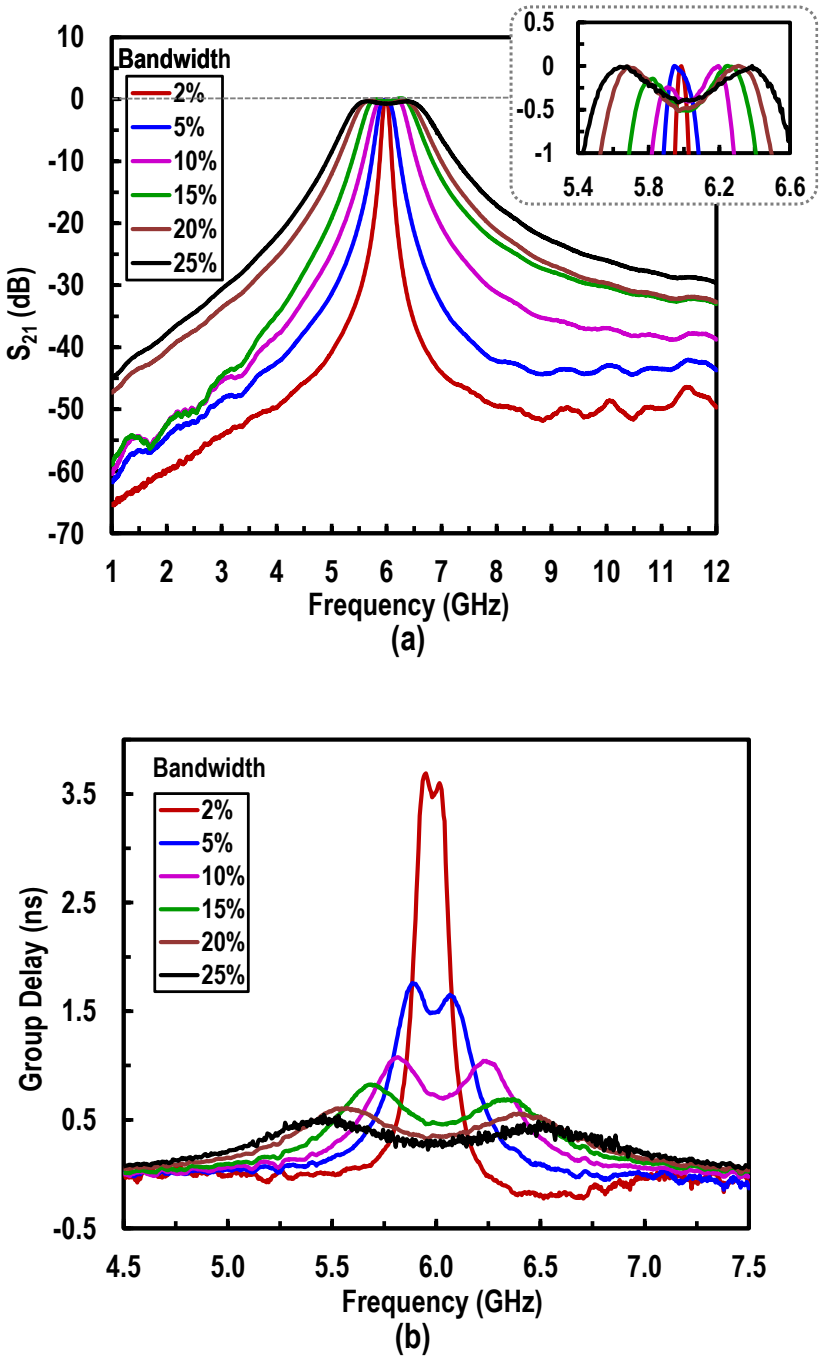

Figure 3-9: Measured (a) filter response at 6 GHz with fractional bandwidth tuning from 2-to-25% and (b) measured group delays.

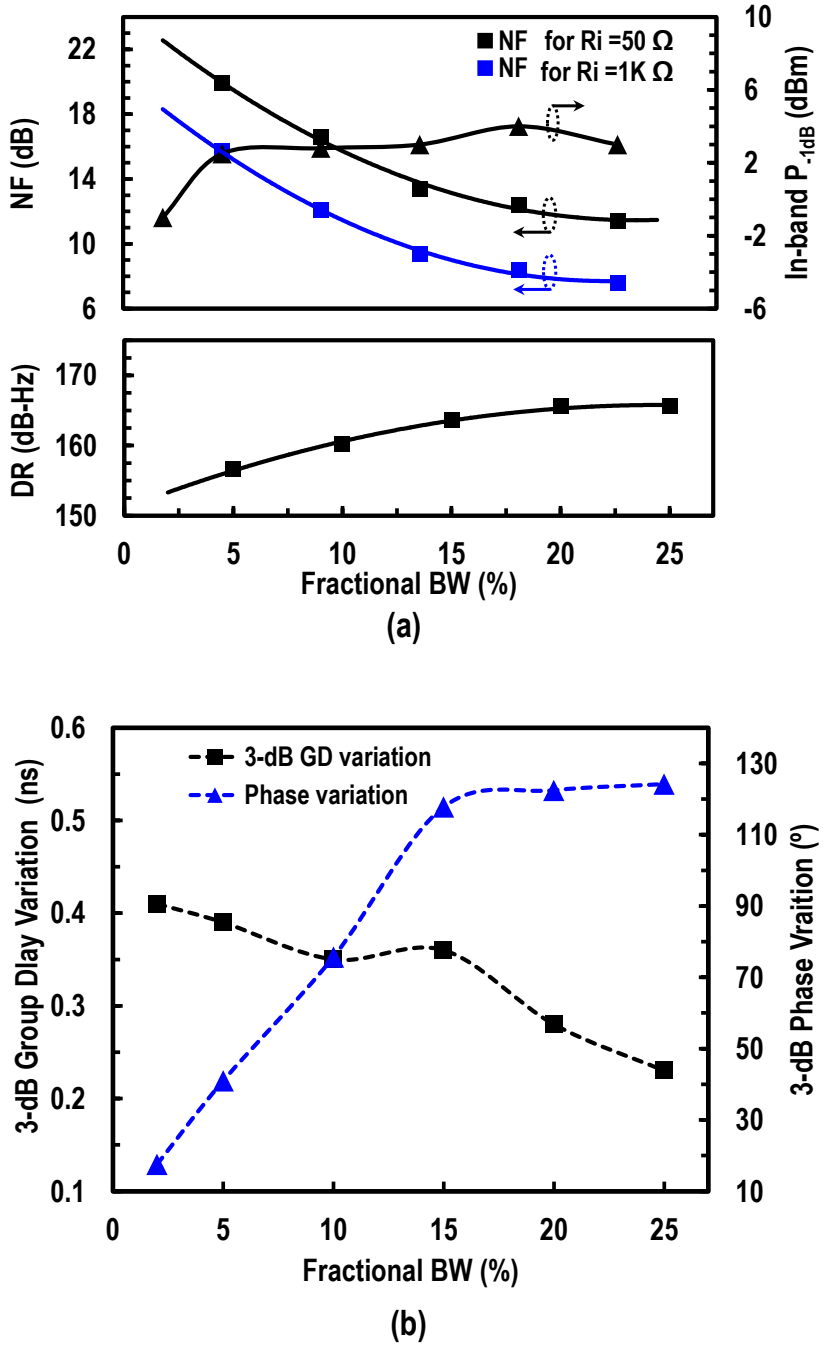

Figure 3-10: (a) Measured NF, in-band P_{-1dB}, and dynamic range for fractional bandwidth tuning from 2-to-25% and (b) 3-db group delay variation and phase variation.

$$\theta(\omega)_{3dB} = \tau(\omega) \times \omega_{3dB} \quad (4)$$

where $\tau(\omega)$ is the group-delay in seconds, ω_{3dB} is the bandwidth of the filter . The group delay variation varies from 0.41 ns to 0.23 ns and the phase varies from 17.6° to 124° for fractional bandwidth from 2% to 25%.

3.4.2 Out-Of-Band Linearity Measurement

Figure 3-11(a)-(b) show the out-of-band (OOB) measured linearity tests at a center frequency of 6 GHz for fractional bandwidths of 2, 5, 10 and 25%, corresponding to 120, 300, 600 and 1500 MHz bandwidths, respectively. The tests were performed for both upper and lower offset frequencies from the center frequency of 6 GHz. The blocker P_{-1dB} test is shown in Figure 3-11 (a), where a large blocker is injected at offset frequency and a small signal is at center frequency of 6 GHz. The blocker power is increased until the in-band signal compresses by 1 dB and is plotted for upper and lower sides. Similarly, the OOB IIP3 is performed for upper and lower side offset frequencies from 6 GHz and is plotted in Figure 3-11(b).

3.4.3 Frequency Tuning

Figure 3-12(a) shows the measured filter response for constant fractional BW (equivalent $Q = 20$) covering the entire frequency band of 4-8 GHz. The pass-band ripple is less than 0.2 dB. The filter center frequency tuning is continuous, but for reporting purposes, is plotted here for discrete frequency steps. The filter has an excellent out-band-rejection on the lower side away from the center frequency, and is more than 60 dB at 1 GHz. On the higher frequency side, the out-of-band rejection is more than 42 dB and saturates due to the high frequency zero caused by the mismatch in bandwidths of each resonator and DC blocking capacitors. The measured NF and in-band P_{-1}dB for the constant fractional BW are plotted in Figure 3-12(b) for the input matched case of $R_i = 50\ \Omega$. The gain is kept constant at 5 dB and the S21 plot is normalized to 0 dB. The measured DR is 153.2±1 dB·Hz for the entire band in Figure 3-12(b) and remains constant as expected since the Q of the BPF remains constant. The filter can also be controlled to have an absolute BW response as shown in Figure 3-13(a). In this case the bandwidth at each center frequency is 200 MHz and

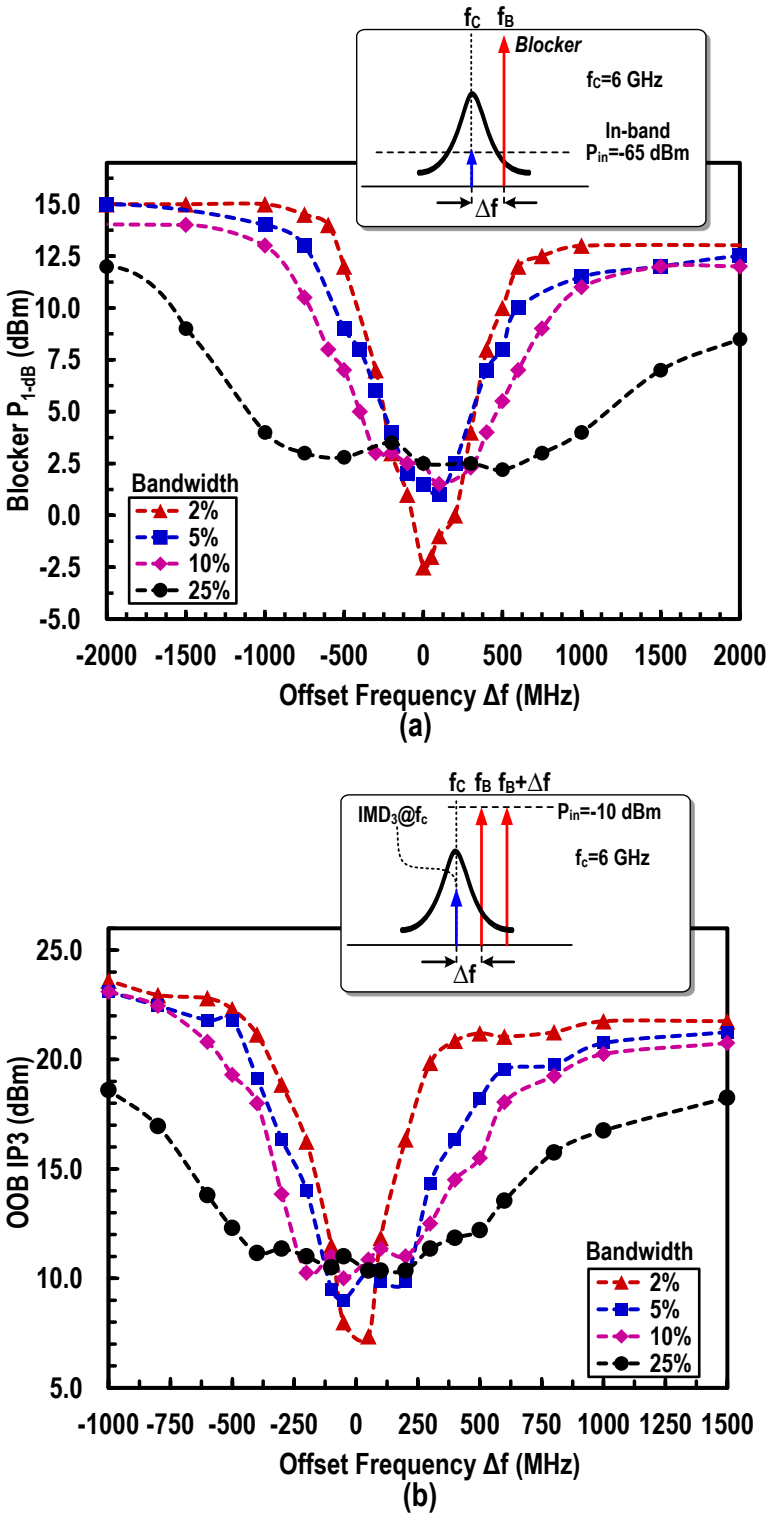

Figure 3-11: (a) Blocker P_{-1dB} measurements for 2, 5, 10 and 25% and (b) OOB IP3 measurements for 2, 5, 10 and 25%.

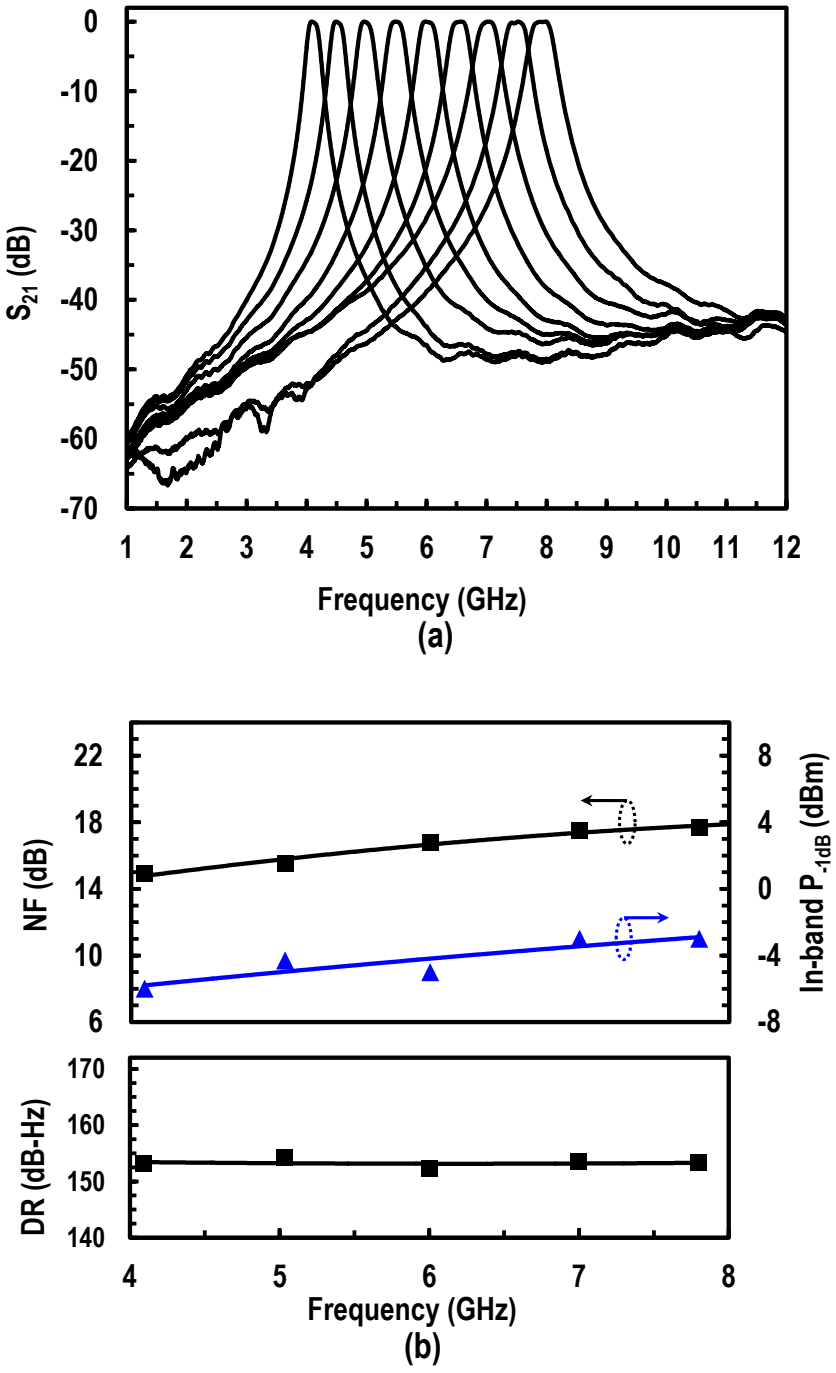

Figure 3-12**:** Measured (a) frequency tuning with constant fractional bandwidth (Q=20) and (b) NF, in-band P_{-1dB}, and DR for constant fractional bandwidth.

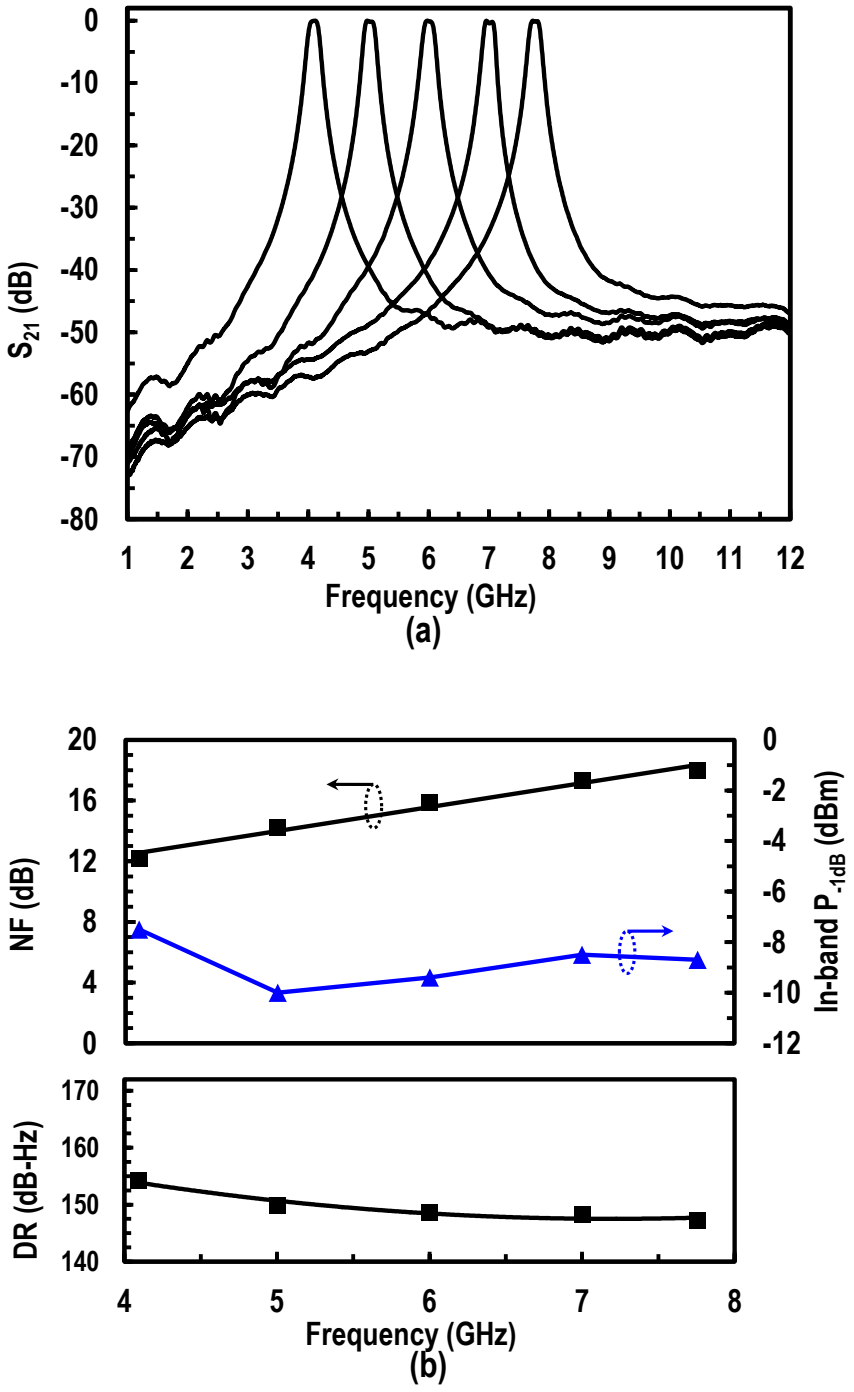

Figure 3-13: Measured (a) frequency tuning with absolute bandwidth of 200 MHz and (b) NF, in-band P_{-1dB}, and DR for absolute bandwidth of 200MHz.

the pass-band ripple is less than 0.2 dB. The filter has more than 60 dB and 45 dB of rejection toward the lower- and upper-side frequencies, respectively. The measured NF and in-band P-1dB for the absolute BW of 200 MHz are plotted in Figure 3-13 (b). The DR varies from 154.6 dB to 147.3 dB from 4 to 8 GHz respectively. The DR degrades at high frequencies since more Q is required to maintain constant bandwidth of 200 MHz, in turn requiring more negative gm and hence increased NF.

3.4.4 Gain Tuning

The filter gain can be tuned based on the NF and linearity trade-off due to the current-mode driving (Figure 3-4) using a variable transconductor. Figure 3-14(a) shows the measured gain tuning centered at 6 GHz for both input matched and high impedance cases. The corresponding measured NF and P_{-1dB} are plotted in Figure 3-14 (b). The DR range varies 153.2 dB to 158.6 dB.

Table 3-3 summarizes and compares measured performances with previous on-chip Q-enhanced LC and N-path filters. The proposed filter achieves one of the widest bandwidth tuning ranges (120 MHz to 1.5 GHz), better DR, and higher out-of-band rejection compared to prior state-of-the art integrated filters, making this design favorable for operation at microwave frequencies. The power consumption of the filter is on par with, or better than, the N-path approach at C-band and beyond.

Figure 3-15 is plot of the power consumption of the published N-path filters, mostly at frequencies below 3 GHz. Both lower and upper frequencies power consumption are reported for most of these filters and the trend against frequency is shown with a dashed line. .Figure 3-16 shows the power consumption of the filtering part only from Figure 3-15. As can be seen, the proposed LC filter approach demonstrates a favorable power consumption trend for higher microwave frequency designs. It is also important to note that in addition to power consumption being a function of operating frequency, the N-path filter's OOB attenuation degrades at higher frequencies due to switch parasitic and multi-phase clock inaccuracies.

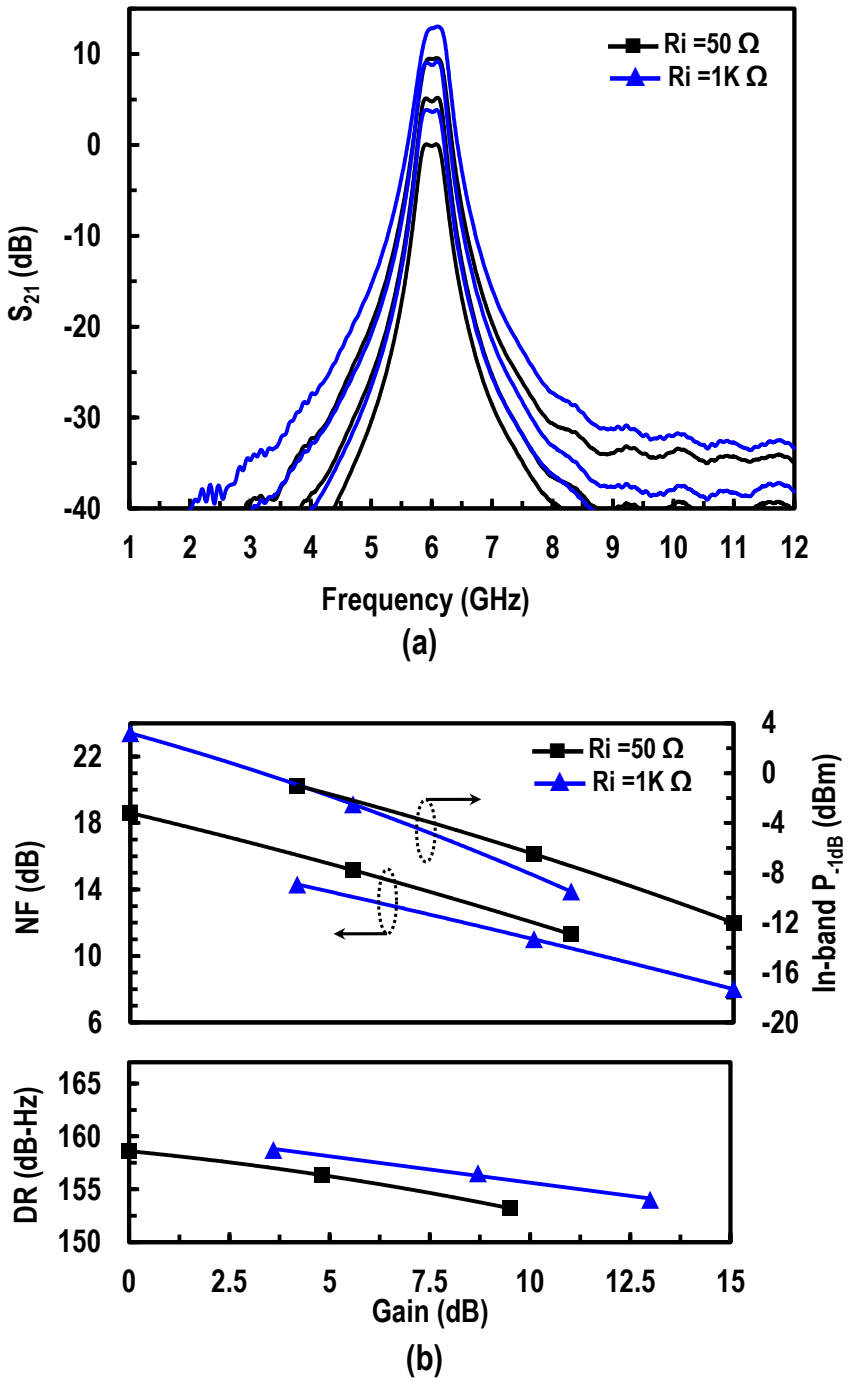

Figure 3-14: Measured (a) gain control at 6 GHz and (b) NF, in-band P_{-1dB}, and DR versus gain.

Table 3-3: Comparison with State Of The Art BPFs

Authors	This Work	C. Luo, TMTT'16 [24]	R. Chen, JSSC'15 [19]	M. Hasan, IMS'16 [20]	J. Zhou, JSCC'14 [11]	D. Murphy, JSSC'12 [12]	M. Darvishi, ISSCC'12 [27]	F. Hu, IMS'14 [36]	M. Lee, TMTT'11 [37]	B. Georgescu, JSSC'06 [38]
Type	Q-enhanced LC Filter	N-path LNA	N-path+DT RX	N-path Filter	N-path RX	N-path RX	N-path Filter	Active-L Ladder Filter	TL-based Active Filter	Q-enhanced LC Filter
Freq. (GHz) /Tunability	4.1 – 7.9 / Tunable	0.4 – 6 / Tunable	0.5 – 3 / Tunable	0.2 – 1.2 / Tunable	0.3 –1.7 / Tunable	0.3 – 2.9 / Tunable	0.3 – 1.2 / Tunable	1.5 / Fixed	1.58 / Fixed	2.0 / Fixed
Bandwidth (MHz)	120 – 1500 @6 GHz	15	1 – 30	6.2	6.2	–	21	1000	126.4	130
Filter Q	4 – 50	–	–	–	–	–	19-57	1.5	12.5	15
NF (dB) @Gain (dB)	7.6 – 15.7 @4.5 dB	3.6 – 4.9 @ 12 – 8	5.5 – 8.8[e] @35 – 29	4.5 – 6.2 @ 21	4.2 – 5.6 @ 19 – 34	1.9 @ 58	9.5 @ 3.5	19[k] @ -1.8	15	15 @ 0
IP_{-1dB} (dBm)	−1 – +4.0	< 10	−34 – −30	–	< −20.6[h]	< −13[j]	−4.4	−21	−13.8	−6.6
Normalized DR[a] (dB·Hz)	151 – 166	<179	<135	–	<148.4	<159	160	134	145.2	152
Ultimate Rejection (dB)	>65[b] >52[c]	60 [d] <18 @ 6GHz	>45	<60[g]	–	<15	>55	>40	52.3	>38
Area (mm^2)	0.371	0.28	7.8	2.2	1.2	1.1	0.127	0.18	0.92	0.81
Power (mW)	112 – 125	81 – 209	250 – 600[f]	33 – 70	74.6 – 83/ 146.6 –155[i]	49.4–99.8	17.6	30	14.4	16.6
Process	130nm SiGe BiCMOS	32nm SOI CMOS	65nm CMOS	65nm CMOS	65nm CMOS	40nm CMOS	65nm CMOS	130nm CMOS	180nm CMOS	180nm CMOS

[a]Calculated from 174+IP_{-1dB} – NF, [b],[c]upper and lower side of center frequency, [d]Single notch point at 0.6 GHz for fc=0.4 GHz, [e]After de-embedding off-chip balun NF, [f]including CLK synthesizer power of 40mW– multi-phase CLK power is 405 mW at 3GHz, [g]Bandpass with two notches, [h]calculated from IIP3 graph @ 4MHz offset, [i]with Tx canceller/without Tx canceller, [j]calculated from IIP3 graph @ 3MHz offset, [k]simulation

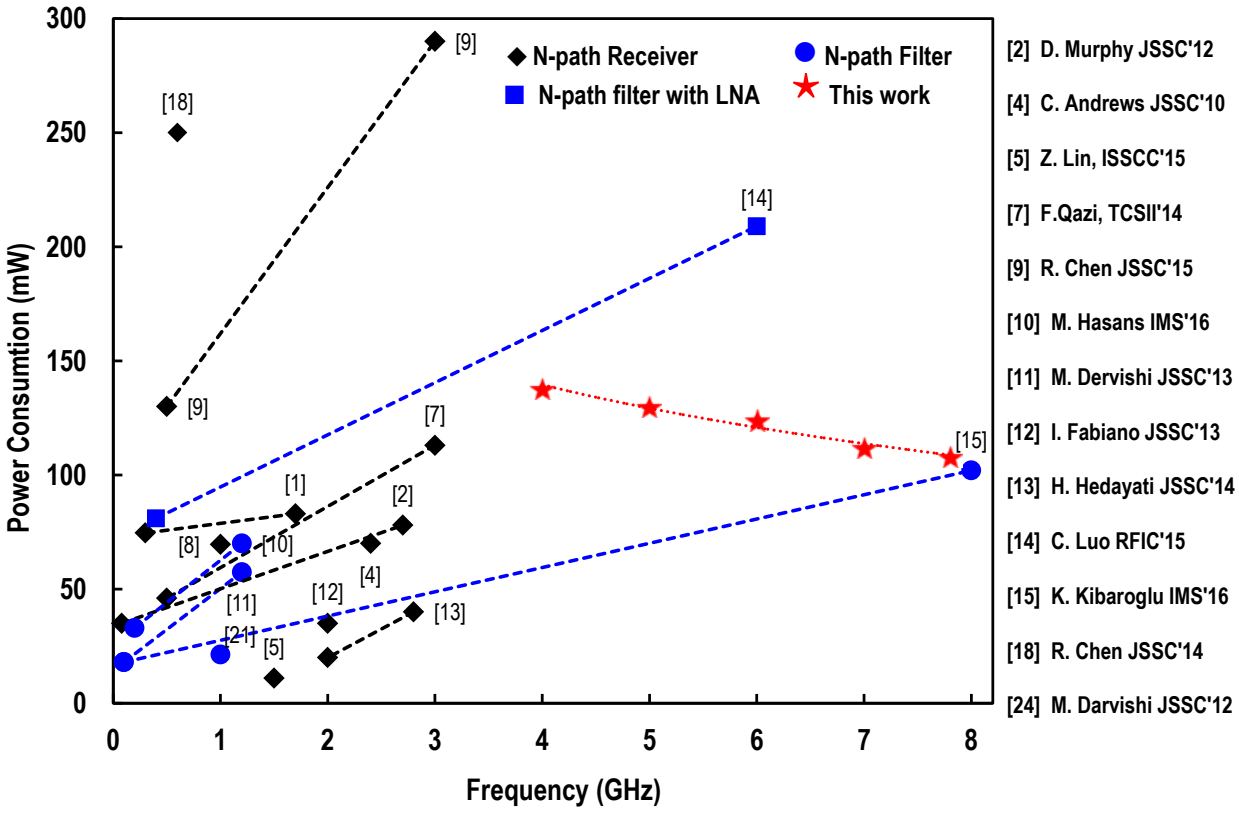

Figure 3-15: Power Consumption chart of integrated filters and receivers.

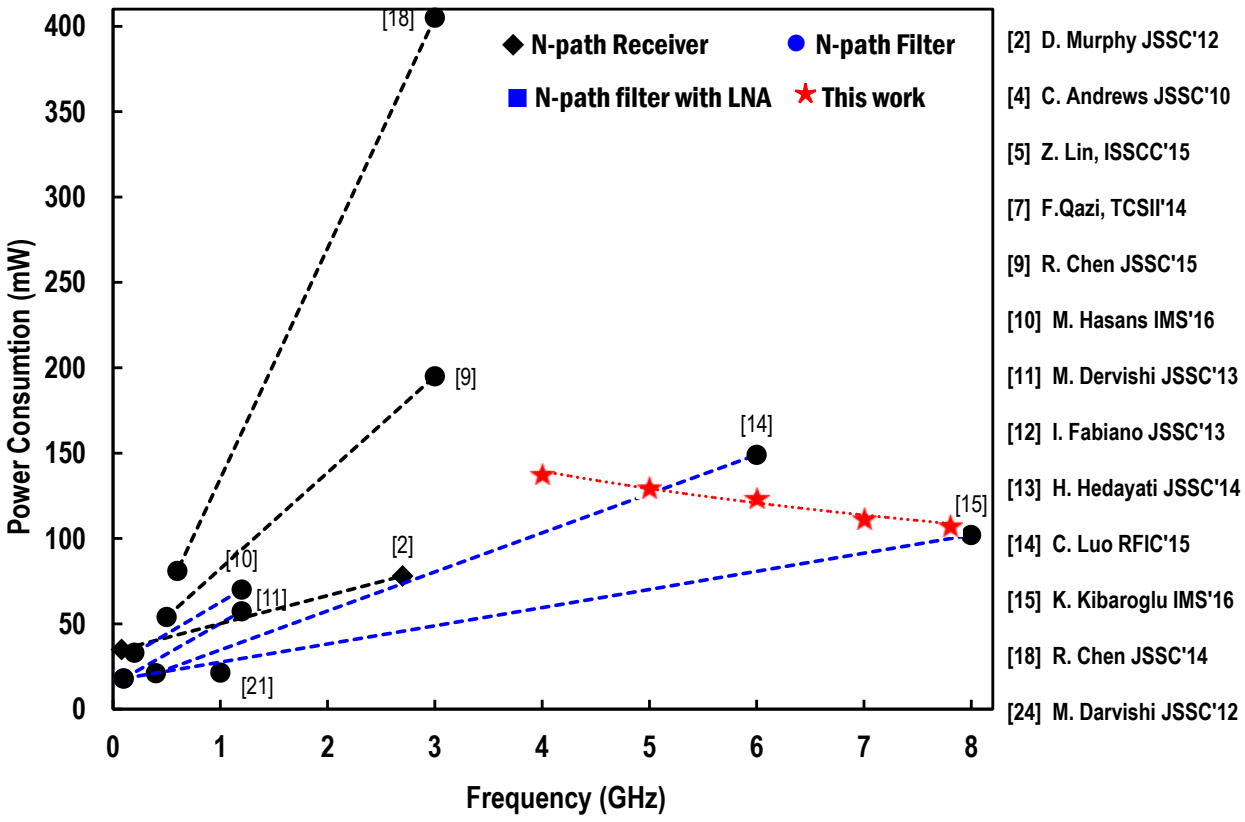

Figure 3-16: Power Consumption chart of filters only (filtering power consumption from the N-path receivers are reported).

3.5 Summary

A 4th-order Q-enhanced bandpass filter with 151-166 dB·Hz dynamic range, 2:1 center frequency tuning (4-8 GHz), and 2-to-25% fractional BW tuning has been demonstrated in 130 nm SiGe BiCMOS technology. The filter effectively synthesizes a 4th-order bandpass response by subtracting two identical 2nd-order LC-tanks responses with each tank resonance frequency optimally separated depending on the required passband ripple magnitude and bandwidth. The parallel synthetic 4th-order filter approach trades DC power to achieve a versatile filter design in terms of large fractional bandwidth tuning and center-frequency tuning at microwave bands. By migrating the architecture to advanced CMOS nodes with better f_T, 65 nm or below, power consumption can be reduced substantially due to the lower threshold voltage of the transistors. The concept can be easily extended to X, Ku and K bands with similar or lower DC power consumption, since on-chip inductor Q increases, thereby requiring less loss compensation; however, varactor losses need to be considered in the mm-wave regime.

Chapter Four: **Varactor Linearization**

4.1 Introduction

This chapter discusses in more detail the implementation of a proposed switched varactor control scheme to improve the linearity of the LC-tank. In Chapter 3, a switched four varactor architecture was implemented to improve the linearity of the LC-tank for a parallel synthetic 4^{th}-order BPF. In order to further study, the effectiveness of this scheme, the switched varactor control scheme is applied to a simple 2^{nd}- order BPF at C-band.

4.2 Varactor Nonlinearities and Modelling

4.2.1 Varactor Capacitance

A varactor is a variable capacitance, with certain maximum and minimum capacitance values, controlled using a bias voltage. The ratio of maximum and minimum capacitance is called the tuning ratio as discussed in section 2.3. This tuning ratio is around 4 for the “ncap” device from IBM SiGe 130nm BiCMOS 8HP technology used for this work. Generally, a large tuning ratio is preferred for wide frequency tuning range.

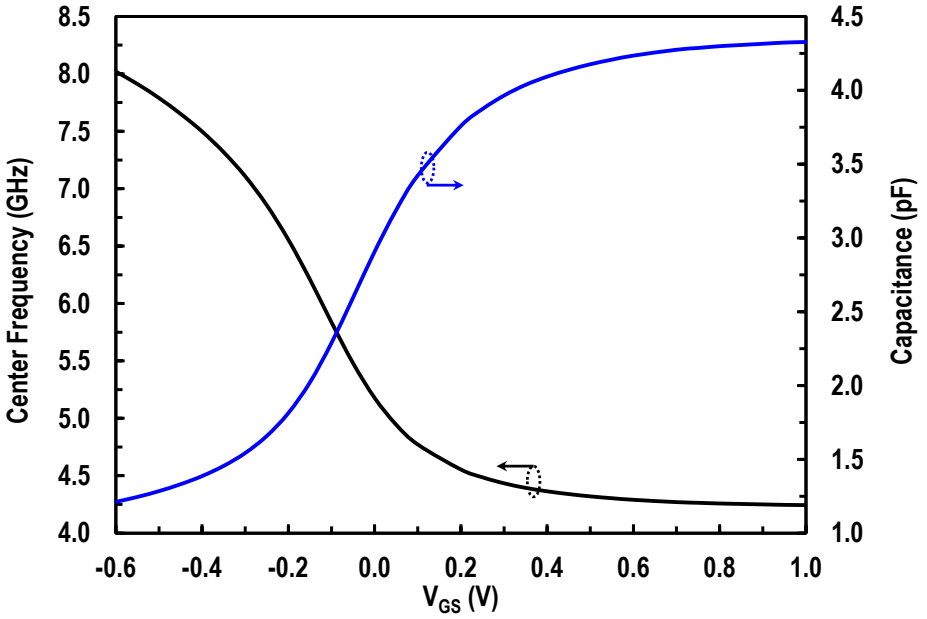

Figure 4-1: Varactor capacitance for a IBM 130 nm BiCMOS 8HP ncap device size of 1008/0.37 versus V_{GS} and the frequency range of the resonator for $L = 320pH$.

However, for a large tuning ratio varactor, on the order of more than two, the capacitance varies nonlinearly over applied voltage range and therefore limits the linearity performance of an LC tank used to implement a tunable BPF. Figure 4-1 shows the varactor capacitance curve versus the applied bias voltage V_{GS} for IBM 130nm BiCMOS 8HP "ncap" device of size of 1008/0.37 . The capacitance changes from 1.2–4.3 pF for an applied bias voltage of 1 to -0.5 V. The varactor capacitance can be modelled [58] approximately as

$$C(V_{GS}) = \frac{C_{max} + C_{min}}{2} + \frac{C_{max} - C_{min}}{2} tanh\left(a + \frac{V_{GS}}{V_0}\right) \quad (1)$$

where C_{max} and C_{min} are the maximum and minimum values of capacitance range, and a and V_0 are constants that represent the intercept and slope to match the simulated plotof the C-V characteristic. A plot of (1) is compared to the C-V curve of a simulated IBM SiGe 130 nm varactor in Figure 4-2. The theoretical approximation is very close the actual device simulation. A more accurate approximation can be derived from charge using $d(Q) = C(V)dV$ relation, yielding

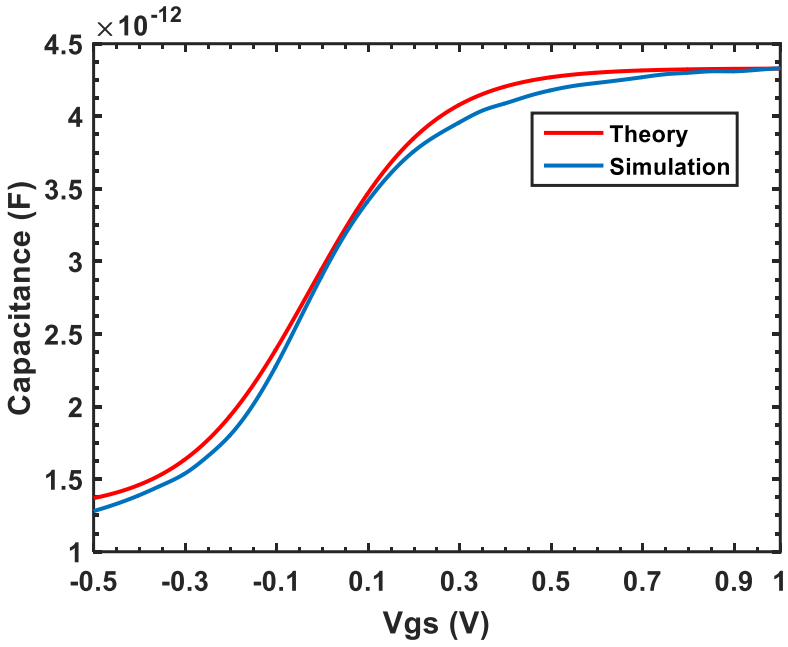

Figure 4-2: Varactor capacitance theory (1) and simulated range for IBM SiGe 130nm.

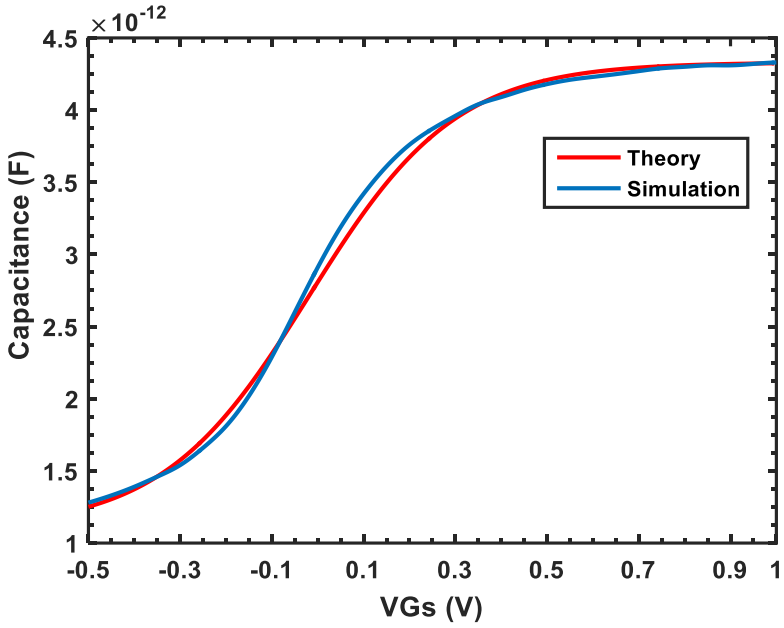

Figure 4-3: Varactor capacitance theory (3) and simulated range for IBM SiGe 130nm.

$$Q(V_{GS}) = \int C(V_{GS})\, dV_{GS} = \int \frac{C_{max} + C_{min}}{2} + \frac{C_{max} - C_{min}}{2} tanh\left(a + \frac{V_{GS}}{V_0}\right) \quad (2)$$

$$Q(V_{GS}) = \frac{C_{max} - C_{min}}{2} V_0 \ln\left[\cosh\left(a + \frac{V_{GS}}{V_0}\right)\right] + \frac{C_{max} + C_{min}}{2} V_{GS} \quad (3)$$

The current through the capacitor can then be calculated

$$I = \frac{dQ(V_{GS})}{dt} \quad (4)$$

Using (4), the capacitance plot together with the actual varactor device is shown in Figure 4-3 which represents a closer approximation.

4.2.2 Varactor Nonlinearity

As can be seen, the actual device and the model equations exhibit a large nonlinear capacitance especially in the transition region as shown in Figure 4-2 and Figure 4-3. This can also be explained intuitively as shown in Figure 5 4, where a small voltage swing across the varactor terminal causes a large capacitance variation. Therefore, nonlinear capacitance is an inherent behavior with large tuning ratio varactors. The varactor nonlinear capacitance can be approximated using power series as follows

$$C_{var}(V_{GS}) = C_0 + C_1 V_{GS} + C_2 V_{GS}^2 \quad (5)$$

Where C_0 is the linear capacitance and

$$C_1 = \frac{dC_{var}}{dV_{GS}} \quad , \quad C_2 = \frac{1}{2}\frac{d^2 C_{var}}{dV_{GS}^2}$$

The nonlinear current is then given by

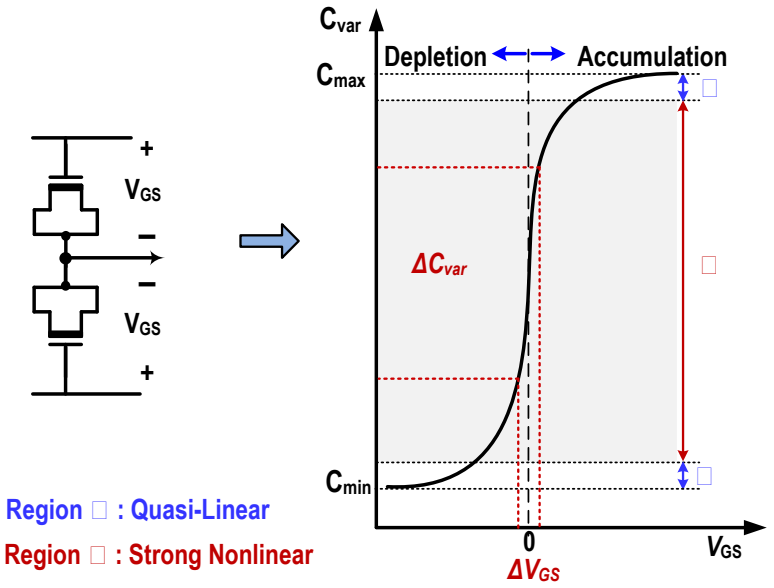

Figure 4-4: Depiction of varactor capacitance variation in strong nonlinear region for a small voltage swing across its terminals.

$$i_{var}(V_{GS}) = \frac{dQ_{var}}{dt} = C_{var}(V_{GS})\frac{dV_{GS}}{dt} \tag{6}$$

$$i_{var}(V_{GS}) = C_1\frac{dV_{GS}}{dt} + \frac{1}{2}C_2\frac{dV_{GS}^2}{dt^2} + \frac{1}{3}C_3\frac{dV_{GS}^3}{d3}\ . \tag{7}$$

From (1), C_1 can be written as

$$C_1(V_{GS}) = \frac{dC(V_{GS})}{dV_{GS}} = \frac{C_{max} - C_{min}}{2} sech^2\left(a + \frac{V_{GS}}{V_0}\right).\frac{1}{V_0} \tag{8}$$

$$= \frac{C_{max} - C_{min}}{2}.\frac{1}{V_0}\left[1 - tanh^2\left(a + \frac{V_{GS}}{V_0}\right)\right] \tag{9}$$

$$C_2(V_{GS}) = \frac{dC_1(V_{GS})}{dV_{GS}} = -\frac{C_{max} - C_{min}}{2}.\frac{2}{V_0} tanh\left(a + \frac{V_{GS}}{V_0}\right) sech^2\left(a + \frac{V_{GS}}{V_0}\right).\frac{1}{V_0} \tag{10}$$

$$= -\frac{C_{max} - C_{min}}{2}.\frac{2}{V_0^2} tanh\left(a + \frac{V_{GS}}{V_0}\right) sech^2\left(a + \frac{V_{GS}}{V_0}\right) \tag{11}$$

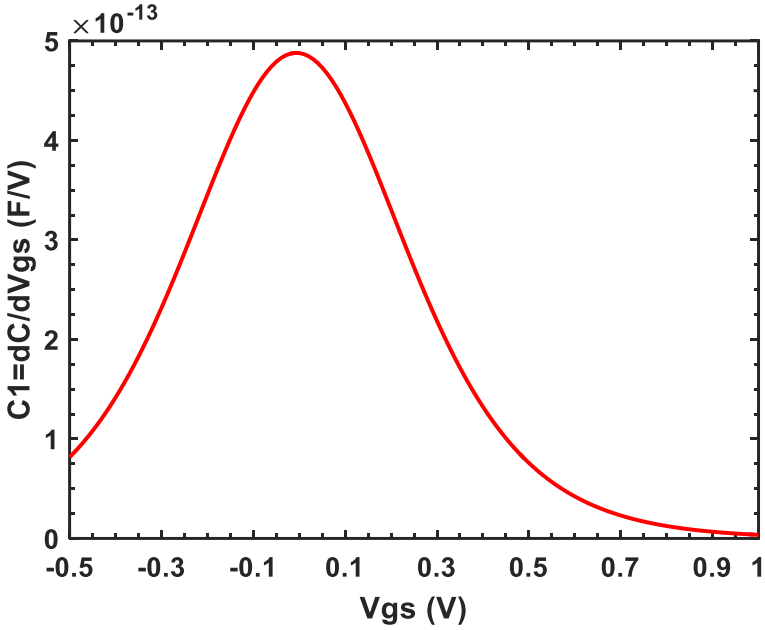

(a)

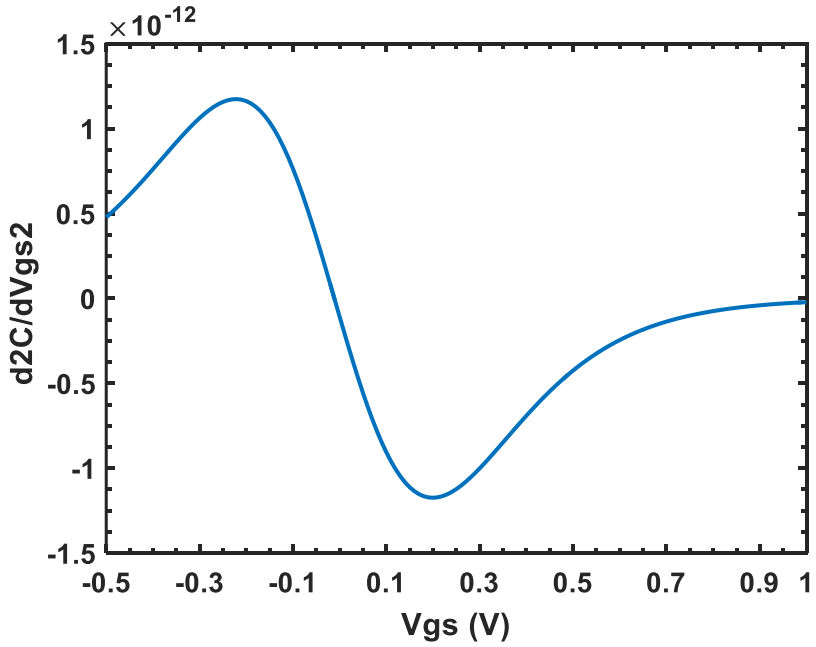

(b)

Figure 4-5: (a)Varactor nonlinear capacitance components C_1 theory (9) and (b) Varactor nonlinear capacitance components C_2 theory (11).

The plots of nonlinear components C_1 and C_2 of the varactor capacitance are shown in Figure 4-5 (a) and Figure 4-5 (b) respectively. Using the power series, (5), the nonlinearities of the varactor used in an LC-tank can be expressed in term of P_{-1dB} as follows [51]

$$V_{P1dB}^2 = \frac{0.435}{Q}\frac{C}{C_2} \quad , Q = \frac{R_C}{\sqrt{L/C}} \tag{12}$$

Using Volterra series, the P_{-1dB} can be derived as [51]

$$V_{P1dB}^2 = \frac{0.435}{Q}\frac{C}{C_2}\left[\left|1 - \frac{2}{3}\frac{C_1^2}{C C_2}\right|\right]^{-1} \tag{13}$$

Figure 4-6(a) shows the plot of P_{-1dB} theory using Volterra series (13). The corresponding simulated P_{-1dB} of an IBM 8HP varactor device, in an LC-tank for L=320 pH, is also shown in Figure 4-6 (b). part from the center-frequency shift of the point where nonlinear component C_2 becomes zero (Figure 4-5 (b)) making the P_{-1dB} very large, the two plots show a very similar trend.

4.3 Varactor Linearization

4.3.1 Switched Varactor scheme

As discussed in section 2.3, switched varactor control scheme improves the linearity of the varactor which in turn makes the tunable BPF more linear. The basic idea is to divide the single large tuning ratio varactor into N number of smaller varactors. This breaks the frequency range of a single varactor into N discrete frequency steps. N-1 varactors are biased in switched mode between maximum and minimum capacitance values and the Nth varactor is biased to vary continuously to cover the frequency range between the frequency step size. In this way, the strong nonlinear capacitance region (Figure 4-4) of a single large varactor is divided by N. This reduces the nonlinear capacitance variation ΔC_{var} significantly (by a factor of ~N) as shown in Figure 4-7.

Figure 4-8 shows varactor control schemes with single, 4, 8 and 16 switched control steps. The associated simulated linearity in terms of P_{-1dB} is also plotted when the

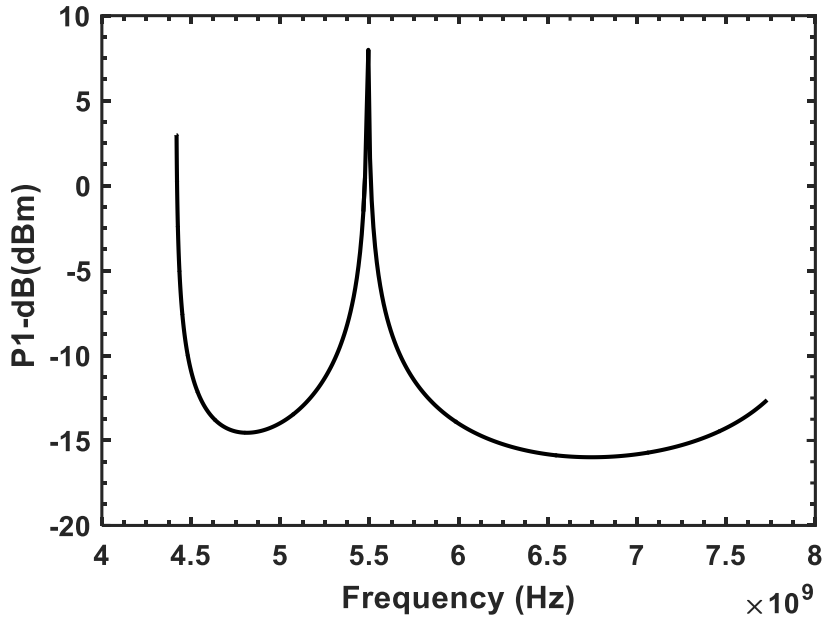

(a)

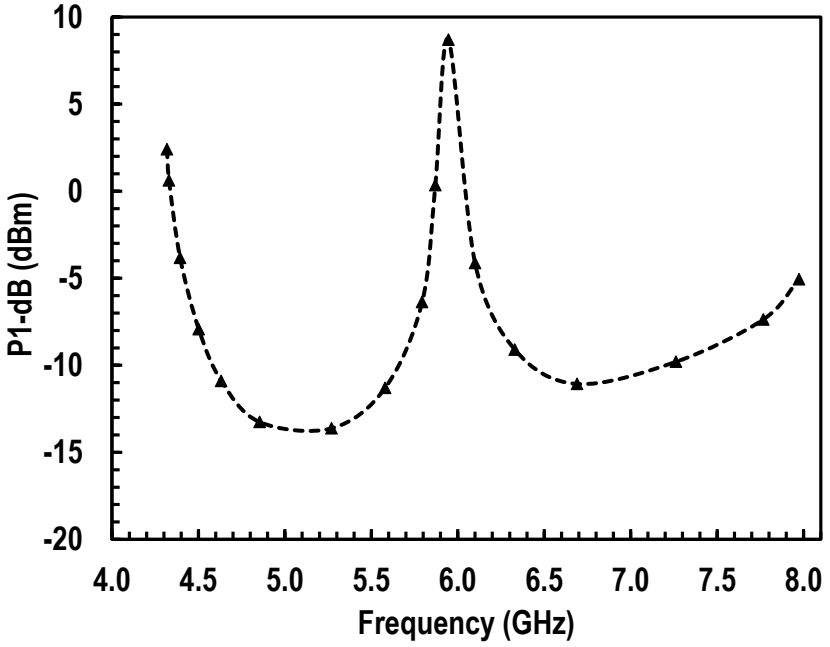

(b)

Figure 4-6: (a) Varactor nonlinearity in terms of P_{-1dB} theory (1) using Volterra series and (b) Varactor nonlinearity in terms of P_{-1dB} for IBM SiGe 130nm single-ended device.

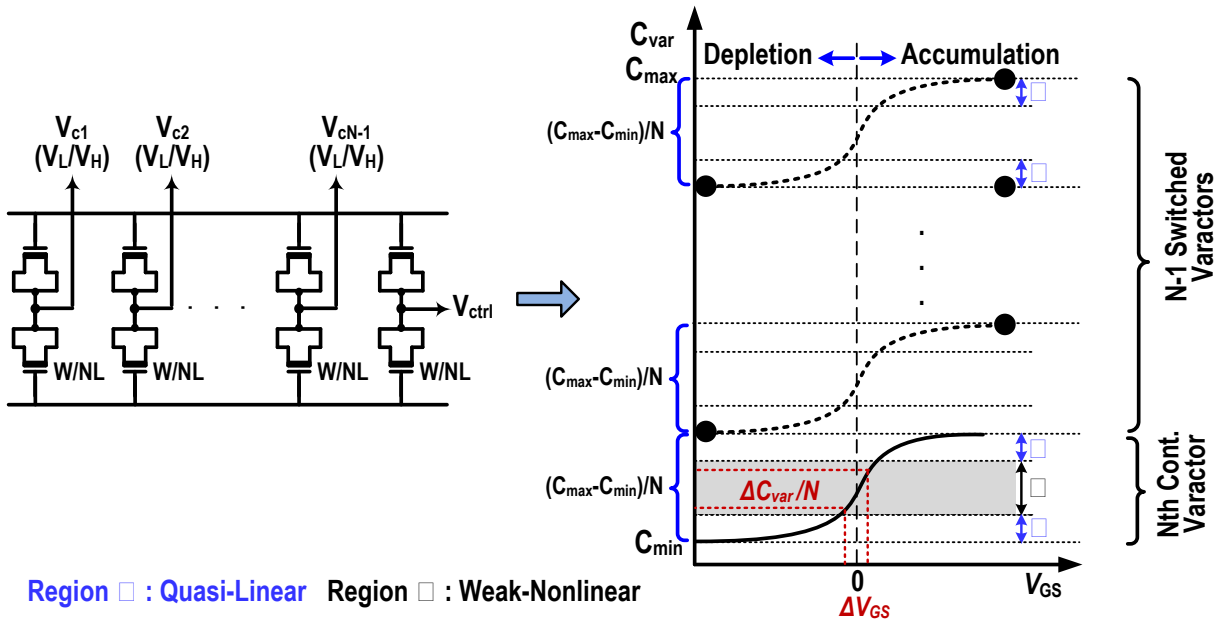

Figure 4-7: Depiction of N switched varactor control scheme to reduce the non-linear capacitance variation by N making it weakly nonlinear.

varactors are excited in differential mode with an inductor. From the P_{-1dB} plots, it is evident that increasing the number of controls steps makes the varactor structure more linear overall, and the upper and lower P_{-1dB} difference becomes smaller and smaller. However, increasing the number of controls steps makes the layout of smaller varactors and their individual bias voltage control complicated. This also increases the effective area of the tank nodes. This in turn increases the associated parasitic, i.e. resistance and capacitance, which degrades the Q and reduces the varactor tuning frequency range. Therefore, a compromise is needed between increasing the number of varactors, N, and layout complexity degrading the Q and tuning range. From simulation, including efficient layout, an optimized N value is around 8 to 12. In this chapter, an eight switched varactor scheme was implemented.

4.3.2 Circuit Design

Figure 4-9 shows the schematic diagram of the 2nd-order BPF with an eight switched varactor scheme. For the switched varactor control practical implementation, digital

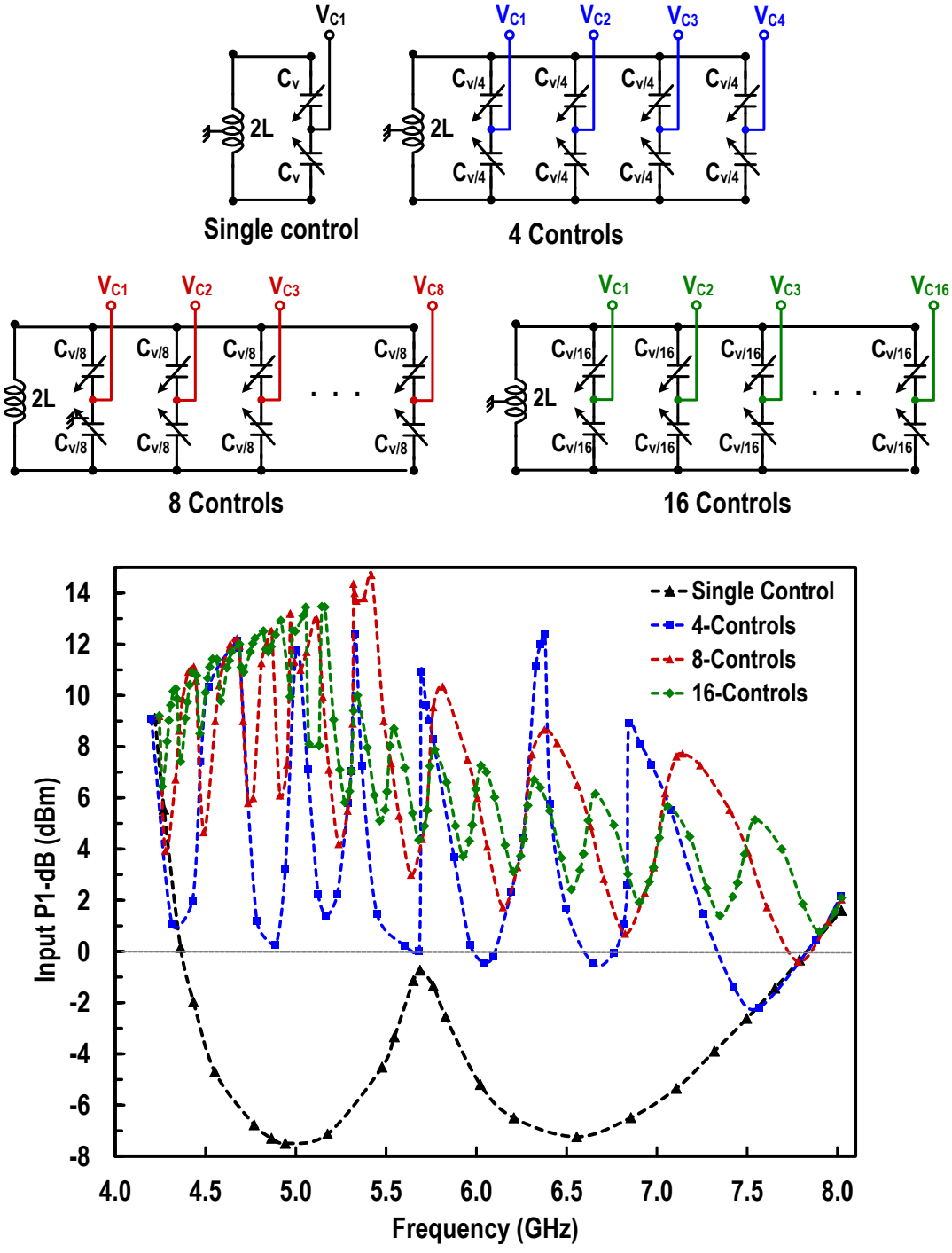

Figure 4-8: Switched varactor control (single, 4, 8 and 16) schemes and corresponding simulated P_{-1dB}.

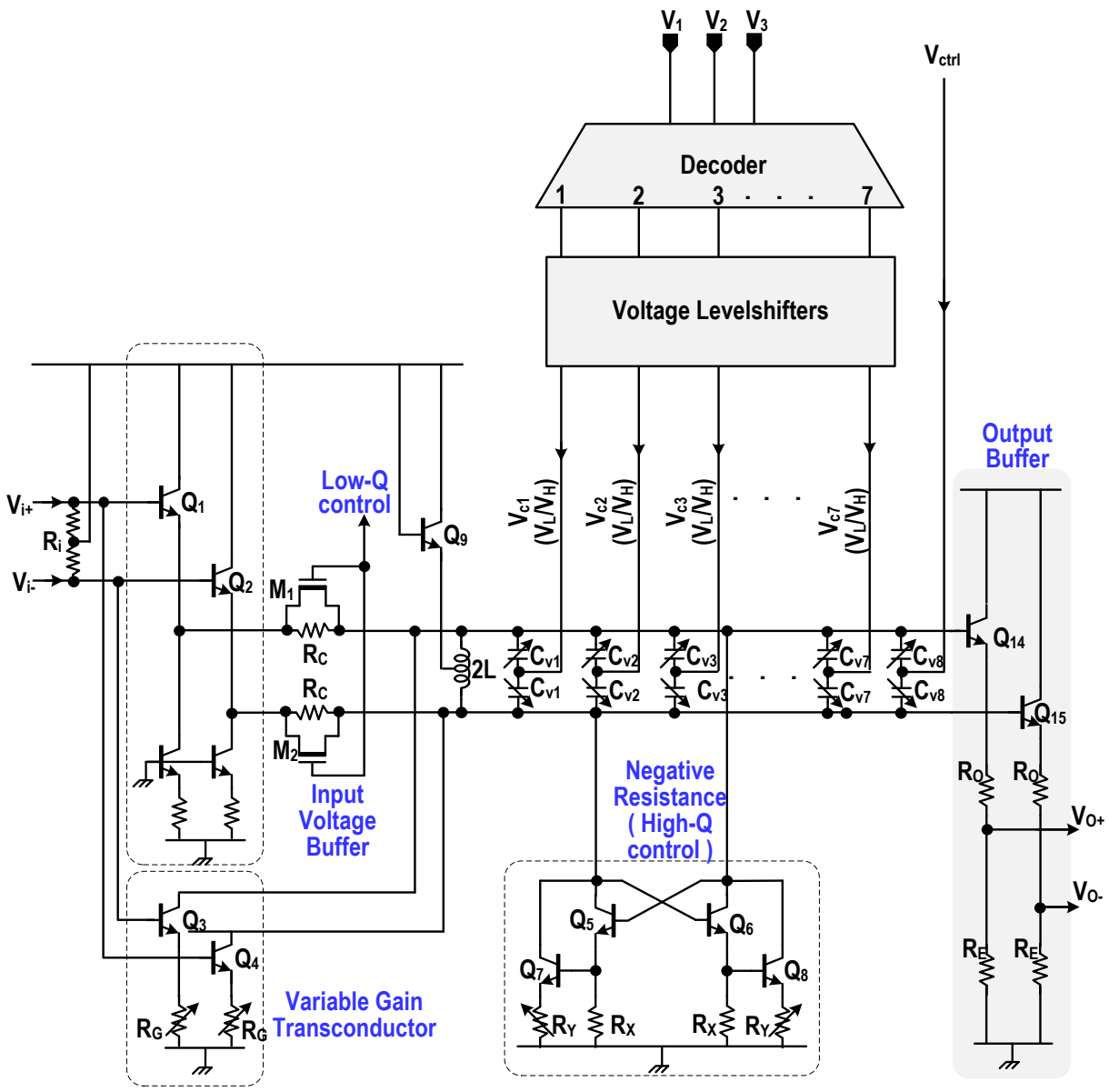

Figure 4-9: Block Diagram of the BPF with proposed varactor linearization scheme.

logic control is needed. Digital logic usually switches between 0 V and Vdd and this voltage swing is not compatible with the varactors available in the 130 nm CMOS technology used. Therefore, level-shifters are needed to drive the individual varactors with the proper bias voltage between the lower capacitance voltage of 1.6 V and the upper capacitance voltage of 3.2V. These voltage values depend on the circuit biasing where varactor is used in the circuit. , e.g., in this design the varactor gate bias node is set at 2.6 V set by the diode connected transistor Q_9 from a supply voltage of 3.5 V. The rest of the circuit design is similar as discussed in section 3.3, including a negative gm cell consisting of transistors $Q_{5,6,}$ $Q_{7,8}$ and resistors R_X-R_Y, a voltage and a current driving scheme, and R_C variable resistance for low Q control. The output driving circuit is a buffer which consists of $Q_{14,15}$ and R_0 to drive the 50 Ω output load of the measurement equipment.

The BPF with switched control scheme (Figure 4-9) is implemented in IBM 130nm SiGe BiCMOS technology. The real challenge in the proposed switched varactor control scheme is the LC-tank layout. Since the varactor is divided into N (8 in this case) smaller independent varactors, their biasing needs to be separated. This introduces N extra LC-tank nodes on the biased sides of the varactors and increases the node length at the other side of the varactor. This is shown in Figure 4-10 where single and 8 control varactor Q sensitive LC-tank nodes are highlighted in red. The chip micrograph is shown in Figure 4-11 with the varactor control scheme layout in inset. An efficient layout was performed to reduce the Q sensitive node length and to minimize the Q degradation due to layout parasitics. A Q degradation of only 7~9% was achieved after post layout simulations.

4.3.3 Level-shifter and decoder

The CMOS logic voltage levels in 130nm BiCMOS technology are 0 and 1.8 V. The recommended varactor bias control voltage V_{GS} ranges from 1V to -0.6 V to vary the capacitance from maximum to minimum value. The bias point across the differential varactor is around 2.6 V, set by the biasing transistor Q_9 as shown in Figure 4-9. So the varactor bias voltage has to be between 3.2 V and 1.6 V. For this purpose, level shifters are needed to properly shift the digital logic voltages to be compatible with the varactor biasing. The required level-shifter output is achieved with a logic Vdd=1.6V. The voltage level-shifter schematic, which

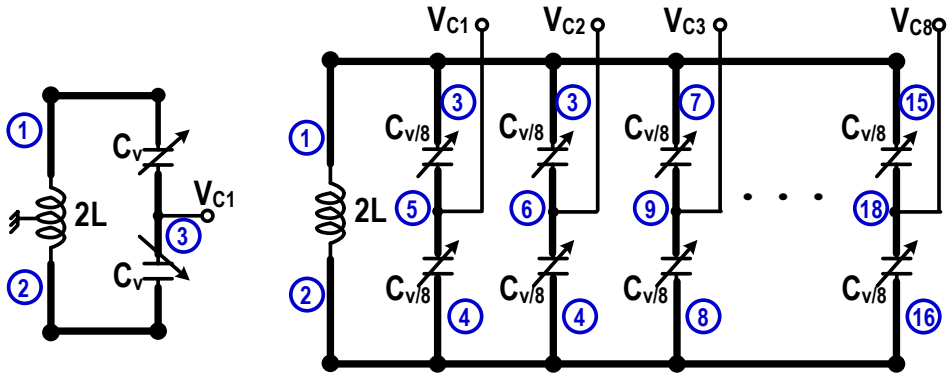

Figure 4-10: Single versus 8 switched control schemes highlighting the Q sensitive LC tank nodes.

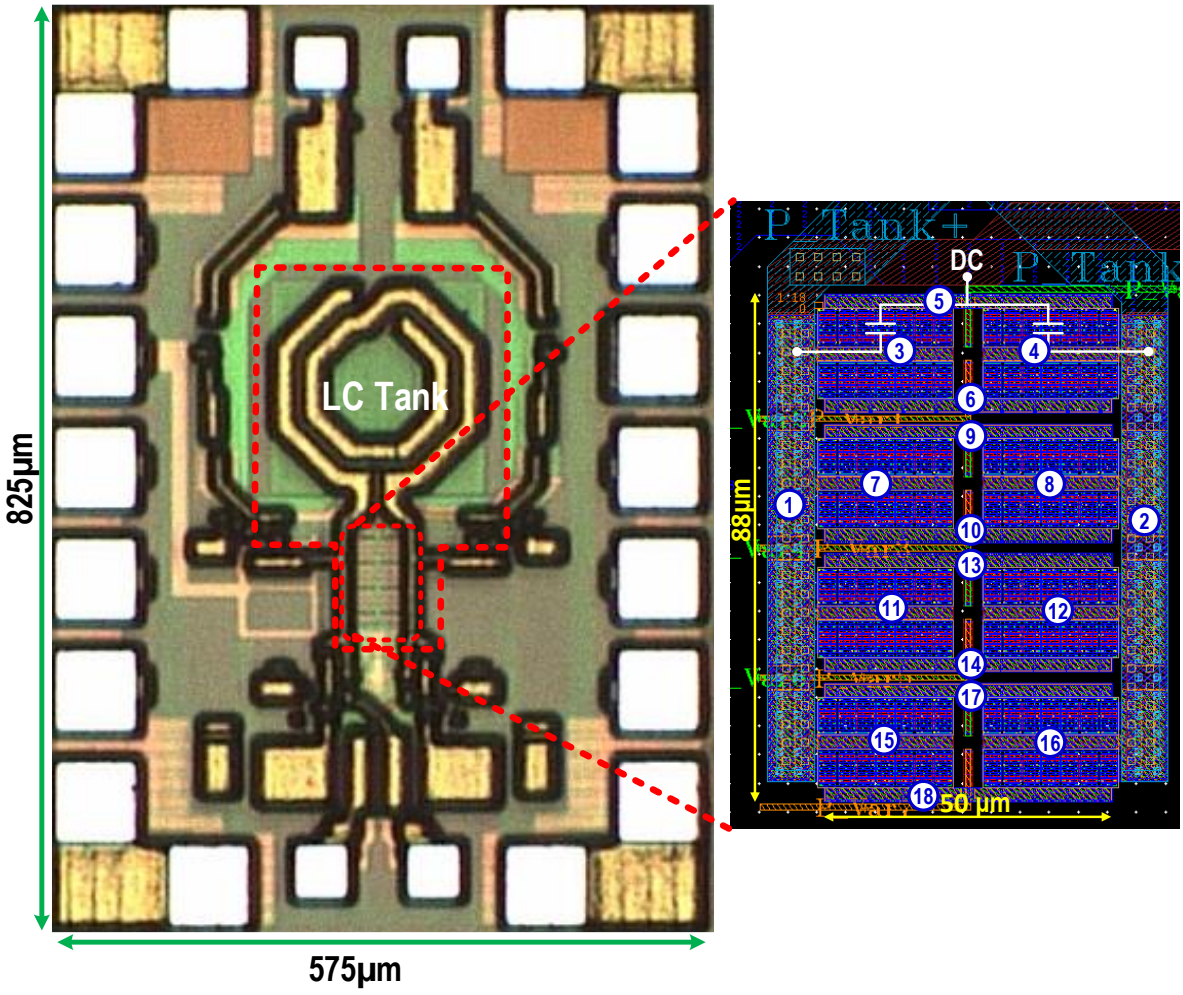

Figure 4-11: Micrograph of the 825x575 µm^2 chip in IBM 8HP with switched varactors and 8-control layout.

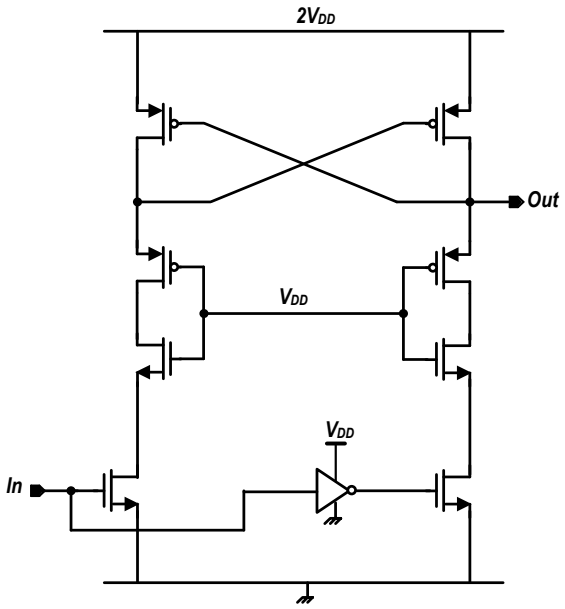

Figure 4-12: Schematic of the voltage level-shifter to drive the varactor in switched mode.

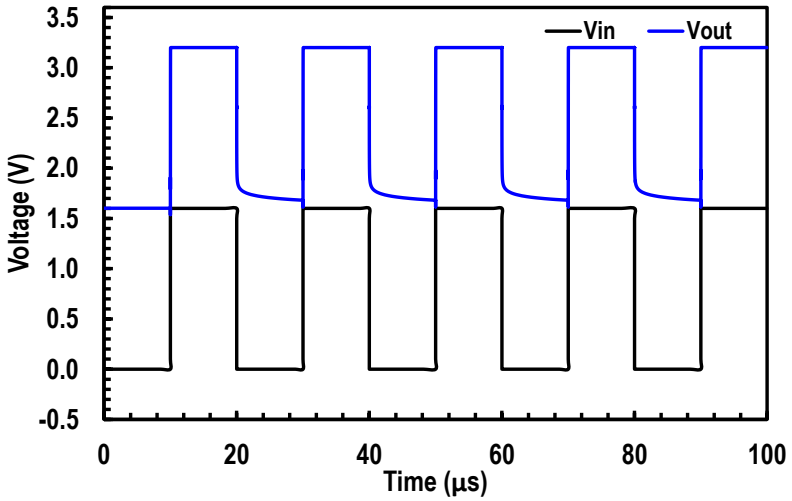

Figure 4-13: Simulation results of the voltage level-shifter.

converts a Vdd-0 voltage swing to 2Vdd-Vdd voltage swing, is shown in Figure 4-12. The simulated level-shifter input and outputs are plotted in Figure 4-13. A total of seven level shifters are used for the switched control varactors. The 8th varactor is operated in continuous tuning mode and is controlled directly. The inputs to the level shifters originate from the logic decoder, which decodes the three-bit input B1-B3 to a seven-bit output, switching to logic 1 in increasing fashion depending on the input code. The truth table of this decoding logic is shown in Table 4-1. The reduced decoder logic is the shown in Figure 4-14 which generates the seven outputs depending on the input code.

Table 4-1: Truth Table of Switched Varactor Control Logic.

B_1	B_2	B_3	V_{C1}	V_{C2}	V_{C3}	V_{C4}	V_{C5}	V_{C6}	V_{C7}
0	0	0	0	0	0	0	0	0	0
0	0	1	0	0	0	0	0	0	1
0	1	0	0	0	0	0	0	1	1
0	1	1	0	0	0	0	1	1	1
1	0	0	0	0	0	1	1	1	1
1	0	1	0	0	1	1	1	1	1
1	1	0	0	1	1	1	1	1	1
1	1	1	1	1	1	1	1	1	1

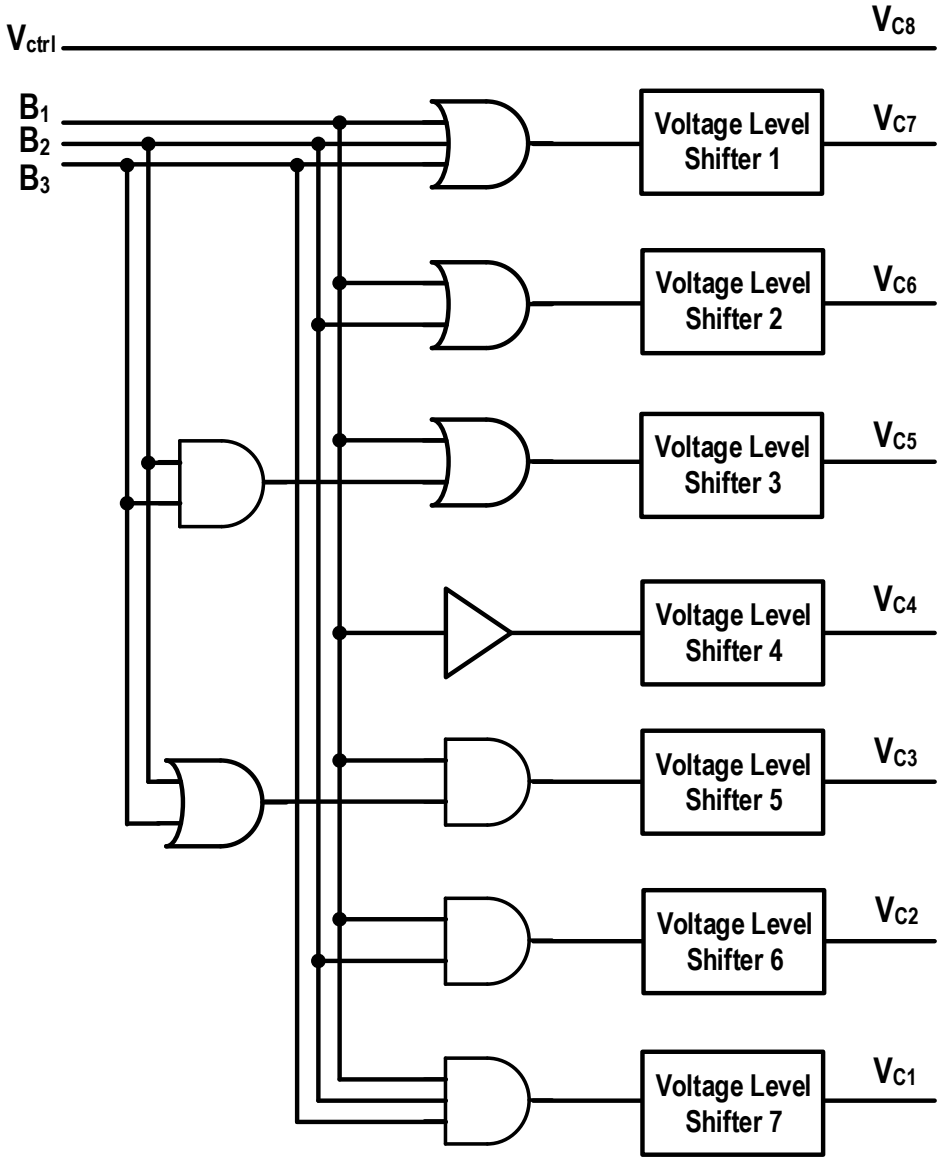

Figure 4-14: Schematic of the decoder for switched mode control

4.3.4 Measurement Results

Figure 4-15 shows the circuit diagram enabled for the non-linearity characterization. The gain stage comprising transistor $Q_{3,4}$ and resistor R_G is turned off by maximizing the resistance R_G. The second stage of negative transconductance comprising $Q_{7,8}$ and R_Y is also turned off. The purpose is to minimize the non-linear contribution from the gain and negative transconductance stages. The measured BPF output is plotted in Figure 4-16 with frequency tuning from 4.15 to 7.61 GHz. The Q varies from 12 to 32 as shown in Figure 4-17. The measured P_{-1dB} is plotted in Figure 4-18 for frequency range of 4.15 to 7.61 GHz. The measured P_{-1dB} is from 8.2 dBm to 3.8 dBm which shows significant linearity improvement due to switched varactor control scheme compared to the single varactor linearity in Figure 4-8.

4.4 Summary

The switched varactor control technique implemented in this work greatly improves the linearity of Q-enhanced LC BPF. The proposed scheme is also suitable for more practical digital control. By dividing the large varactor into eight smaller varactors, the sensitivity of the center frequency to control voltage is also improved since the same bias range is now used to tune a smaller varactor with reduced minimum to maximum capacitance range.

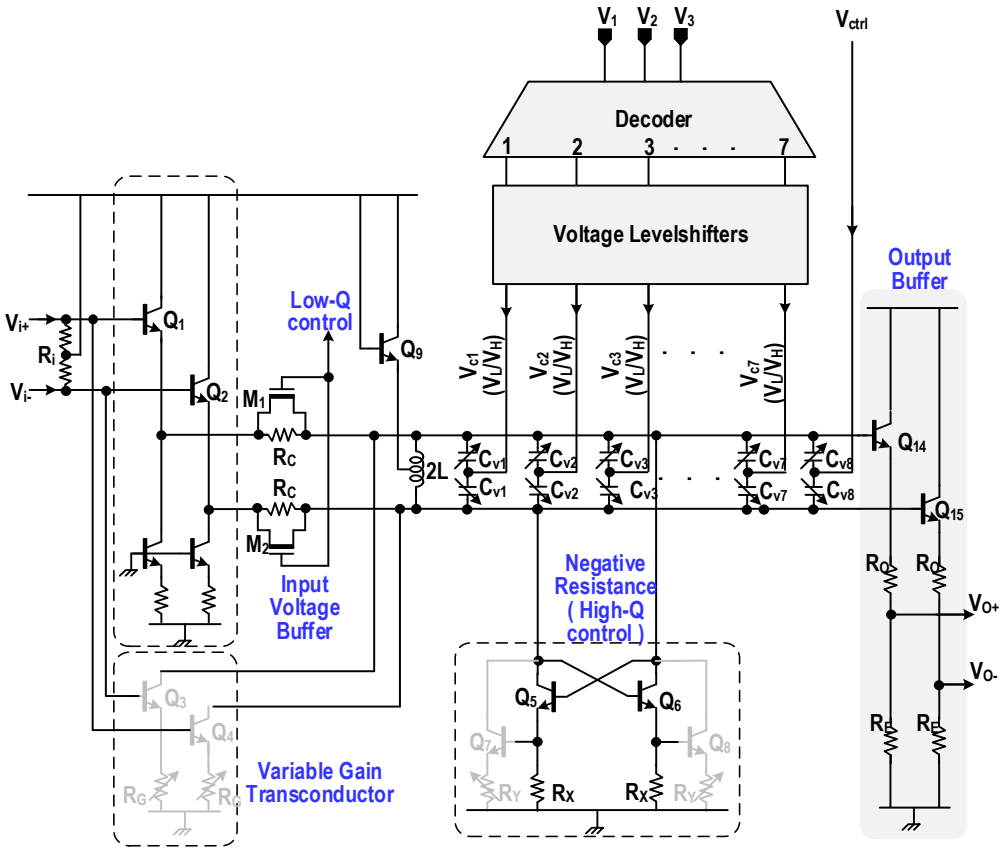

Figure 4-15: Schematic showing enabled circuit for the measurement.

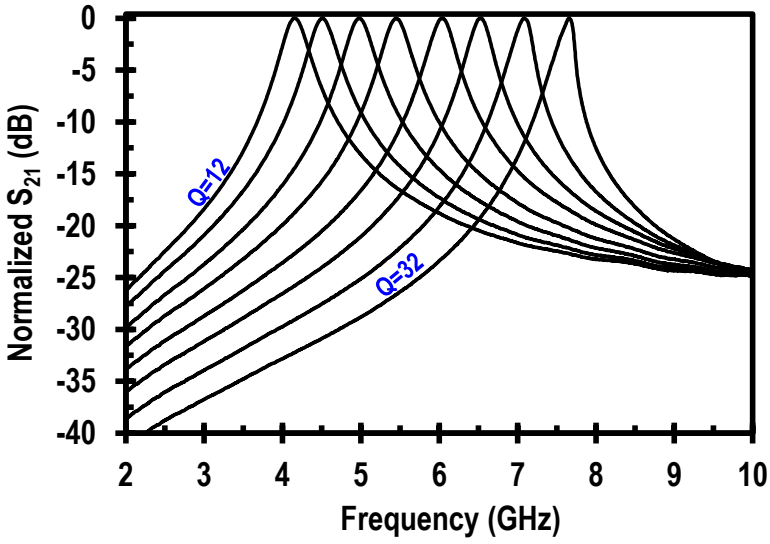

Figure 4-16: Measurements of BPF filter with 8-switched varactor control scheme.

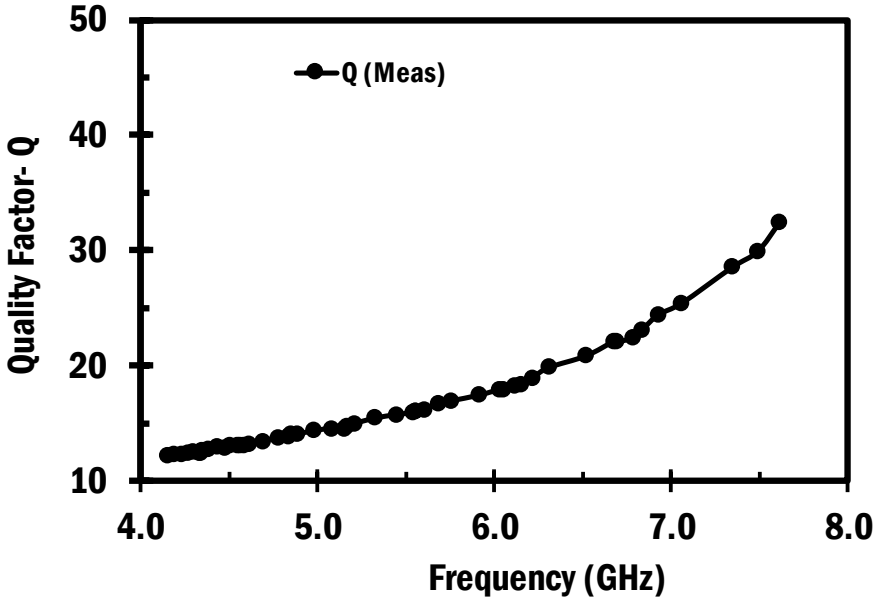

Figure 4-17: Measured Q from 4.15 to 7.61 GHz.

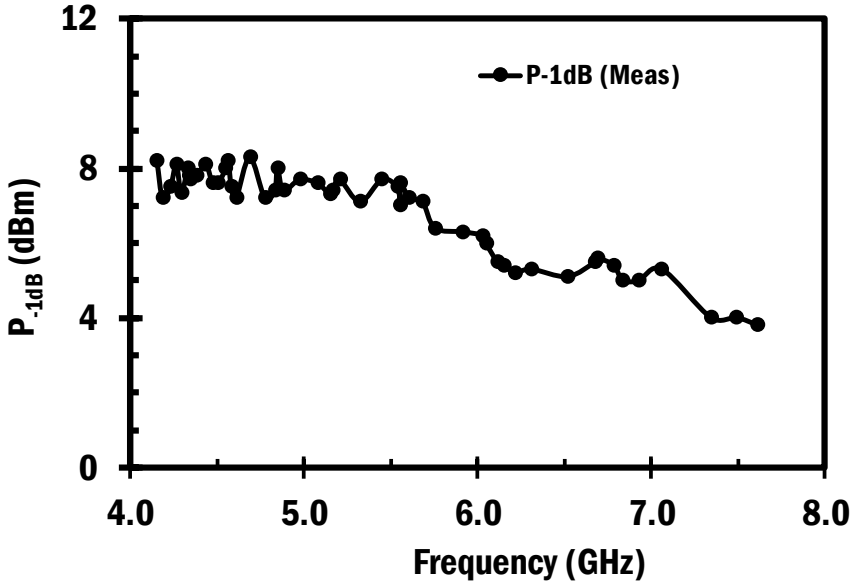

Figure 4-18: Measured P_{-1dB} of BPF filter with 8-switched varactor control scheme.

Chapter Five: **Tunable Dual-band Microwave BPF**

5.1 Introduction

Modern wireless communication and radar systems require simultaneous operation of more than one band for multi-standard or multi-band RF front-ends that can operate in the presence of strong interference. This requirement is due to rapid increase of various systems and standards co-existing in the same spectrum. More specifically, this requirement can arise from the need to support two largely spaced frequency bands, or from carrier aggregation where information is spread over non-contiguous bands to make efficient use of the spectrum. One common example of such system is the WiFi standard operating at 2.4 and 5.8 GHz. To increase the data rate and for reliable communication, a front-end is needed which can simultaneously support the two bands. As a result, there is a significant interest in multi-band bandpass filters, particularly dual-band filters. Additionally, future communication standards are shifting towards higher frequencies, in the range of microwave to millimeter-wave.

Conventionally, dual-band filters in the microwave regime have been designed using substrate integrated waveguide (SIW) cavities and/or microstrip lines [52–58] which are not practical to integrate on chip. These solutions also typically lack tuning capabilities, and therefore multiple switched filters are needed to cover different frequency bands. Numerous off-chip techniques to

obtain dual-band response have been proposed in [52, 54–58] including stepped impedance resonators, capacitively loaded dual cavity resonators, and microstrip based coupled resonating sections. An off-chip passive tunable multiband bandpass filter (BPF) covering 0.8-1.2 GHz, employing Wilkinson type power divider [53], has also been reported with good performance but with limited integration capability and large area. To date, no work has been reported for on-chip dual-band operation at higher microwave frequencies above 3 GHz.

Recent developments in on-chip filtering, including N-path filters, are discussed in chapter 1. N-path filters typically employ a wideband LNA followed by a narrowband frequency tunable filtering using switches driven by multi-phase clocks. For simultaneous dual-band operation, the N-path filters will need two sets of N-phases clocks at each of the two desired center frequencies which will increase the power consumption substantially, and their filtering performance degrades as frequency increases. For example, in [25], at the expense of significant power consumption the OOB attenuation is still limited to 20 dB or worse at frequencies above 10 GHz in CMOS SOI 32nm.

Compared to N-path filters, Q-enhanced LC filtering is quite suitable at higher microwave frequencies due to increased on-chip inductor Q's and reduced size [33, 35] and is also suitable for dual-band operations with increased OOB attenuation. In this chapter, an on-chip Q-enhanced dual-band filtering solution is presented along with measured results for X and Ku band frequencies.

5.2 Dual-band synthesis Concept

Figure 5-1 shows the concept of parallel synthesis techniques using two LC-tanks with the tank frequencies spaced farther apart. The center frequencies of the LC-tanks are tunable using the varactors C. The Q of the LC-tank can be tuned using a variable load resistance R_P . By exploiting the LC-tank's phase characteristics, two types of dual-band band-pass shaping are achievable. The first characteristic is achieved by subtracting the two LC-tank responses with largely spaced center frequencies ω_{01} and ω_{02} to form a dual-band filter response with higher out-of-band attenuations. However between bands the attenuation is 6 dB less compared to the 2nd-order BPF responses

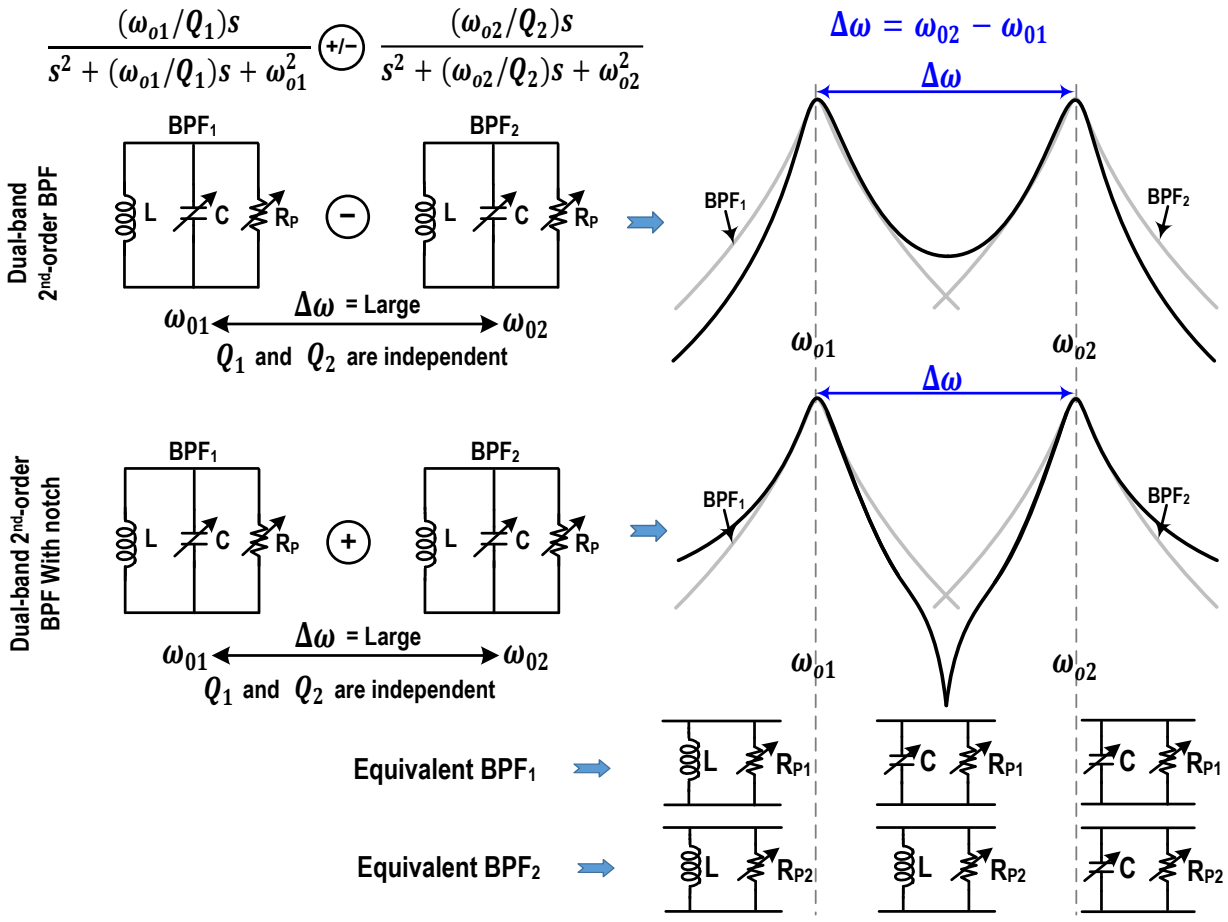

Figure 5-1: Shaping of dual-bands BPF responses by parallel synthesis of two tunable (Q and center-frequency) LC-tanks.

alone. This can be explained by the phase changes of the two LC-tanks where both LC-tanks are inductive below the center frequency ω_{01} of BPF1 and therefore are in phase. When the responses are subtracted in this region the resulting roll-off will be steeper than the 2nd–order BPFs alone. The same is true for the region higher than the center frequency ω_{02} of BPF2. In between the two center frequencies ω_{01} and ω_{02}, BPF1 is capacitive whereas BPF2 is inductive; hence they are out-of-phase resulting in addition of the responses when the outputs are subtracted. The second characteristic is achieved by adding the two LC-tank responses. This results in a sharp notch between the two center frequencies for higher attenuation between the bands. However, the ultimate rejection levels on the higher and lower sides of the center frequency worsen by 6 dB compared with individual 2nd-order BPF responses due to additive common impedance by the two BPFs. The choice of addition or subtraction to form dual-band responses depends on the application and operating frequencies; nevertheless, a trade-off exists between inband attenuation vs. OOB attenuation. The addition mode resulting in the deeper notch may be desirable at lower RF frequencies where an attenuation in-between the bands is important. The subtraction mode is favorable, in general, at higher microwave frequencies where the band separations are larger.

5.2.1 Dual-band attenuation theory and simulations

To find the attenuation in-between bands, the 2nd-order transfer function can be expressed as

$$H(s) = \frac{\left(\frac{\omega_{01}}{Q_1}\right)s}{s^2 + \frac{\omega_{01}}{Q_1}s + \omega_{01}^2} \tag{1}$$

$$H(j\omega) = \frac{1}{1 + jQ\left(\frac{\omega}{\omega_0} - \frac{\omega_0}{\omega}\right)} \tag{2}$$

For large Q, (2) can be expressed as

$$|H(j\omega)| \approx \frac{1}{Q\left(\frac{\omega}{\omega_0} - \frac{\omega_0}{\omega}\right)} \tag{3}$$

To find attenuation between bands by the first BPF, $\omega_0 = \omega_{01}$ and $\omega = \omega_{01} + \frac{\Delta\omega}{2}$ are substituted, and after approximation, (3) can be expressed as

$$|H(j\omega)| \approx \frac{1}{2Q}.\left(\frac{\omega_{02}+\omega_{01}}{\omega_{02}-\omega_{01}}\right) \quad (4)$$

Therefore, for the same Q of each band, the total attenuation between bands will be added and can be expressed in dB as

$$A_T = 20\log\left(\frac{1}{2Q}.\frac{\omega_{02}+\omega_{01}}{\omega_{02}-\omega_{01}}\right) + 6 \ \ (dB) \quad (5)$$

where ω_{01} and ω_{02} are the center frequencies of LC-tanks. This shows that the in-between bands attenuation is degraded by 6 dB compared to a 2nd-order BPF response.

Figure 5-2(a) shows the simulation and the approximate relation derived in (5) against the frequency spacing between the two bands in terms of the ratio of ω_{02} to ω_{01}. In this case the Q of each BPF is 50 and the spacing between the two bands are varied from very small to when ω_{02} is twice that of ω_{01}. The plots show agreement between the simulation and the theoretical approximation. The relation in (5) can reveal important design parameters in terms of Q and spacing between the two bands to achieve a targeted attenuation. For example, when Q of both bands is set to 50, the spacing resulting in ω_{02} = 1:5ω_{01} guarantees at least 20 dB of attenuation.

Figure 5-2(b) shows the plots of the theoretical equation and simulation vs. Q of the two bands for two cases of ω_{02} and ω_{01} spacing. For Q = 100 for each band, the attenuation is more than 31 dB when ω_{02} is twice that of ω_{01}. An ideal lumped component simulation with dual-bands around 10 and 14 GHz each having 200 MHz of BW is shown in Figure 5-3. The trade-off between in-between bands and out-of-band attenuation is evident for the two synthesis cases of addition and subtraction. Note the out-of-band attenuation on higher side of the 14 GHz for the case of subtraction compared to addition, where the subtraction has mitigated the effects of less roll-off of a 2nd-order BPF. As a proof of concept of this approach, the subtraction mode was demonstrated using the design of [33].

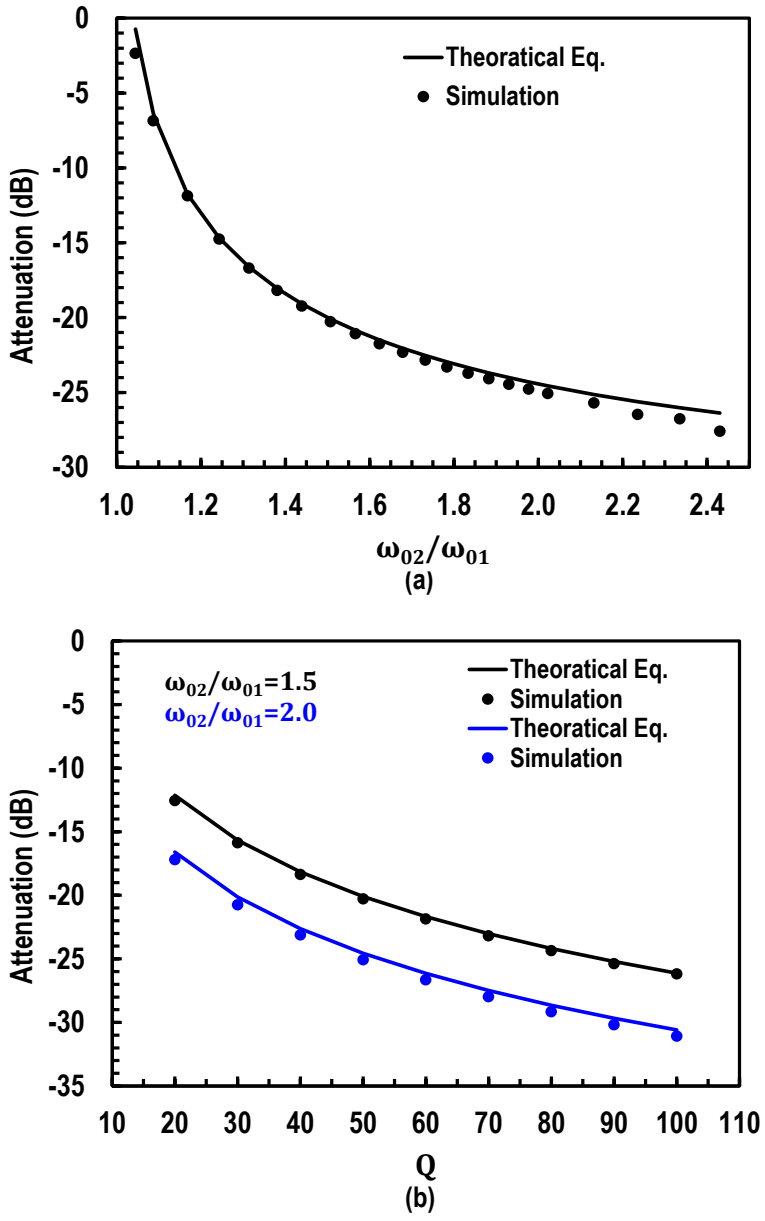

Figure 5-2: (a) In-between bands attenuation for theoretical approximate equation and simulation (a) vs dual-band frequencies ration and (b) vs Q of the each dual band.

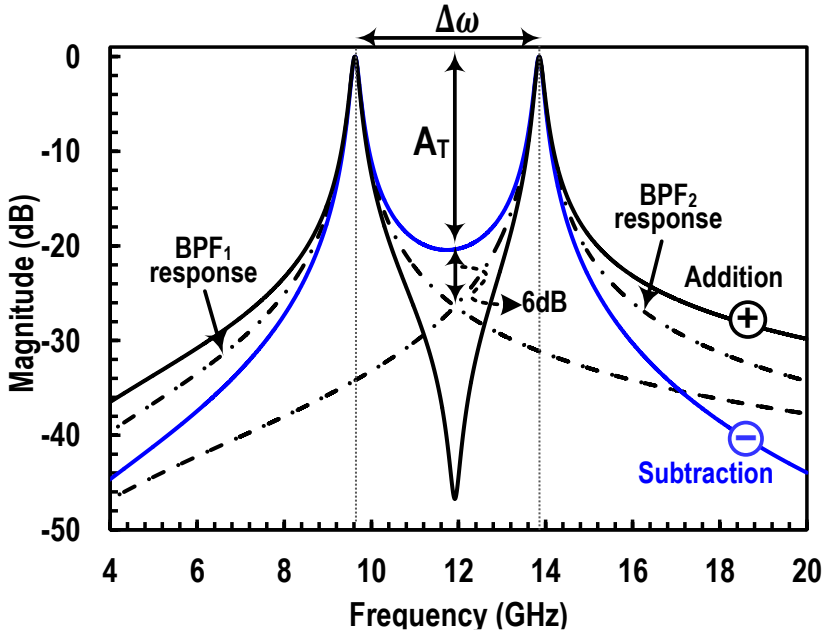

Figure 5-3: Ideal lumped circuit simulations of dual-band BPF at 9.7 and 13.9 GHz.

5.3 Circuit Design and Implementation

The proposed parallel synthesis technique requires independent tuning of the center frequency and Q of the LC-tanks. Figure 5-4(a) shows the block diagram of the proposed filter where two tunable 2nd-order BPFs outputs are subtracted using transistors ($Q_{A\text{-}B}$) and ($Q_{C\text{-}D}$) and resistor R_0 and R_E. Resistance R_0 also serves to match to 50Ω output for measurement purposes.

The 2nd-order LC band-pass filter consists of one parallel resonator or tank, which provides two negative frequency poles. For a lossy on-chip inductor the effective tank Q is that of the inductor with loss R_S at the resonance frequency of the tank: $Q_0 = \omega_0 L/R_s = 1/R_S.\sqrt{L/C}$. Then the equivalent parallel inductor L_P and loss R_P can be written as

$$L_P = \left(\frac{1+Q_0^2}{Q_0^2}\right)L_S, \qquad R_P = (1+Q_o^2)R_S \approx \frac{\omega_0^2 L^2}{R_S} \tag{6}$$

A negative resistance $R_N = -1/G_m$, to cancel the equivalent parallel loss R_P can be implemented using a transconductor with positive feedback as shown in Figure 5-4(e). The equivalent parallel resistance R_{EQ} and the enhanced quality factor Q_{EQ} can be expresses as

$$R_{EQ} = R_P \parallel \left(-\frac{1}{G_m}\right) = \frac{R_P}{1-G_m R_P} \tag{7}$$

and

$$Q_{EN} = \frac{R_{EQ}}{\omega_o L_P} = \frac{Q_0}{1-G_m R_P} \tag{8}$$

The Q can be made very high when $G_m R_P \rightarrow 1$. However the $-G_m$ needs to be precisely controlled to avoid oscillation which happens when the equivalent resistance R_{EQ} becomes negative. i.e. $G_m R_P \geq 1$.

The proposed dual-band band-pass filter in Figure 5-4, is implemented in IBM 0.13um SiGe BiCMOS process with f_T /f_{max}=180/220 GHz. The fabricated chip photograph is shown in Figure 5-5. Great efforts were made to achieve highly symmetric layout for differential matching. The core size of the filter, excluding pads, occupies 0.53x0.7 mm^2. The total chip area is 1.05x0.95 mm^2.

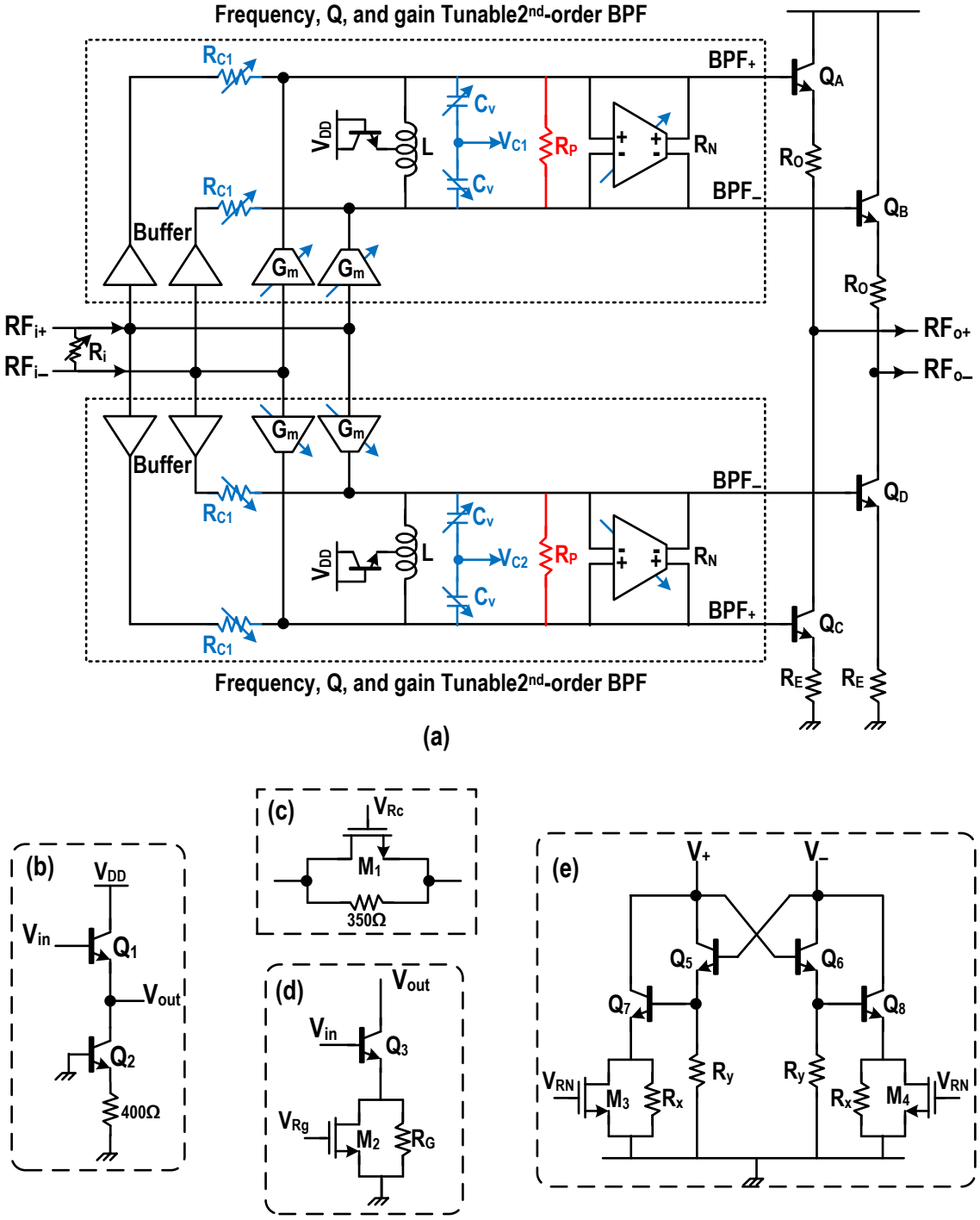

Figure 5-4: (a) Schematics diagram of the proposed filter using two 2nd-order BPFs with independent tuning, (b) the buffer cell, (c) The resistance R_{C1} implementation, (d) The variable G_m cell and (e) A linearized variable negative resistance R_N implementation.

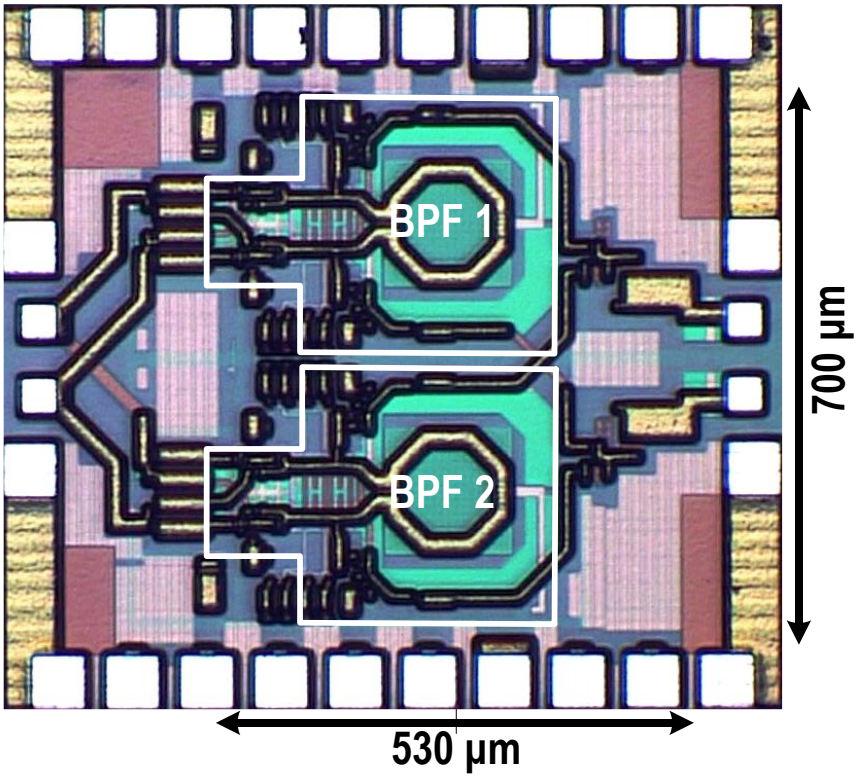

Figure 5-5: IBM SiGe 130nm chip micrograph with core area of 0.7x0.53 mm2.

5.3.1 2nd-order BPF Tuning

The LC-tanks are driven by a buffer and a transconductor as shown in Figure 5-4(a) for voltage and current mode driving, respectively. Since the LC-tanks are driven as well as loaded by unilateral components, no coupling exists between the two resonators, contrary to the case of traditional all-passive ladder and coupled resonator filter structures. Hence, the two LC-tanks can be independently controlled in terms of Q and center frequency tuning. The input buffer, realized by $Q_{1,2}$ (Figure 5-4(b)), drives the LC-tank in voltage mode. The variable resistor R_C consists of an nMOS M_1 and a resistor (Figure 5-4(c)) which is used to reduce the Q to as low as 4. A variable transconductance G_m, realized by Q_3 together with variable resistance R_G and M_2 in parallel (Figure 5-4(d)) is used to drive the tank in current mode in order to control the gain of the LC-tank. This enables control of the trade-off between noise and linearity. The LC-tank losses R_P are compensated by a Darlington-type negative resistance R_N as shown in Figure 5-4(e). This consists of a fixed negative $1/G_m$ realized by $Q_{5,6}$ and R_Y and a variable negative $1/G_m$ realized using nMOS $M_{3,4}$ and resistance R_X. The Q can be increased to more than 100 by controlling the negative resistance using $M_{3,4}$. This control also helps in keeping each BPF path stable.

5.3.2 2nd-order BPF Q and Stability

Figure 5-6(a) shows the Q of the LC-tank before compensation and the total tank Q with a load resistance R_C=350 Ω. The inductor Q, based on EM simulations, varies from 13~18 for frequencies 8~15 GHz whereas the varactor Q varies from 30~115. The resultant LC-tank Q with a load resistance R_C=350 Ω is in the range of 9~10 including all parasitic effects from interconnects. With compensation by the negative resistance R_N for both tanks, the Q can be increased to 100 or more. Figure 5-6(b) shows the post-layout stability simulations of the proposed filter as well as the measured stability factor from S-parameters. The simulation results show that for a Q of 100 for both bands, the stability parameters K>1 and B1>0 are satisfied by a large margin guaranteeing that the filter is unconditionally stable over large frequency range. The measured stability parameters are also plotted for Q=67 from 1 to 22 GHz showing unconditional stability similar to simulations.

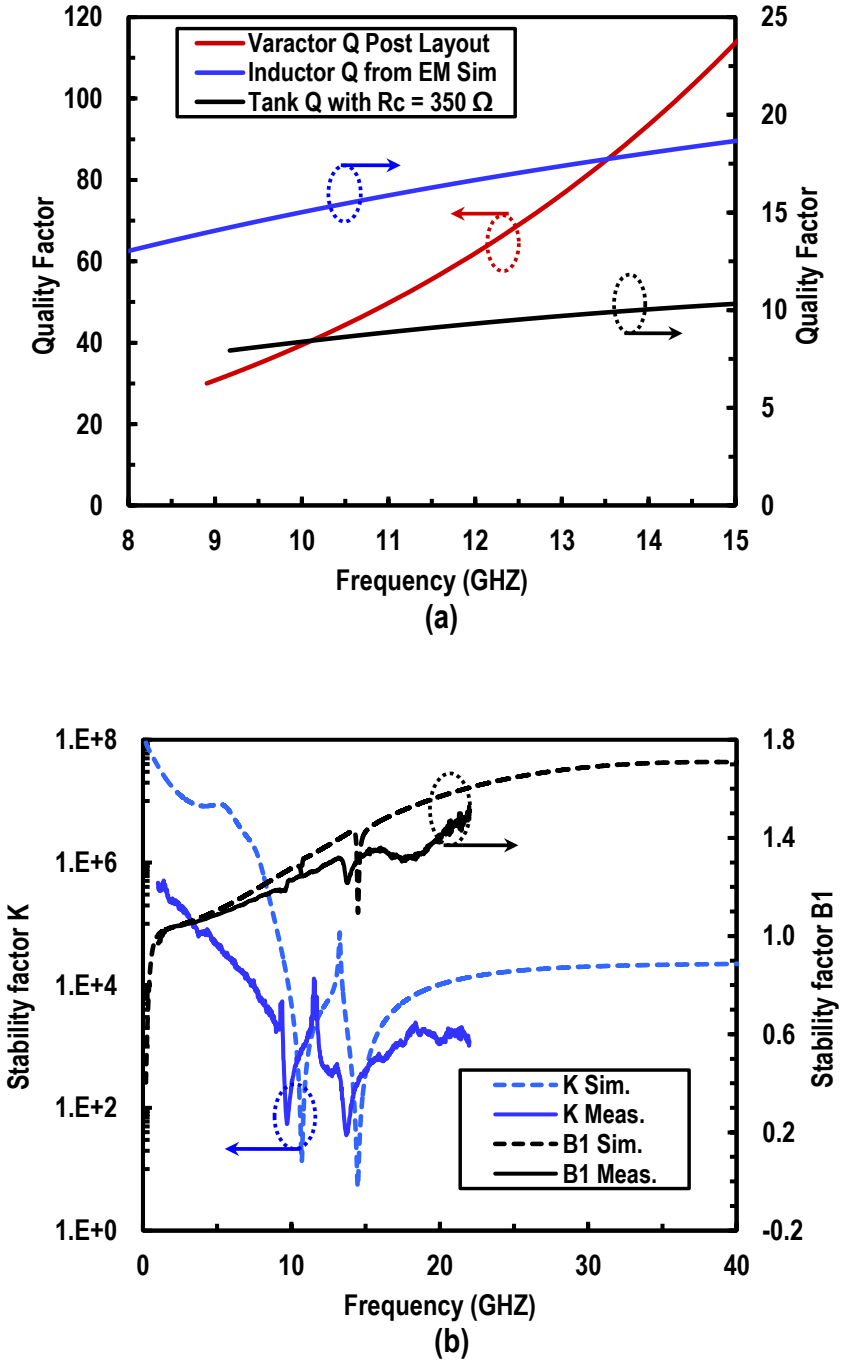

Figure 5-6: (a) Post layout simulated Q of the LC-tank components and (b) simulated stability factors when Q is increased to 100 using negative G_m and measured stability factors for Q=67.

5.4 Measurement Results

To verify the proposed tunable dual-band filter approach, the fabricated chip was measured using GSSG probes with differential SOLT calibration. To interface with single-ended 50Ω equipment, 180-degree hybrid couplers were used for differential to single-ended conversion.

5.4.1 Bandwidth (Q) Tuning

The measured dual-band filter response is plotted in Figure 5-7(a) which shows normalized S_{21} plots for different Qs, ranging from 20 to 67. The Q tuning is independent and continuous by controlling each tank's R_C and R_N (Figure 5-4(a)) though only discrete Q tuning steps are shown for clarity. The dual-bands are tuned at 9.7 and 13.9 GHz. With this band-separation, the attenuation is more than 22 dB for bandwidths of 200 MHz each. Due to subtraction, the out-of-band attenuation on the lower side is >50 dB below 4 GHz, and, more significantly, >48 dB on the higher side of the filter at 20 GHz and above. The roll off continues on the lower and upper side frequencies beyond the plot limits. The bands can be tuned independently up and down in frequency using varactor control, while Figure 5-7(b) shows the band tuning across the frequency by tuning the lower BPF. The S_{11} and S_{22} measurements are shown in Figure 5-8(a) for the filter tuned at 9.7 and 13.9 GHz. each with Q of 50. The output matching is very good with S_{22} <-14 dB. The S11 is -10.2 and -8.8 dB at 9.7 and 13.9 GHz respectively. The group delay measurement plots are shown in Figure 5-8(b) for Qs of 20 and 50. The total group delay is around 0.8 ns for Q=20 and 1.9 ns for Q=50.

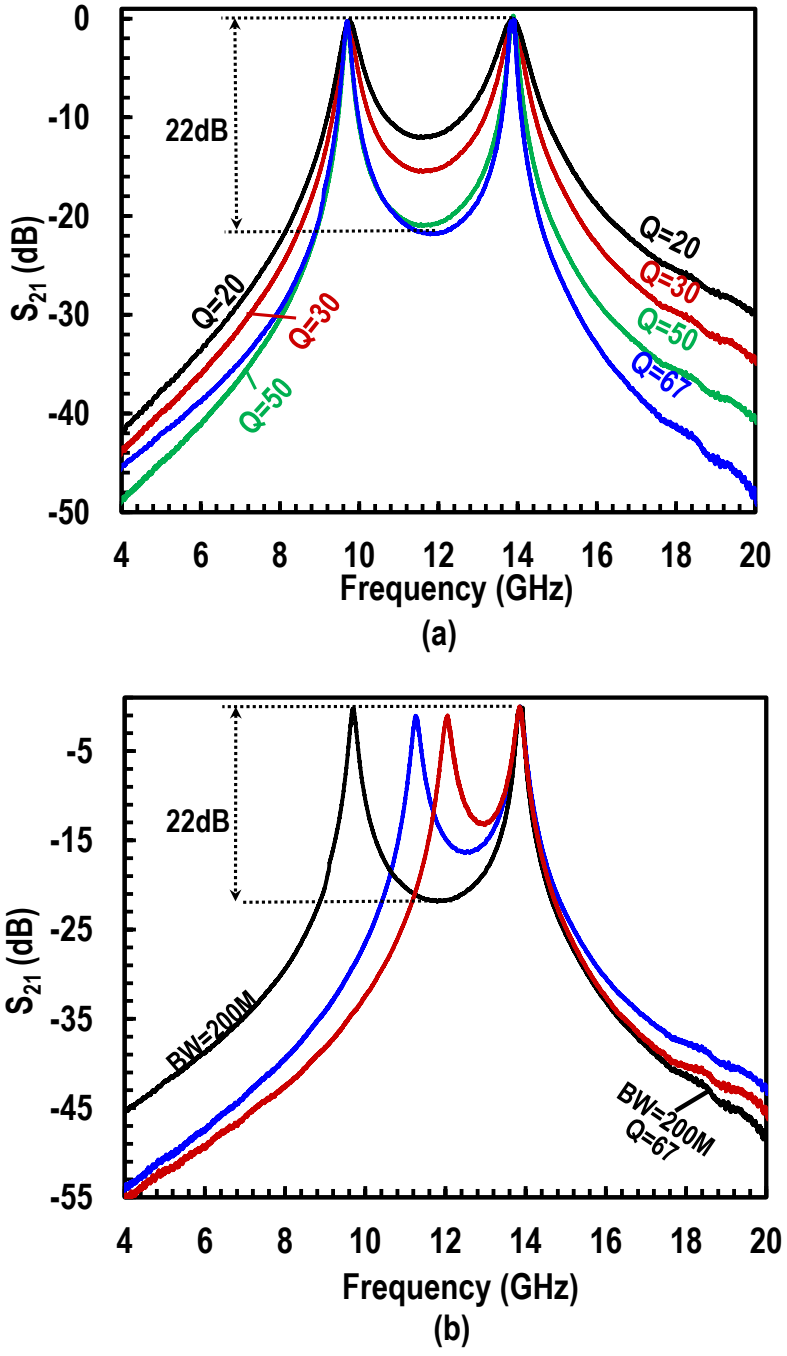

Figure 5-7: (a) Measured filter response at 9.7 and 13.9 GHz with Q tuning from 20 to 50 and (b) measured center frequency tuning of the upper-band.

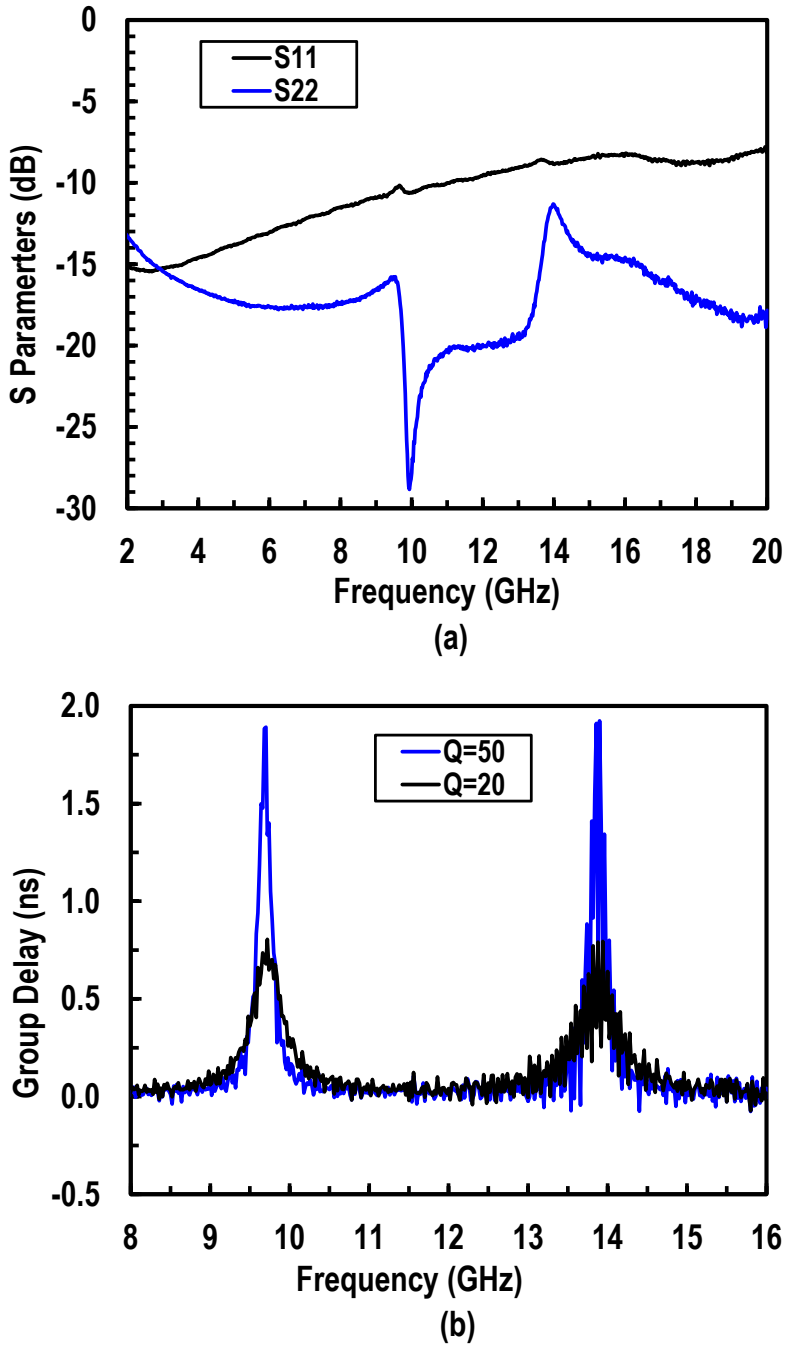

Figure 5-8: Measured (a) S_{11} and S_{22} and (b) group delay for Q of 20 and 50.

5.4.2 Noise Figure and Linearity

The NF and P_{-1dB} are plotted in Figure 5-9 (a). The NF is measured for both input matched and high impedance case using Ri in Figure 5-4(a). The normalized DR, the ratio of P_{-1dB} to the 1-Hz BW input referred noise, for the input matched case is plotted in Figure 5-9(b). The normalized DR varies from 164.6~154.5 for the lower band, and 160~152 for the upper band for Q=20~50 at the expense of 115-130 mW DC power. The measured P_{-1dB} for Q=20~50 is 3~3.6 dBm and 6~0.4 dBm for lower and upper bands respectively. The NF can be reduced by increasing the gain from the variable transconductance amplifier G_m in Figure 5-4(a).

5.4.3 Performance Comparison to off-chip and on-chip filters

Table 1-1 shows the performance summary and comparison with state of the art on-chip dual-band filters. The proposed Q-enhanced dual-band filtering is advantageous at microwave frequencies with higher out-of-band attenuation, independent dual-band tuning, and better DR performance compared to prior integrated N-path filter implementations. Additionally the proposed dual-band filter performance is also compared with off-chip filters in Table 5-2. The off-chip filters are generally higher-order than the 2^{nd} order dual-bands in this work. It is also worth mentioning that most of the off-chip filters have dual-band center frequency ratios of more than 2. Apart from small area and tunability, the proposed filter, if designed for frequency ratios >2, can achieve in-between bands attenuation, as shown in Figure 5-2(b), similar to off-chip filters in Table 5-2.

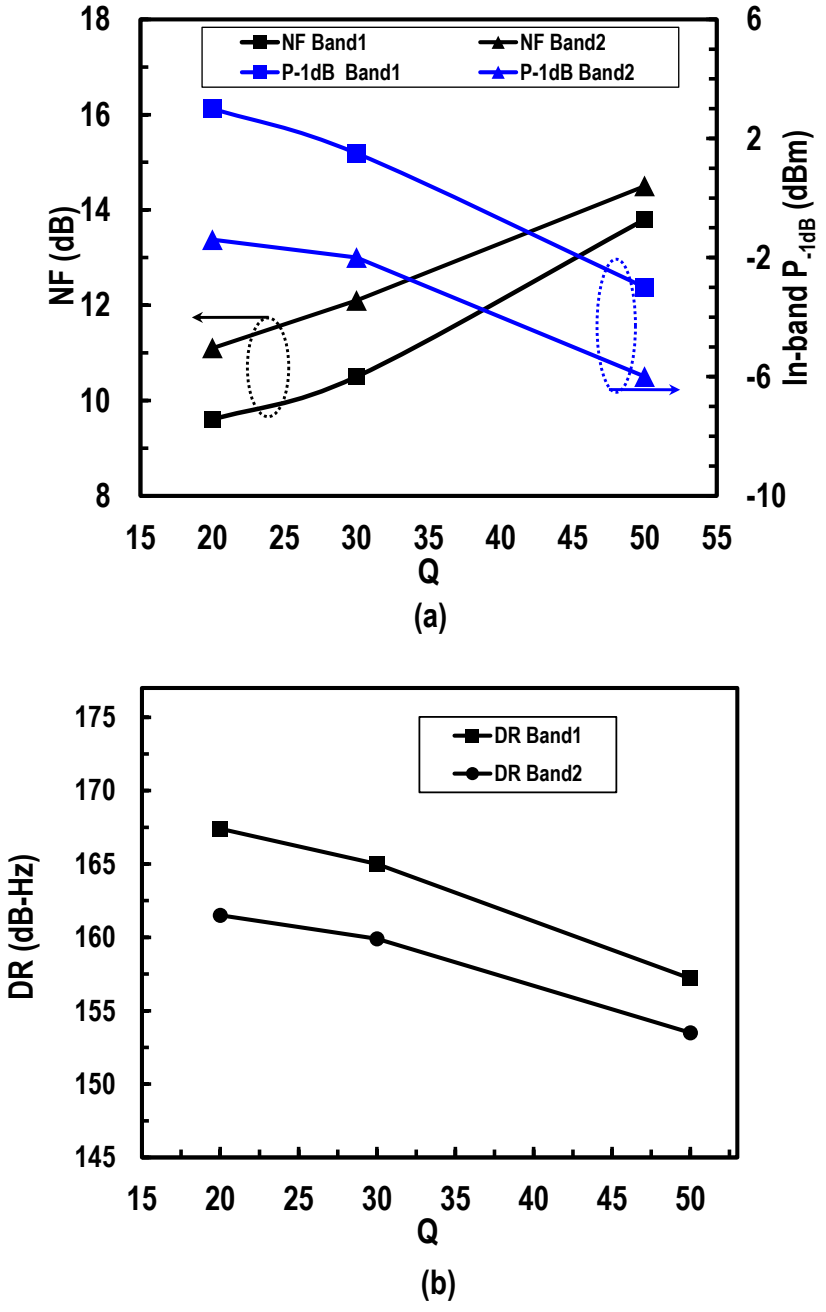

Figure 5-9: Measured (a) in-band P_{-1dB} and NF verses Q and (b) normalized dynamic range.

Table 5-1: Performance Comparison with On-Chip Filters.

References	Type	Freq. (GHz)	Channles/ Bands	BW of each Band (MHz)	Filter Q	NF (dB)	IP_{-1dB} (dBm)	Normalized DR[c] (dB·Hz)	Ultimate Rejection(dB)	Power (mW)	Area (mm^2)	Process
This Work	Q-enhanced LC	9.7 ~ 13.9	2	200 ~ 700	20 ~ 67	9.6 ~ 13.8[d]	−3 ~ 3.6[d]	165 ~ 154.5[d]	> 50	115 ~ 130	0.371	130 nm SiGe BiCMOS
[25]	N-path Filter	0.1 ~ 12	1	150	1 ~ 80	-	−3.6[c] @12GHz	-	~20 @12GHz	130 @12GHz	0.36	32 nm SOI CMOS
[19]	N-path RX	0.7 ~ 2.5	3 (Intra-band)	1 ~ 30	-	4.8	<−19[c]	< 150	> 40 with a notch	150~362[b]	7.8	65 nm CMOS
[59]	N-path RX	0.5 ~ 3.6	4 (Inter, intra-band)	-	-	3.7 ~ 4.5	−7.1[c]	-	44	46	0.3	28 nm CMOS
[60]	N-path Image-Reject RX	0.5 ~3	2 (Intra-band)	-	-	4.5	−4.1[c]	~165	25	15 @2GHz	0.16	45 nm CMOS

[a]calculated from 174+IP_{-1dB} – NF, [b]including CLK generator power [c] calculated from IIP3 – 9.6 dB [d] at 9.7 GHz for Q=20~50

Table 5-2: Performance Comparison with Off-Chip Filters.

References	Type	No of. Bands	Center Frequencies (GHz)	Ratio of Center Frequencies	BW of each Band (MHz)	In-between bands Attenuation (dB)	Ultimate Rejection(dB)	Area
This Work	Q-enhanced LC on-Chip	2	9.7 / 13.9 Tunable	1.43	200 / 200 Tunable	~22	> 50	0.37 mm^2
[52]	SIW cavities	2	2.51 / 5.30	2.11	170 / 307	~31	>45	-
[55]	Substrate step-impedance resonators	2	1.57 / 3.5	2.23	240 / 400	~35	> 50	>300 mm^2
[57]	Folded SIW cavities	2	2.4 /5.2	2.17	180 /300	~33	> 40	-
[58]	SIW cavities	2	9.23 /14.05	1.52	260 /780	~35	>50	~ 40 cm^2

5.5 Summary

This chapter presented an integrated Q-enhanced dual-band filtering solution at X and Ku band microwave frequencies using 0.13µ um SiGe BiCMOS. The filter dynamic range is 164.6-154.5 dB and 160-152 dB at the demonstrated lower (9.7 GHz) and upper (13.9 GHz) bands, respectively. The dual-band filtering approach using the subtraction method has the advantage of increased out-of-band attenuation on the lower and upper sides of the two passband responses. The concept of dual-band independent tuning operation can be extended to wide range of operating frequencies by appropriately designing the tanks.

Chapter Six: **Tunable wideband Band-Reject Filter**

6.1 Introduction

The suppression of interference in wideband multi-standard communications systems is an increasing challenge given today's crowded and dynamic electromagnetic environment. For this purpose, there is an increasing need for tunable band-reject or band-stop filtering which can suppress very strong interferers. Band-pass filtering is typically used to filter out some of the interferers but suffers from bandwidth-selectivity trade-offs, particularly for on-chip implementations. Notch filtering is used to suppress blockers but their on-chip implementations to date(e.g. [33], [61]-[62]) are limited to 2^{nd} –order only which attenuates a single frequency or a very narrow band on the order of kHz for a typical attenuation of more than 20 dB. Modern and future systems have requirements for larger bandwidths, 100s of MHz to GHz in the case of radars. Therefore, tunable wideband band-reject filtering is needed to reject interference having a large bandwidth.

This chapter introduces a novel technique to synthesise a wideband tunable band-reject filter compared to the single frequency or very narrow band limitation of the notch filter. The bandwidth of the rejection band can be as large as on the order of tens to hundreds of MHz at C band (4~8 GHz) and beyond. A rejection of more than 20 dB can be easily achieved. The band-reject filter is

implemented at circuit level by re-using some of the building block from the 4th-order BPF design presented in chapter 2 and 3. A test chip containing wideband band-reject filters at S and C bands was designed for fabrication in GF 130 nm SiGe BiCMOS 8HP.

6.2 Parallel Synthesis of wideband band-reject filter

Figure 4-2 shows the block diagram of the proposed tunable band-reject filter. The filter consists of three parallel conditioning sections. Two identical parallel BPF sections tuned at slightly different center frequencies $\omega_{01}$and ω_{02} are added in phase first, the result of which is then subtracted from the All-pass section. Due to the phase properties of the BPF sections and the all-pass section, a wider band band-reject filter shaping can be formed at the output. The center-frequency spacing of the parallel BPF sections establishes the wideband band-reject filter attenuation bandwidth. The most common attenuation level for specifying notch bandwidth is 20 dB, i.e. the bandwidth of the notch is measured at -20 dB from the passband level. The attenuation $x\ dB$ at a specified bandwidth for a 2nd-order notch filter can be calculated using [34]

$$A_{dB} = 10\log\left[1 + \left(\frac{f_0}{Q \times BW_{xdB}}\right)^2\right]. \quad (1)$$

For example, if the 3-dB BW is 100 MHz, the attenuation when the notch bandwidth reaches 30MHzis calculated to be 10.8 dB, and 40 dB of attenuation for a 1 MHz bandwidth. The attenuation in (1) can also be expressed in terms of 3-dB bandwidth of the notch as follows:

$$A_{dB} = 10\log\left[1 + \left(\frac{BW_{3dB}}{BW_{xdB}}\right)^2\right]. \quad (2)$$

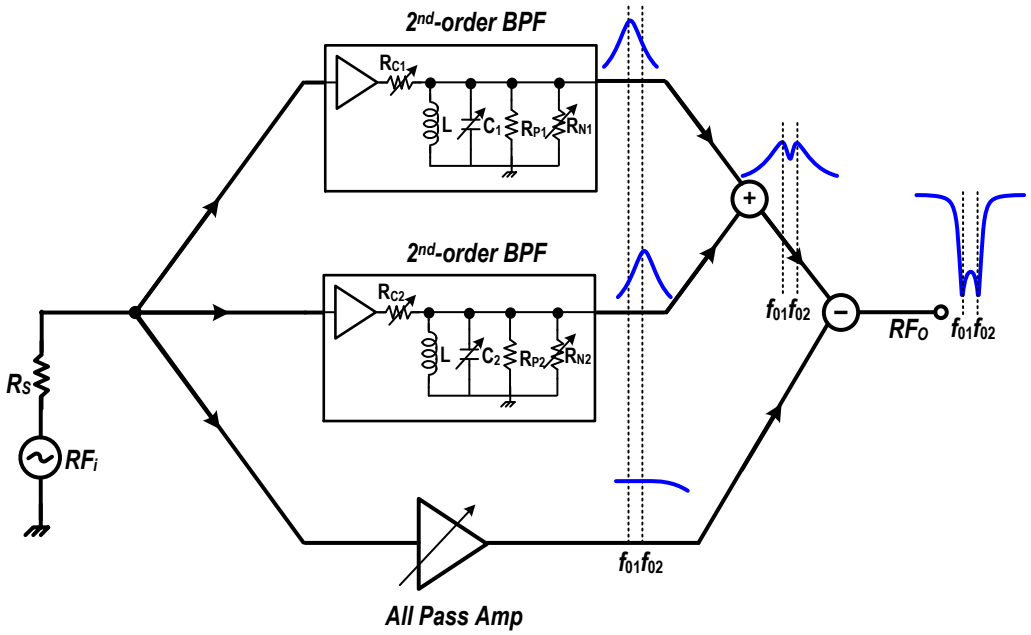

Figure 6-1: Block Diagram of the proposed wideband tunable band-reject filter.

6.2.1 Ideal Simulation Results

Figure 6-2 (a) shows ideal component simulations for the proposed band-reject filter technique centered at 5 GHz. For this example, design, the Qs of the individual BPFs are set at 30, which can be easily achieved as reported in previous chapters using Q-enhanced LC filtering. The two distinct notches can be seen in the final band-reject filter response. This simulation shows a midband rejection of around 33 dB is possible for BPFs Q of 30. The 33-dB bandwidth in this case is around 50 MHz. The ripple in the band-reject filter is a function of spacing between the two BPFs tuned frequencies and their Q.

A bandwidth tuning of the proposed band-reject filter is shown in Figure 6-2 (a) , where the Q of the individual BPFs are kept constant but the spacing between the center frequencies is varied. By doing so, the band-reject attenuation can be increased further where the maximum attenuation bandwidth is reducing. Similarly, the 3-dB bandwidth can be tuned by changing the Q of the individual BPFs as shown in Figure 6-2 (b), where the Q of the individual BPFs are 50 and 30 for

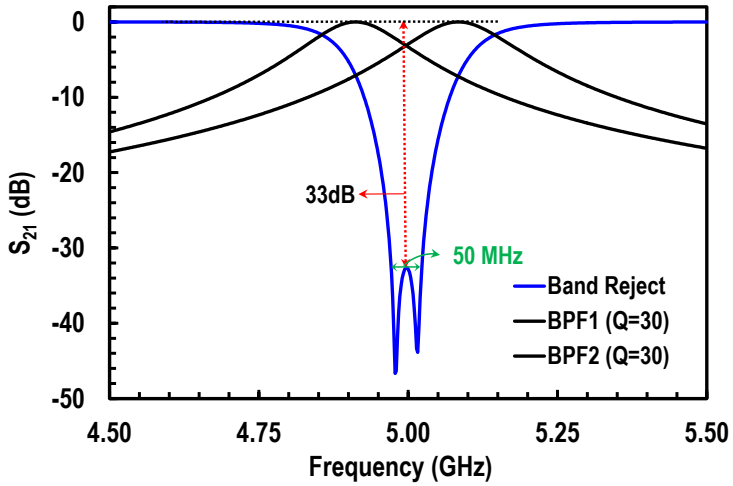

Figure 6-2: Ideal simulation of band-reject filter at 5 GHz center frequency with >33 dB rejection.

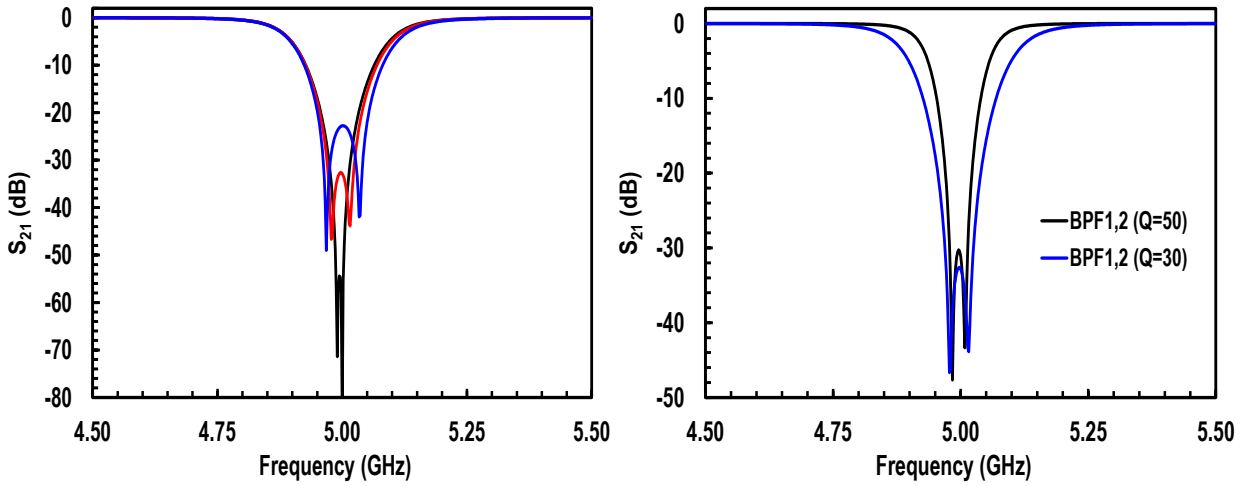

(a) (b)

Figure 6-3: (a) Ideal simulation of band-reject filter with rejection bandwidth tuning for constant Q of the two BPFs and (b) 3-dB bandwidth tuning at the center frequency of 5 GHz.

the two cases plotted.

6.2.2 Circuit Design and Post-Layout Simulations

Figure 3-1 shows the block diagram of the proposed circuit with detailed circuit schematic of the 2^{nd} –order BPF. The BPF schematic is the same as that of a 4^{th}-order BPF covered in chapter 3. The BPF has a switched varactor control scheme to improve the linearity of the varactor. Figure 6-5 shows the differential circuit diagram of the combining network which takes the two BPF outputs and the all-pass output and adds them in-phase and out-phase, respectively. The two BPF filter outputs are added in phase using parallel common emitter circuits, realized by Q_B and $R_{E1,2}$ in the current domain. The output of these two paths is out-of-phase with respect to the all-pass path which is added using common collector circuit realized by Q_A and R_0. Figure 6-6 shows the layout of the implemented tunable band-reject filter in GF 8HP SiGe BiCMOS technology with a core area of $700 \times 550\ \mu m^2$. The post layout simulation results are plotted in Figure 6-7 where the band-reject filter is tuned to around 4.4 GHz with more than 22 dB of attenuation. The 20dB bandwidth is 115 MHz whereas the 3dB bandwidth is 340 MHz. The NF of the pass-band output is around 11.3 dB, and the P_{-1dB} is -2 dBm. The performance, when the band-reject filter is tuned at 7.4 GHz is also shown in Figure 6-8.

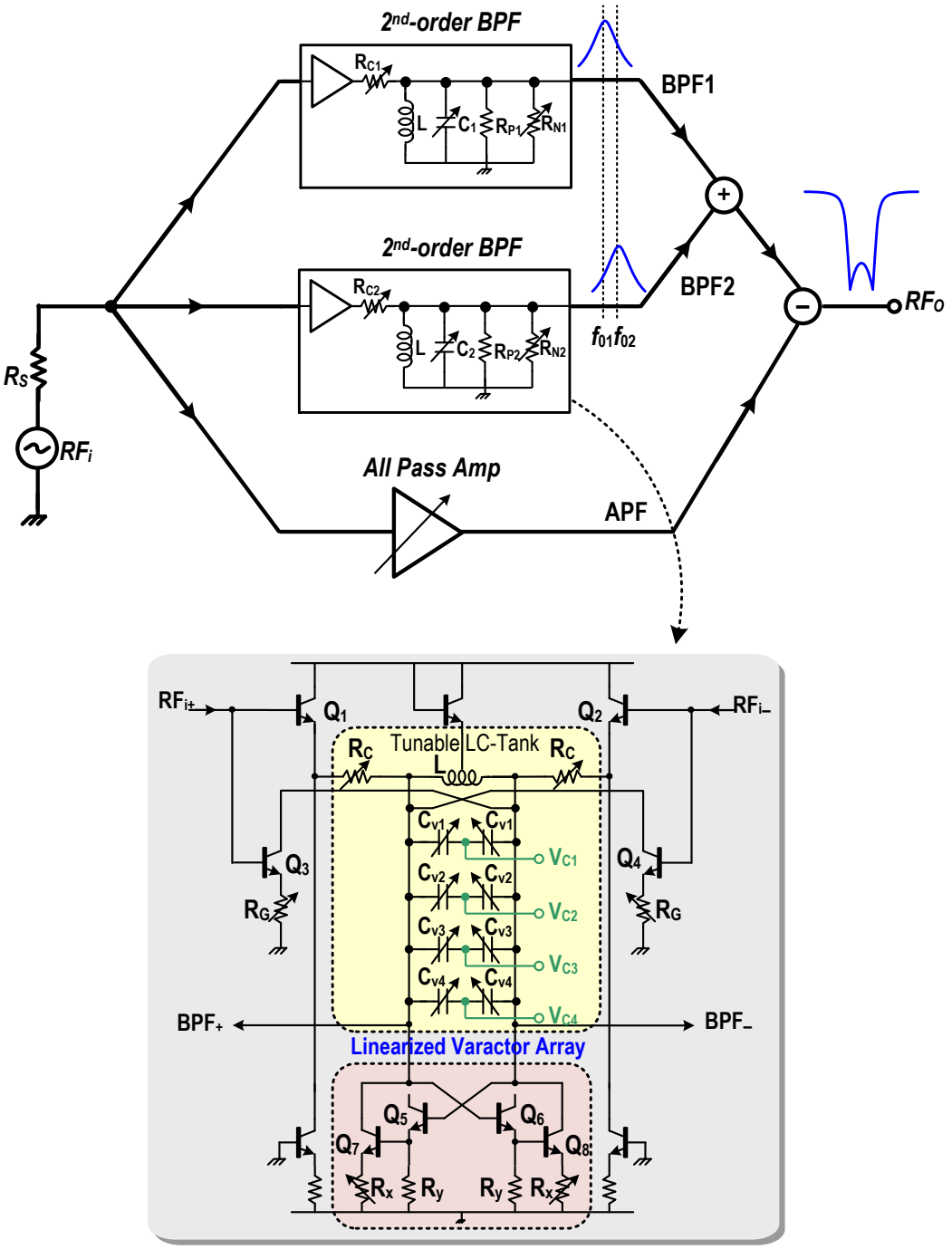

Figure 6-4: Circuit diagram of the Tunable (Q, center-frequency, and gain) 2nd-order BPF.

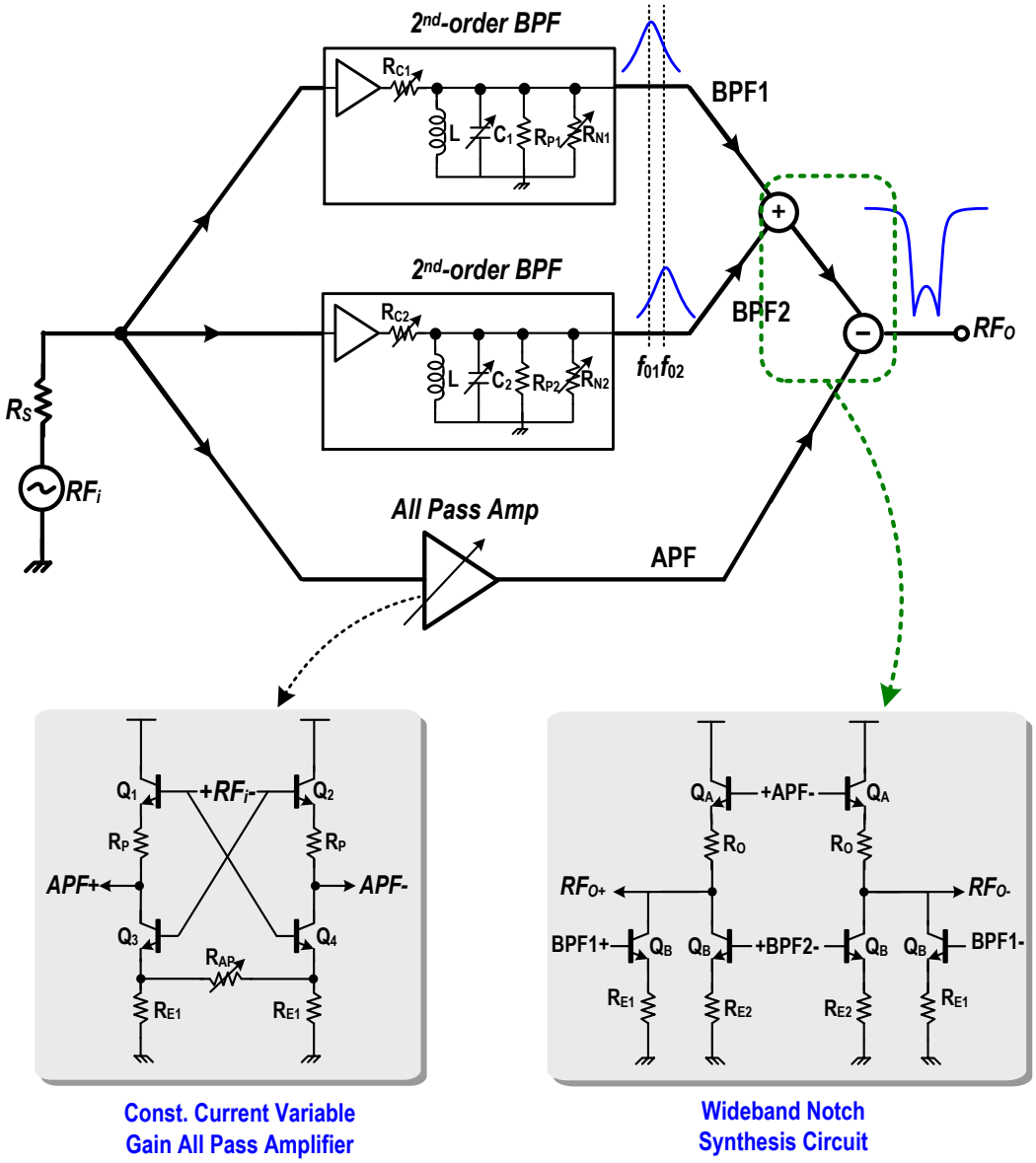

Figure 6-5: Circuit diagram of the gain tunable all-pass amplifier and equivalent wideband notch synthesis circuit for the in-phase and out-of-phase addition of three branches.

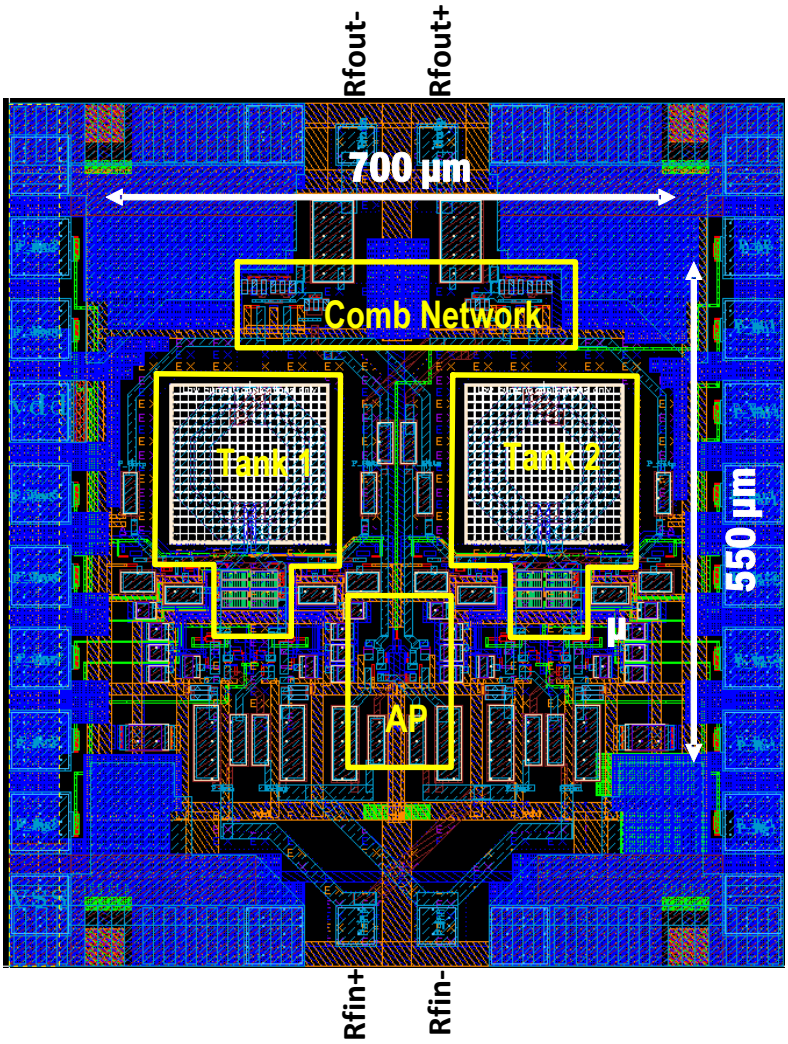

Figure 6-6: Layout of the tunable wideband band-reject filter in GF 130nm SiGe BiCMOS technology.

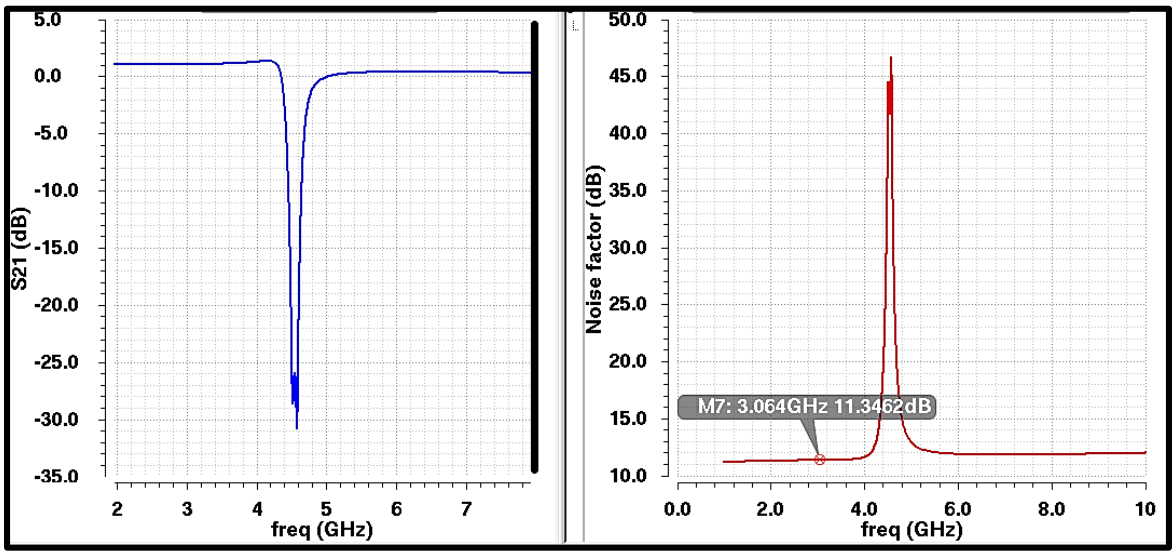

Figure 6-7: Post-layout simulations of band-reject filter around 4.4 GHz with a 20-dB and 3-dB bandwidth of 115 MHz and 3dB respectively, and noise figure (noise factor in dB).

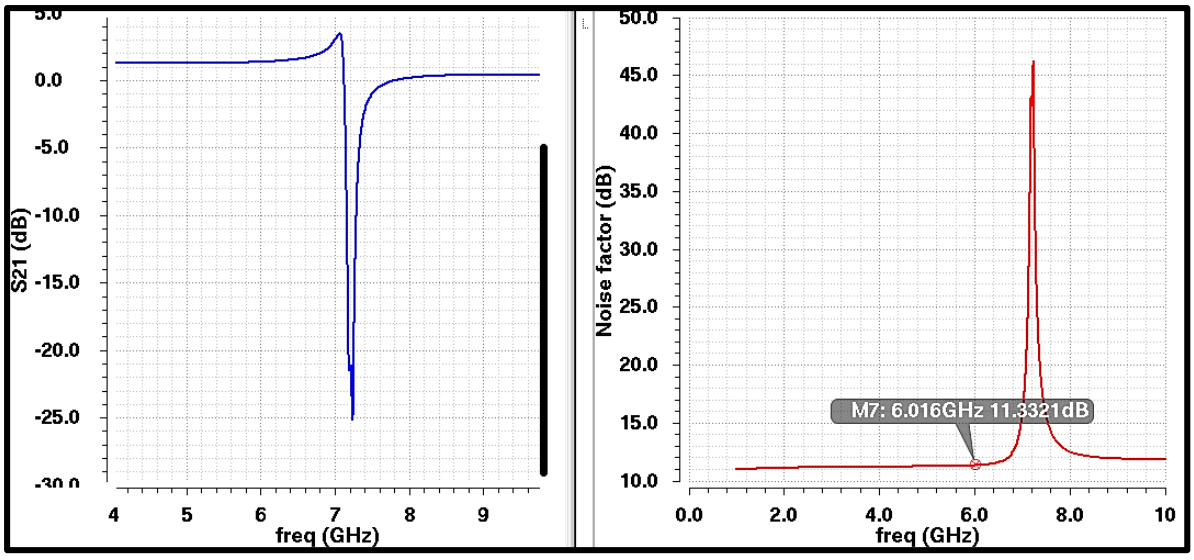

Figure 6-8: Post-layout simulations of band-reject filter around 7.4 GHz with a 20 dB and 3dB bandwidth of 75 MHz and 290 MHz respectively.

6.3 Summary

This chapter presented first of a kind integrated Q-enhanced wideband band-reject filter using 0.13µ um SiGe BiCMOS. The filter employs two BPF and one all-pass variable gain amplifier path to synthesize a wideband band rejection. The filter achieves more than 20 dB of wideband attenuation. The attenuation bandwidth is on the order of 10s of MHz to 100s of MHz. The band-reject filter can be tuned for center frequency operation and the for the attenuation bandwidth. The concept wideband band-reject filtering with tuning operation can be extended to wide range of operating frequencies.

Chapter Seven: **Conclusions and Future Work**

7.1 Conclusions and Contributions

In this dissertation, parallel synthesis techniques have been proposed and implemented for a variety of higher-order filtering shapes. Parallel synthesis approaches are advantageous for on-chip active LC implementations of higher-order filters compared to traditional cascading of resonators. The following contributions are made to the advancement of integrated tunable higher-order filtering.

- A 4^{th}-order wideband tunable bandpass filter was proposed and implemented in SiGe BiCMOS technology. Along with center frequency tuning, the filter achieves first ever reported 3-dB bandwidth tuning from 2% to 25%, representing 120 MHz to 1.5 GHz of bandwidth at 6 GHz. A new set of design equations were derived for the 4^{th}-order parallel synthesis BPF.
- A practical switched varactor control scheme was proposed to greatly reduce the non-linearities from the varactor linearity improvement of BPF. A four-control switched varactor scheme was implemented for the 4^{th}-order BPF which substantial improved the linearity for low Q cases, are need for large 3-dB bandwidth synthesis. A separate eight-control switched varactor was also designed to characterize the linearity improvement.

- Addition and subtraction techniques were proposed to realize tunable dual band filters. The subtraction approach improves out-of-band attenuation; the addition approach creates a deeper notch between two BPFs. The dual band filter is implemented in SiGe BiCMOS technology at X and Ku bands with more than 50 dB of ultimate out-of-band attenuation in the subtraction mode.
- A true tunable wideband band-reject filter design was proposed using parallel synthesis of two band-pass filters and an all-pass path. The proposed band-reject scheme is tunable and wide 20dB attenuation bandwidths on the order of 10s of MHz to 100s of MHz can be achieved.

7.2 Future Work

This section outlines suggested future research directions in order to fully exploit the parallel filter synthesis techniques developed in this work.

7.2.1 Verification of the tunable wideband Band-Reject Filter

The tunable band-reject filter design proposed in this dissertation has been done by re-use of the blocks from the works discussed in prior chapters, plus a tunable all-pass filter and combiner circuit. The band-reject chip is pending fabrication and will be measured to verify the concept and to characterize the sensitivity of band-rejection filter to parasitics and tuning control voltages.

7.2.2 Reconfigurable high-order BPF and BRF

The second direction for further research is the design of a switch network as shown in Figure 7-1. The purpose of proposed switch network is to enable and disable different paths as well as switch the differential signals for the in-phase and out-of-phase addition. This in turn enables the three parallel paths (two BPFs and one all-pass) configuration to

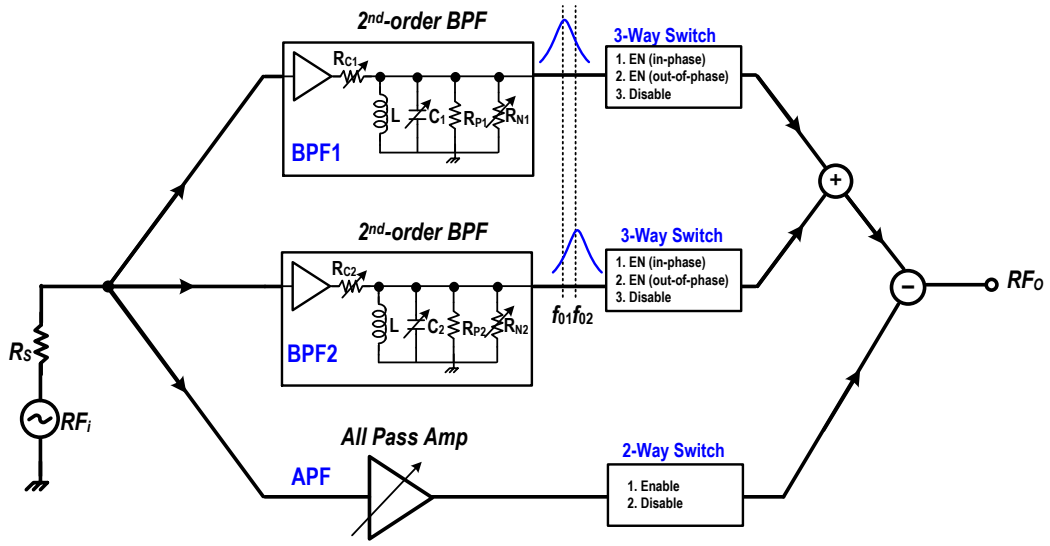

Figure 7-1: Block Diagram of the proposed future work switch network for a dynamic filter.

Table 7-1: Types of Filtering using switch network architecture of Figure 7-1.

No	Parallel Path Configuration	Addition	Resultant Filter Type
1	BPF1 only	NA	2nd-order BPF
2	BPF1 and BPF2	Out-of-phase	4th-order BPF
3	All-pass only	NA	All pass Amplifier
4	Large frequency-spaced BPF1 and BPF2	Out-of-phase	Dual-band BPF with large out-of-band attenuation
5	Large frequency-spaced BPF1 and BPF2	In-phase	Dual-band BPF with sharp notch in-between bands
6	BPF1 and All-pass with	Out-of-phase	2nd-order Notch Filter
7	BPF1, BPF2, and All-pass	In-phase followed by out-of-phase	Wideband Band-Reject Filter
8	Large frequency-spaced BPF1, BPF2, and All-pass	In-phase followed by out-of-phase	Dual-band 2nd-order Notch filter

do a variety of filtering functions as summarized in the Table 7-1.

7.2.3 Parallel Filter Synthesis in Gallium Nitride MMIC

For radar and high power RF environment applications, the parallel synthesis techniques devolved in this dissertation can be implemented as a Gallium Nitride (GaN) based Monolithic Microwave Integrated Circuit (MMIC). The idea is to take advantage of the high power handling of GaN device therefor enabling the path to tunable high power linear filtering. One challenge is the relative lack of multilevel metallization and control device pcells in currently available GaN foundry technologies.

7.2.4 Automatic Tuning Control and Sensitivity Analysis

For practical system implementations of the proposed filters in this dissertation, automated tuning will be needed. Most importantly a closed loop control mechanism should be implemented for precise center-frequency control. Some of the automatic closed loop tuning approaches for low frequencies and implementation details can be found in [63]-[64]. For the less sensitive tuning controls for gain and Q, especially low Q control of the filter, a lookup table scheme can be incorporated. When implementing such automatic tuning schemes, sensitivity analysis to control voltages will be needed to help in the design process .

Appendix A: Circuit level Linearity Simulations

The following circuit level linearity simulation for a 2nd-order BPF were performed to characterize the amount of non-linear contribution in terms of IMD_3 by each block.

A1. Buffer and Tank impedance

The IMD3 simulation were performed for Q =20 around 4.4 GHz. For a Q=20, C=4 pF, L=4.4 GHz resulting in f=4.4 GHz, the total resistance $R_{Total} = Q/\sqrt{L/C}$ is 180 Ω. The resistance $R_C' = R_C + 20 = 370\ \Omega$. Then the tank resistance R_T is given by

$$\frac{1}{R_{Toatl}} = \frac{1}{R_T} + \frac{1}{R_C{}'} \quad \Rightarrow \quad R_T = \frac{R_C{}' R_{Total}}{R_C{}' - R_{Total}} = \frac{370 \times 180}{370 - 180} = 350\ \Omega$$

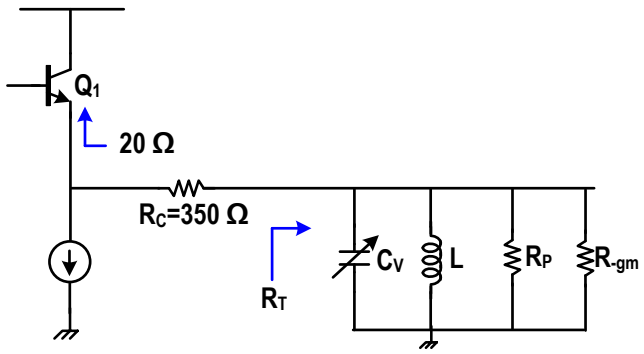

Figure A.1 Diagram of the put buffer and tank impedances.

A2. Input Buffer

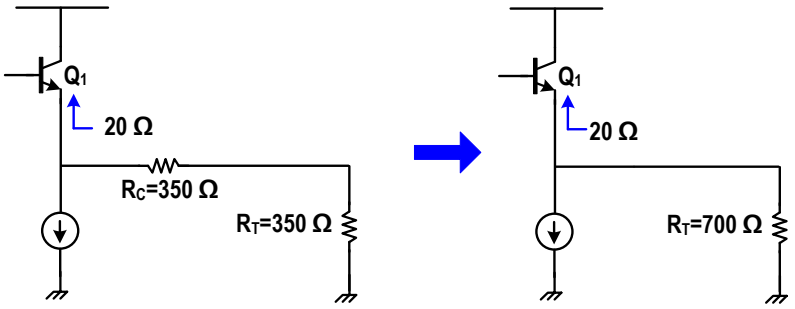

Figure A.2 The total impedance seen by the buffer.

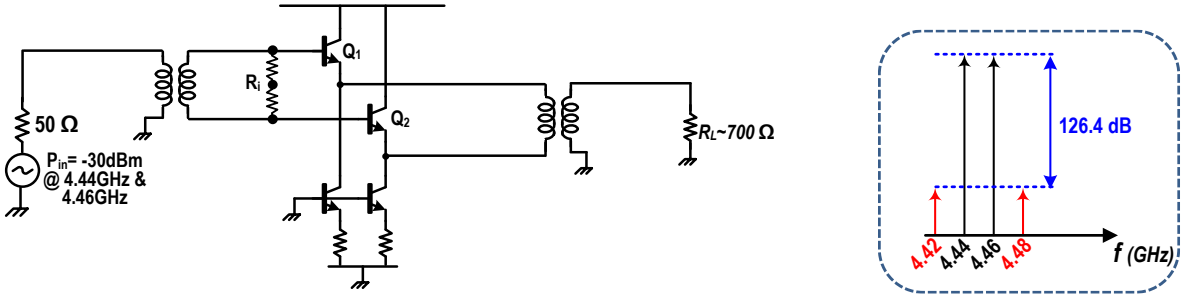

Figure A.3 Input buffer circuit and resultant IMD_3

A3. Input Buffer and Q Control Resistance

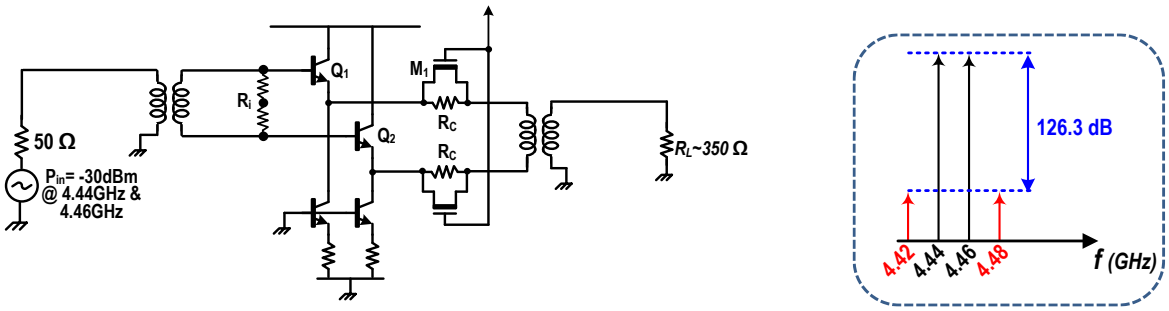

Figure A.4 Input buffer circuit with resistance R_C and resultant IMD_3

A4. Voltage and Current mode driving

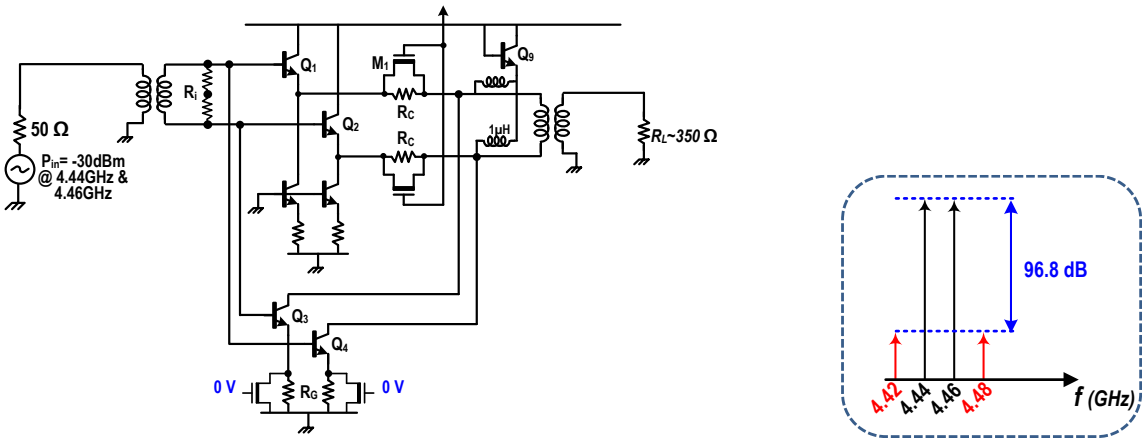

Figure A.5 Voltage mode and current mode driving circuit with gain stage turned off and resultant IMD_3

Gain Stage NMOS is turned on around typical values for a gain of 0~2 dB. Figure A.6 shows the resultant circuit and IMD_3 value.

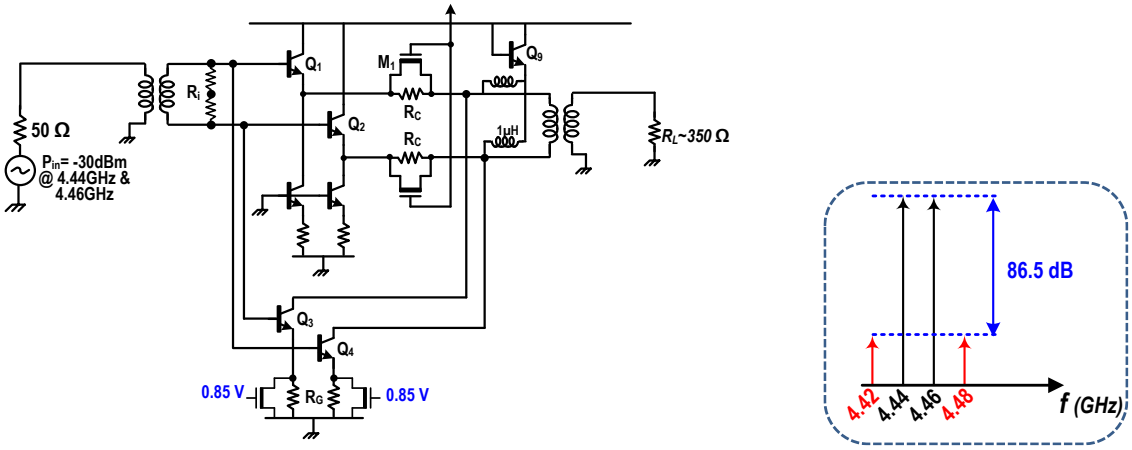

Figure A.6 Voltage mode and current mode driving circuit with gain stage turned on and resultant IMD_3

A5. BPF with LC-tank and compensation

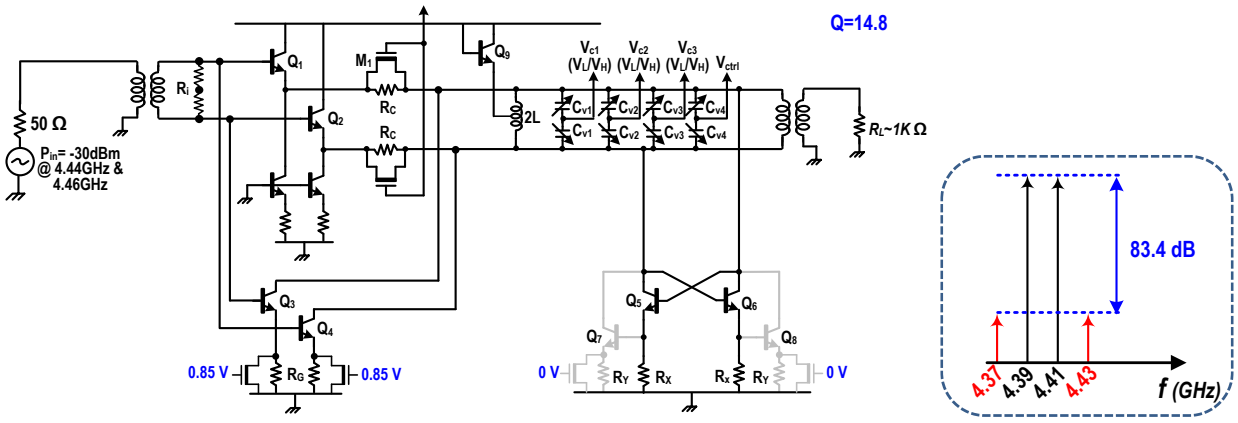

Figure A.7 BPF with LC-tank, and compensation circuit with fixed negative resistance turned on providing Q=14.8 and resultant IMD_3

Next the negative resistance circuit is turned to make the Q=20 which is the targeted test case for the simulations.

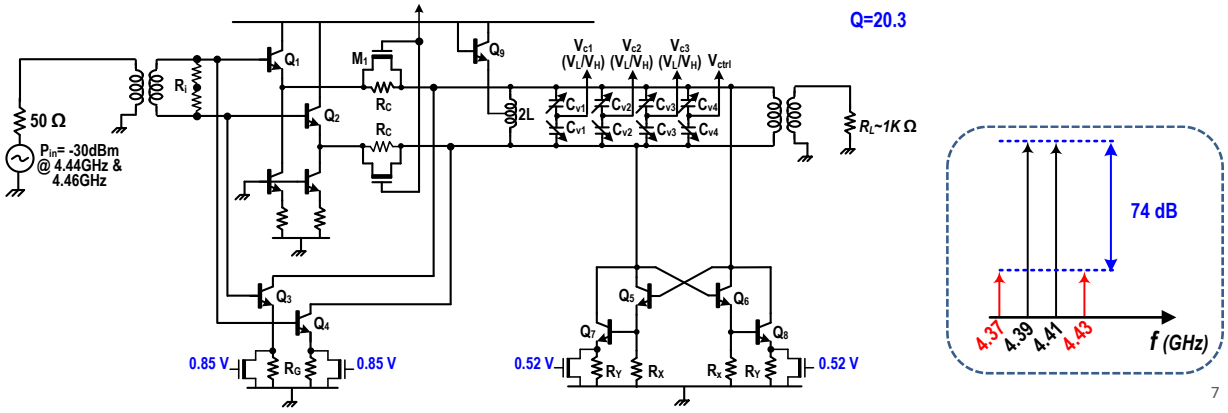

Figure A.8 BPF with LC-tank, and compensation circuit with negative resistance turned on providing Q=20 and resultant IMD_3

A6. BPF with LC-tank and Output Buffer

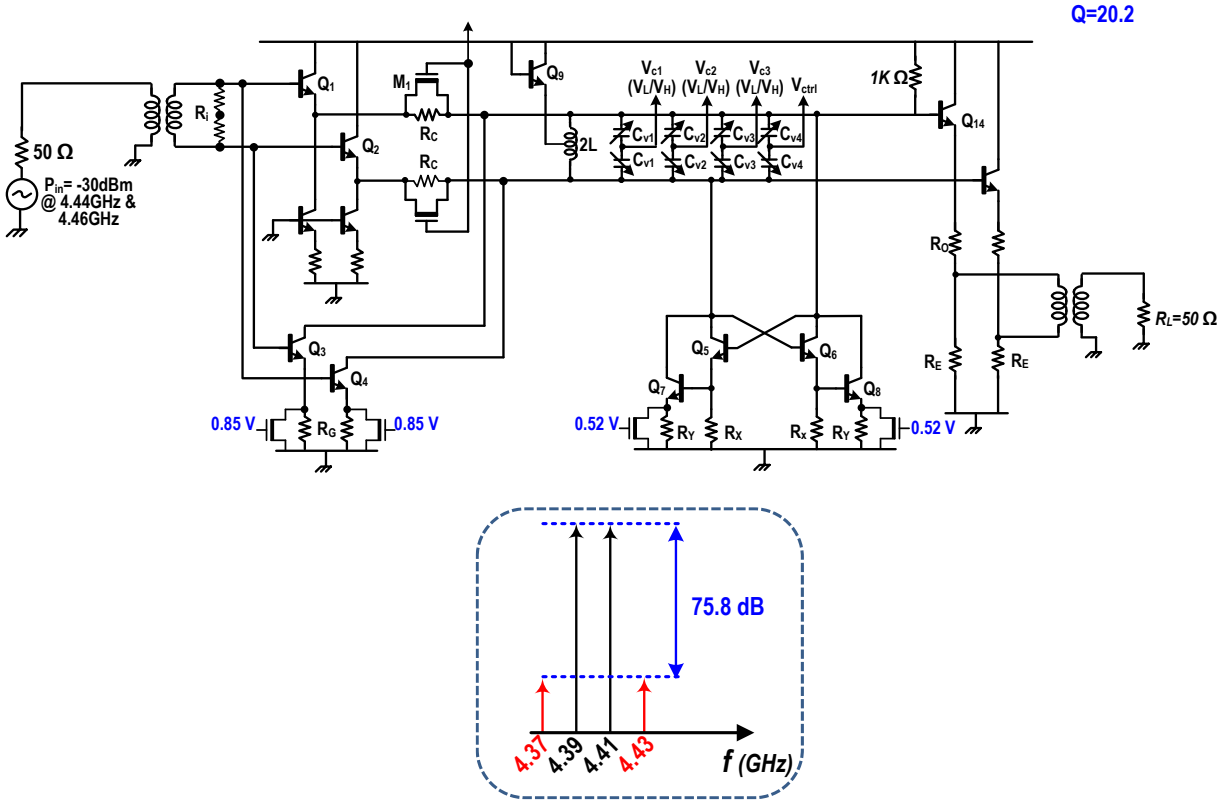

Figure A.9 BPF with output buffer providing Q=20 and resultant IMD_3

A7. BPF and setting Gain=20 dB

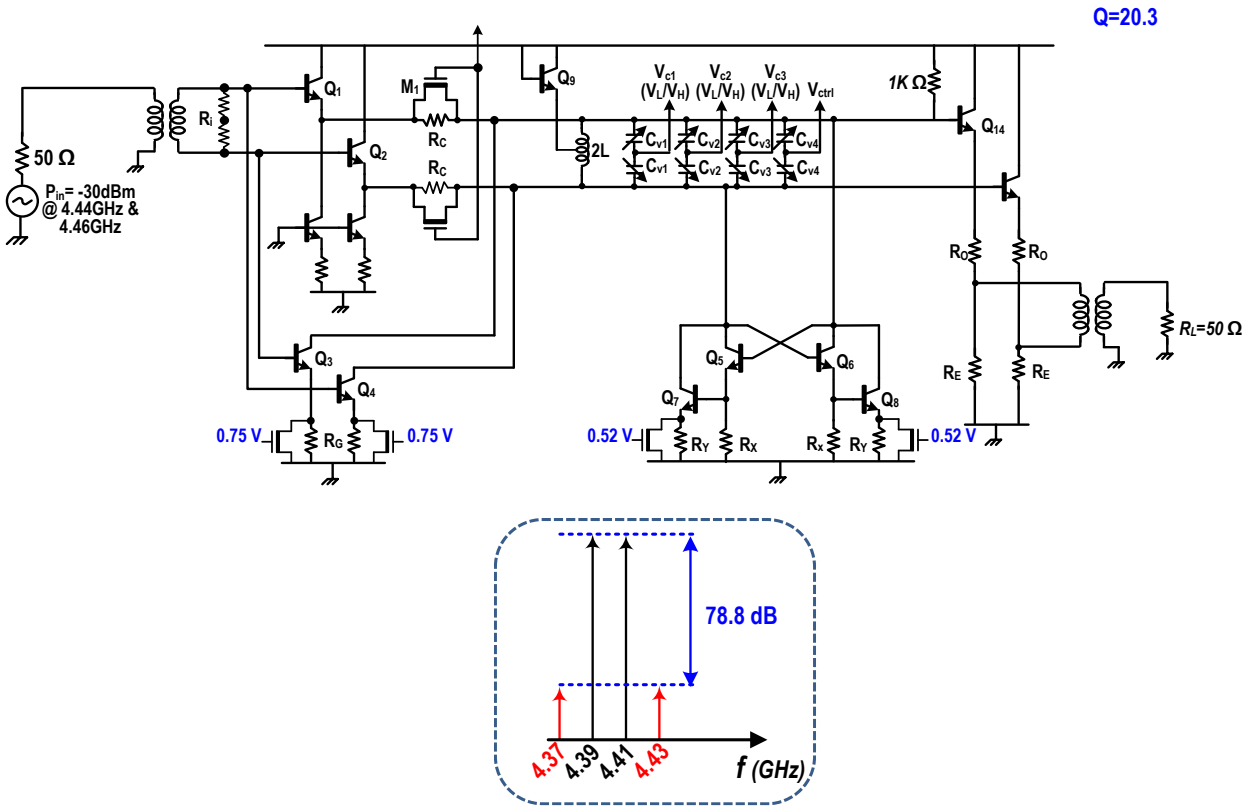

Figure A.10 BPF with output buffer providing Q=20, setting gain around 0 dB and resultant IMD_3

Bibliography

[1] RF Sampling S-band Radar Receiver, *Texas Instrument Designs*, TIDA-00814, May 2016.

[2] M. Ash, M. A. Tanha, P. V. Brennan, A. Köhlert, J. N. McElwaine and C. J. Keylock, "Practical implementation of a 16-channel C-band phased array radar receiver," *2015 IEEE Radar Conference*, Johannesburg, 2015, pp. 66-70.

[3] J. Yu , F. Zhao, J. Cali, D. Ma, X. Geng, F. Dai, J.D. Irwin and A. Aklian, "A single-chip x-band chirp radar MMIC with stretch processing," *Proceedings of the IEEE 2012 Custom Integrated Circuits Conference*, San Jose, CA, 2012.

[4] J. Mitola, "Software radios-survey, critical evaluation and future directions," *[Proceedings] NTC-92: National Telesystems Conference*, Washington, DC, 1992, pp. 13/15-13/23.

[5] J. Mitola, ‘‘Software radio architecture: A mathematical perspective,’’ *IEEE J. Sel. Areas Commun*., vol. 17, no. 4, pp. 514–538, Apr. 1999.

[6] A. A. Abidi, "The Path to the Software-Defined Radio Receiver," in *IEEE Journal of Solid-State Circuits*, vol. 42, no. 5, pp. 954-966, May 2007.

[7] E. Buracchini, ‘‘The software radio concept,’’ *IEEE Commun. Mag*., vol. 38, no. 9, pp. 138–143, Sep. 2000.

[8] R. Bagheri, A. Mirzaei, M. E. Heidari, S. Chehrazi, M. Lee, M. Mikhemar, W. K. Tang, and A. A. Abidi, ‘‘Software-defined radio receiver: Dream to reality,’’ *IEEE Commun. Mag.*, vol. 44, no. 8, pp. 111–118, Aug. 2006.

[9] R. Aigner, "SAW and BAW technologies for RF filter applications: A review of the relative strengths and weaknesses," *2008 IEEE Ultrasonics Symposium*, Beijing, 2008, pp. 582-589.

[10] W. J. Chappell, E. J. Naglich, C. Maxey and A. C. Guyette, "Putting the Radio in “Software-Defined Radio”: Hardware Developments for Adaptable RF Systems," in *Proceedings of the IEEE*, vol. 102, no. 3, pp. 307-320, March 2014.

[11] J. Zhou, A. Chakrabarti, P. Kinget, and H. Krishnaswamy, “Low-noise active cancellation of transmitter leakage and transmitter noise in broadband wireless receivers for FDD/co-existence,” *IEEE J. Solid-State Circuits*, vol. 49, no. 12, pp. 3046–3062, Dec. 2014.

[12] D. Murphy, H. Darabi, A. Abidi, A. A. Hafez, A. Mirzaei, M. Mikhemar, and M.-C. F. Chang, “A blocker-tolerant, noise cancelling receiver suitable for wideband wireless applications,” *IEEE J. Solid-State Circuits,* vol. 47, no. 12, pp. 2943–2963, Dec. 2012.

[13] A. Mirzaei, H. Darabi, and D. Murphy, “A low-power process-scalable super-heterodyne receiver with integrated high-Q filters,” *IEEE J. Solid-State Circuits*, vol. 46, no. 12, pp. 2920–2932, Dec. 2011.

[14] C. Andrews and A. Molnar, “A passive mixer-first receiver with digi- tally controlled and widely tunable RF interface,” *IEEE J. Solid-State Circuits*, vol. 45, no. 12, pp. 2696–2708, Dec. 2010.

[15] Z. Lin, P. l. Mak and R. P. Martins, "2.4 A 0.028mm^2 11mW single-mixing blocker-tolerant receiver with double-RF N-path filtering, S11 centering, +13dBm OB-IIP3 and 1.5-to-2.9dB NF," *ISSCC Dig. Tech. Papers*, 2015.

[16] J. W. Park and B. Razavi, "A 20mw GSMlWCDMA receiver with RF channel selection," *in IEEE ISSCC Dig. Tech. Papers*, Feb 2014.

[17] F. Qazi, Q. T. Duong and J. Dąbrowski, "Two-Stage Highly Selective Receiver Front End Based on Impedance Transformation Filtering," in *IEEE Transactions on Circuits and Systems II: Express Briefs*, vol. 62, no. 5, pp. 421-425, May 2015.

[18] Y. Xu, J. Zhu, and P. Kinget, "A blocker-tolerant RF front end with harmonic-rejecting N-path filtering," in *Proc. IEEE RFIC Symp*, 2014.

[19] R. Chen and H. Hashemi, "Reconfigurable Receiver With Radio-Frequency Current-Mode Complex Signal Processing Supporting Carrier Aggregation," *IEEE J. Solid-State Circuits*, vol. 50, no. 12, pp. 3032–3046, Dec. 2015.

[20] M. Hasan, Q. Gu and X. Liu, "Tunable Blocker-Tolerant RF Front-end Filter with Dual Adaptive Notches for Reconfigurable Receivers," *IEEE MTT-S Int. Microw. Symp.*, May 2016.

[21] M. Darvishi, R. van der Zee, and B. Nauta, "Design of active N-path filters," *IEEE J. Solid-State Circuits*, vol. 48, no. 12, pp. 2962–2976, Dec. 2013.

[22] I. Fabiano, M. Sosio, A. Liscidini, and R. Castello, "SAW-less analog front-end receivers for TDD and FDD," *IEEE J. Solid State Circuits*, vol. 48, no. 12, pp. 3067–3079, Dec. 2013.

[23] H. Hedayati, W.-F. Lau, N. Kim, V. Aparin, and K. Entesari, "A 1.8 dB NF blocker-filtering noise-canceling wideband receiver with shared TIA in 40 nm CMOS," *IEEE J. Solid-State Circuits*, vol. 50, no. 5, pp. 1148–1164, May 2015.

[24] C.-K. Luo, P. S. Gudem, and J. F. Buckwalter, "-Less 3G/4G FDD Diversity Receivers," *IEEE Trans. Microwave Theory and Tech.*, vol. 64, pp. 1110–1121, April 2016.

[25] K. Kibaroglu and G. M. Rebeiz, "An N-Path Bandpass Filter with a Tuning Range of 0.1-12 GHz and Stopband Rejection > 20 dB in 32 nm SOI CMOS," *IEEE MTT-S Int. Microw. Symp.*, May 2016.

[26] I. Madadi, M. Tohidian, R.B. Staszewski, “A 65nm CMOS High-IF Superheterodyne Receiver with a High-Q Complex BPF,” *IEEE RFIC Symposium*, pp. 323-326, June 2013.

[27] M. Darvishi, R. Van der Zee, E. Klumperink, and B. Nauta, “A 0.3-to-1.2GHz tunable 4th-order switched-C bandpass filter with >55dB ultimate rejection and out-of-band IIP3 of 29dBm,” in *IEEE ISSCC Dig. Tech. Papers*, pp.358–360, Feb. 2012.

[28] Y. Xu and P. Kinget, “A Switched-Capacitor RF Front End With Embedded Programmable High-Order Filtering,” *IEEE J. Solid-State Circuits*, vol. 51, no. 5, pp. 1154–1167, May 2016.

[29] R. Chen and H. Hashemi, “A 0.5-to-3 GHz software-defined radio receiver using discrete-time RF signal processing,” *IEEE J. Solid-State Circuits*, vol. 49, no. 5, pp. 1097–1111, May 2014.

[30] M. Tohidian, I. Madadi and R. B. Staszewski, “A fully integrated highly reconfigurable discrete-time superheterodyne receiver,” in *Proc. IEEE Int. Solid-State Circuits Conf. Tech. Dig*., pp. 72–74, Feb. 2014.

[31] J. Choi, M. Raja, and M. Arasu, "A programmable discrete-time filter employing hardware-efficient two-dimensional implementation method", in *Proc. IEEE Asian Solid-State Circuits Conf., 2014*.

[32] A. Geis, J. Ryckaert, L. Bos, G. Vandersteen, Y. Rolain, and J. Craninckx, “A 0.5 mm power-scalable 0.5–3.8 GHz CMOS DT-SDR receiver with second-order RF band-pass sampler,” *IEEE J. Solid-State Circuits*, vol. 45, no. 11, pp. 2375–2387, Nov. 2010.

[33] F. Amin, S. Raman and K. J. Koh, “A High Dynamic Range 4^{th}-order 4-8 GHz Q-Enhanced LC Band-Pass Filter with 2-25% Tunable Fractional Bandwidth,” *IEEE MTT-S Int. Microw. Symp.*, May 2016.

[34] B. Williams, F. J. Taylor, *Electronic Filter Design Handbook. 3rd* ed. New York: McGraw-Hill Inc, 1995.

[35] L. Mohammadi and K. J. Koh, “Integrated Synthetic Bandstop Filters for Blocker Rejection at RF and Microwave Frequency Bands,” *IEEE Trans. Microw. Theory Techn.,* vol. 64, pp. 3557-3567, Nov. 2016.

[36] F. Hu and K. Mouthaan, “L-band bandpass filter with high out-of-band rejection based on CMOS active series and shunt inductors,” *IEEE MTT-S Int. Microw. Symp.*, Jun. 2014.

[37] M.-L. Lee et al., “1.58-GHz thirdorder CMOS active bandpass filter with improved passband flatness,” *IEEE Trans. Microw. Theory Techn.,* vol. 59, no. 9, pp.2275-2284, Sep. 2011.

[38] B. Georgescu et al., “2 GHz Q-Enhanced Active Filter With Low Passband Distortion and High Dynamic Range,” *IEEE J. of Solid-State Circuits*, vol. 41, no. 9, pp. 2029-2039, Sept. 2006.

[39] X. He and W. B. Kuhn, “A 2.5-GHz low-power, high dynamic range self-tuned Q-enhanced LC filter in SOI,” *IEEE J. Solid-State Circuits*, vol. 40, no. 8, pp. 1618–1628, Aug. 2005.

[40] J. Kulyk and J. Haslett, "A monolithic CMOS 2368±30 MHz transformer based Q-enhanced series-C coupled resonator bandpass filter," *IEEE J. Solid-State Circuits,* vol. 41, no. 2, pp. 362-374, Feb. 2006.

[41] A. N. Mohielding , E. Sanchez-Sinencio and J. Silva-Martinez "A 2.7 V 1.8-GHz fourth-order tunable LC bandpass filter based on emulation of magnetically coupled resonators", *IEEE J. Solid-State Circuits,* vol. 38, no. 7, pp.1172 -1181 2003.

[42] S. Pipilos, Y.P. Tsividis, J. Fenk, and Y. Papananos, “A Si 1.8-GHz RLC filter with tunable center frequency and quality factor.” *IEEE J. Solid-State Circuits*, vol. 31, pp. 1517–1525, Oct. 1996.

[43] W.B. Kuhn et al., “Q-Enhanced LC bandpass filters for integrated wireless applications.” *IEEE Trans. Microwave Theory and Tech.*, vol. 46, pp. 2577–2586, Dec. 1998.

[44] W. Kuhn, D. Nobbe, D. Kelly, and A. Orsborn, “Dynamic range per- formance of on-chip

RF bandpass filters," *IEEE Trans. Circuits Syst. II: Analog Digit. Signal Process.*, vol. 50, no. 10, pp. 685–694, Oct. 2003.

[45] T. Soorapanth and S. Wong, "A 0-dB IL 2140 ± 30 MHz bandpass filter utilizing Q-enhanced spiral inductors in standard CMOS." *IEEE J. Solid-State Circuits*, vol. 37, no. 5, pp. 579–586, May 2002.

[46] P. Kallam, E. Sanchez-Sinencio and A. I. Karsilayan, "An enhanced adaptive Q-tuning scheme for a 100-MHz fully symmetric OTA-based bandpass filter," in *IEEE Journal of Solid-State Circuits*, vol. 38, no. 4, pp. 585-593, Apr 2003.

[47] Y. Sun, C. J. Jeong, S. K. Han and S. G. Lee, "CMOS on-chip active RF tracking filter for digital TV tuner ICs," in *Electronics Letters*, vol. 47, no. 6, pp. 407-409, March 17 2011.

[48] M. Darvishi, R. van der Zee, E. A. M. Klumperink and B. Nauta, "Widely Tunable 4th Order Switched Gm-C Band-Pass Filter Based on N-Path Filters," in *IEEE Journal of Solid-State Circuits*, vol. 47, no. 12, pp. 3105-3119, Dec. 2012

[49] D. W. Graham, P. E. Hasler, R. Chawla and P. D. Smith, "A Low-Power Programmable Bandpass Filter Section for Higher Order Filter Applications," in *IEEE Transactions on Circuits and Systems I: Regular Papers*, vol. 54, no. 6, pp. 1165-1176, June 2007.

[50] D. Dowthwaite, K. Newsome, M. Edwards, I. Davis and B. Coaker, "Receiver Protection in S-Band Radars for Mitigation of 4G signal interference," *Microwave J.*, Aug., 2013.

[51] "M. Zergerzadeh, and K. J. Koh, private communication, April. 2016.

[52] Li, M.; Chen, C.; Chen, W.: Miniaturized Dual-Band Filter Using Dual-Capacitively Loaded SIW Cavities, *IEEE Microw. Wireless Compon. Lett*., 27 (2017), 344-346.

[53] D. Psychogiou, R. Gómez-García, A. C. Guyette and D. Peroulis, "Reconfigurable Single/Multi-Band Filtering Power Divider Based on Quasi-Bandpass Sections," in *IEEE Microw. and Wireless Components Letters*, vol. 26, pp. 684-686, Sept. 2016.

[54] Liu, X.; Katehi, L. P. B.; Peroulis, D.: Novel dual-band microwave filter using dual-capacitively-loaded cavity resonators, IEEE Microw. Wireless Compon. Lett., 20 (2010), 610-612.

[55] Lu, Di; Barker, N.S; Tang, X.-H.:Miniaturized dual-band filter with return loss bandwidth and transmission zero control, Int. J. Microwave and Wireless Tech., 1 (2017), 1-7.

[56] Sánchez-Renedo, M.; Gómez-García, R.: Microwave Dual-Band Bandpass Planar Filter Using Double-Coupled Resonating Feeding Sections, 11th Europ. Microw. Conf. Rome, Italy, 2009.

[57] Shen,W.; Yin,W.-Y.; Sun, X.-W.: Miniaturized Dual-Band Substrate Integrated Waveguide Filter With Controllable Bandwidths, IEEE Microw. Wireless Compon. Lett., 21 (2011), 418-420.

[58] Shen, Y.;Wang, H.; Kang,W.,Wu,W.: Dual-Band SIW Differential Bandpass Filter With Improved Common-Mode Suppression, IEEE Microw. Wireless Compon. Lett., 25 (2015), 100-102.

[59] S. Lee, D. Jeong, H. Jin and B. Kim, "Reconfigurable 4 channel carrier aggregation receiver using harmonic recombination technique," *Proc. 11th Europ. Microw. Integrated Circuits Conf.*, 2016.

[60] S.-C. Hwu and B. Razavi, “An RF receiver for intra-band carrier aggregation,” *IEEE J. Solid-State Circuits*, vol. 50, no. 4, pp. 946-961.

[61] A. Vallese, A. Bevilacqua, C. Sandner, M. Tiebout, A. Gerosa and A. Neviani, "Analysis and Design of an Integrated Notch Filter for the Rejection of Interference in UWB Systems," in *IEEE Journal of Solid-State Circuits*, vol. 44, no. 2, pp. 331-343, Feb. 2009.

[62] A. Ghaffari, E. A. M. Klumperink and B. Nauta, "Tunable N-Path Notch Filters for Blocker Suppression: Modeling and Verification," in *IEEE Journal of Solid-State Circuits*, vol. 48, no. 6, pp. 1370-1382, June 2013.

[63] D. Li and Y. Tsividis, “Design techniques for automatically tuned integrated gigahertz-range active filters,” *IEEE J. Solid-State Circuits*, vol. 37, no. 8, pp. 967–977, Aug. 2002.

[64] F. Bahmani, T. Serrano-Gotarredona and E. Sanchez-Sinencio, "An Accurate Automatic Quality-Factor Tuning Scheme for Second-Order LC Filters," in *IEEE Transactions on Circuits and Systems I: Regular Papers*, vol. 54, no. 4, pp. 745-756, April 2007.